Constraining the Ephemeris and Interior Structure of Io using Space-Based Astrometry by JUICE

Kai Zenk

Technische Universiteit Delft

Constraining the Ephemeris and Interior Structure of Io using Space-Based Astrometry by JUICE

by

Kai Zenk

to obtain the degree of Master of Science
at the Delft University of Technology,
to be defended publicly on Tuesday December 19, 2023 at 09:30 AM.

Student number:	5622832	
Project duration:	March 1, 2023 – December 19, 2023	
Thesis committee:	Prof. dr. L.L.A. Vermeersen,	Committee chair
	Dr. ir. D. Dirkx,	Supervisor
	Ir. M. Fayolle,	Co-Supervisor
	Dr. ir. M.R.N. Rovira Navarro,	Examiner

This thesis is confidential and cannot be made public until December 19, 2025.

The cover picture is an artist’s impression of the JUICE mission exploring the Jovian system.
Image credit: ESA.

Preface

Having postponed writing this preface to the last day before having to hand in my thesis feels like it is the ultimate, final piece to my past six years of being a student. After having spent four amazing years in Aachen that - for my feeling - have undoubtedly taught me more than everything there is to know about independence and intrinsic motivation, coming to Delft has at first felt like a unique form of academic culture shock. In Delft, with only eight weeks into the master, after having already handed in a ton of deadlines, the first exams had to be taken - while I cannot remember having ever done much productive in the first eight weeks of the academic year in Aachen aside from sporadically checking which classes were actually worth attending. Maybe this is why the TU Delft initially refused my application to the Space Flight program...

Thus, in analogy to the zeroth law of thermodynamics, I would introductory - but not firstly - like to thank Sander Barendrecht for all his patience in our countless mailing contacts. Even though we sometimes had mixed feelings for each other - I can only imagine this also being true for him, it definitely has been the case for me - without him, I would most likely not be writing these lines and the past two years would not have been the same for me.

Having saved my first thank you, I would like to express my eternal gratitude for the two best supervisors I could have ever dreamt of - Dominic and Marie. Whilst one of the biggest advantages of having two supervisors is receiving twice the amount of feedback - this could simultaneously turn out to be a significant disadvantage. Yet, with all your input and ideas, as well as motivating feedback I never once regretted the decision of choosing the two of you as supervisors, and I am sure this work has greatly benefited from it. Even though it has also been a lot of hard work having to wrap my head around all those covariance matrices, you made writing this thesis adventure so much fun.

Since studying would be much more boring without friends, many thanks go out to everyone who has made my time in Delft so special, for your emotional support, the countless iterations of proofreading this work, and the many times you forced me to put my nose out of the books and enjoy other aspects of life. I really needed those reminders and will always appreciate every free moment I have spent doing other things than studying. It would be wrong not to mention Justus Jonas, Peter Shaw, and Bob Andrews who - unknowingly - have shared large portions of the writing process of this thesis work with me. Last but certainly not least, a big thank you to my family for all their unconditional and never-ending support during my studies and all those years that came before.

Abstract

Owing to the assumed presence of sub-surface oceans, the Galilean satellites - Io, Europa, Ganymede, and Callisto - are among the most promising candidates for potential extraterrestrial habitats within our Solar System. To this end, the moons are going to be extensively studied by the upcoming JUICE and Europa Clipper missions. Ultimately, understanding the dynamics of the Jovian system is a means to shed light on the general existence and stability of these presumed habitable worlds as well as the formation and evolution of the entire Solar System. Yet, while the dynamics of Ganymede (in particular via the orbital phase of JUICE) and Europa (mainly via the various flybys of Europa Clipper) are going to be observed to an unprecedented level of accuracy, the absence of flybys of Io due to its harsh radiation-environment results in a significantly imbalanced data set. To stabilise the numerical data inversion, spaced-based imaging by the camera subsystem of JUICE is crucial to constrain the dynamics of Io.

However, while the analysis of orbital dynamics is usually performed with respect to the centre-of-mass (COM) of natural satellites, optical space-based astrometry provides measurements of the position of a body's centre-of-figure (COF), introducing a discrepancy between the dynamical and observational model. Explicitly accounting for the offset between the observed centre-of-figure and the propagated centre-of-mass during ephemeris estimation, however, ensures the consistency of the dynamical and observational model. In turn, this allows us to assess the extent to which optical space-based astrometric observations might either validate the merely indirectly obtained radio science data or contribute to the overall orbital solution of Io. Finally, obtaining a measure of the offset between the centre-of-figure and centre-of-mass yields an entirely new constraint on the interior structure and composition of Io.

In order to quantify the COF-COM-offset, we have simulated optical astrometric observations by JUICE and subsequently determined the formal uncertainties of the estimated offset using covariance analyses. Using suitably computed *a prioir* covariance matrices, we have constrained our analyses to the averaged propagated formal errors of Io that would arise from the radiometric tracking set-up of JUICE and Europa Clipper. We have found that the contribution of optical space-based astrometry to the COF-COM-offset of Io and its estimated state highly depends on the observations' quantity, quality, and geometry. Thus, an algorithm for the selection epochs at which images are to be simulated based on the main drivers - the absolute uncertainties and relative geometries of a series of observations - of the formal errors COF-COM-offset has been developed. However, owing to the largely equatorial alignment of JUICE with respect to Io - observations of the in-plane contribution have been found to be obstructed by the brightness of Jupiter. To maximise the scientific return of optical space-based astrometry, in particular, astrometry during the high-inclination phase has proven beneficial.

Overall, significant constraints of the discrepancy between the centre-of-figure and centre-of-mass and the orbital solution of Io have been obtained. For an expectable number of about 1300 images being taken of Io, realistically attainable formal uncertainties in the estimated COF-COM-offset of no more than 300 metres have been obtained. Furthermore, since notable contributions to the orbital solution already occur for reasonable radio science true-to-formal-error ratios between two and five, we have concluded a high likelihood of space-based astrometry contributing to the orbital solution. This potential of space-based imaging to balance and contribute to the orbital solution of Io thus motivates future research concerning the offset between the centre-of-figure and centre-of-mass.

Contents

Nomenclature

Abbreviations and Acronyms

ABM	Adams-Bashforth-Moulton
BS	Bulirsch-Stoer
COF	Centre-of-Figure
COM	Centre-of-Mass
CReMA	Consolidated Report on Mission Analysis
DP	Dormand-Prince
DEC	Declination
ESA	European Space Agency
FOV	Field-of-View
IMCCE	Institut de Mécanique Céleste et de Calcul des Ephémérides
JUICE	Jupiter Icy Moons Explorer
MEE	Modified Equinoctial Elements
MRP	Modified Rodrigues Parameters
NAC	Narrow Angle Camera
NASA	National Aeronautics and Space Administration
NavCam	Navigation Camera
NOE	Numerical Orbit and Ephemerides
RA	Right Ascension
RK	Runge-Kutta
RKF	Runge-Kutta-Fehlberg
RSW	Radial (R), Along-Track (S), and Normal (W)
SPICE	Spacecraft Planets Instrument C-Matrix Events
tudat	TU Delft Astrodynamics Toolbox
USM	Unified State Model
UVS	Ultraviolet Spectrograph
VLBI	Very-Long Baseline Interferometry

Latin Symbols

C	Spherical harmonics cosine gravity coefficient. Subscripts indicate degree and order [-]; Surface roughness scaling factor [-]
c_q	Contribution to the solution an estimated parameter [-]
d_a	Apparent diameter [-]
D	Distance between a spacecraft and a satellite [m]
$\vec{F}$	Tidal force vector
FOV	Size of the field-of-view of a camera [-]
G	Gravitational constant [Nm^2/kg^2]
GM	Gravitational parameter [km^3/s^2]
$\vec{h}$	Observations vector

$\boldsymbol{H}$	Observations partials (or design) matrix
$\boldsymbol{I}$	Identity matrix
J_2	Oblateness [-]
k	Love number. Subscript indicates degree [-]
K	Scaling factor for covariance matrices [-]
m	Mass [kg]
n	Orbital mean motion [1/s]; Number of simulated observations [-]
N_{FOV}	Number of stars in the field-of-view [-]
N_{pixels}	Number of pixels in the field-of-view [-]
$\vec{p}$	Parameters vector
P	Legendre polynomial. Subscripts indicate degree and order [-]
$\boldsymbol{P}$	Covariance matrix
$\vec{q}$	Estimated parameters vector
Q	Tidal quality factor [-]
$\vec{r}$	Position vector
R	Equatorial radius [m]
R^2	Coefficient of determination [-]
$\boldsymbol{R}$	Rotation matrix
S	Spherical harmonics sine gravity coefficient. Subscripts indicate degree and order [-]
$\boldsymbol{S}$	Sensitivity matrix
t	Time since J2000 [s]
T	Period of the main tidal excitation [1/s]
$\boldsymbol{W}$	Weight matrix
$\vec{x}$	State vector
$\vec{z}$	Observables vector

Greek Symbols

α	Right ascension [deg]
δ	Declination [deg]
Δt	Tidal time lag [s]
ϵ	Integration error [m]
θ	Longitude of conjunction [deg]
λ	(Mean) longitude [deg]
μ	Gravitational parameter [km^3/s^2]
ρ	Correlation factor [-]
σ	Formal errors [var.]
σ_{c}	Formal centre-of-figure uncertainty [-]
σ_{p}	Formal pointing uncertainty [-]
σ_{sc}	Formal spacecraft position uncertainty [-]
ϕ	Latitude [deg]
ϕ_L	Laplace angle [deg]
$\boldsymbol{\Phi}$	State transition matrix
ω	Argument of pericentre [deg]
Ω	Spin frequency [1/s]
$\vec{\Omega}$	Angular velocity vector

Subscripts

0	Referring to an initial time or state, or *a priori* information; Referring to Jupiter
1, I, Io	Referring to Io
2, E	Referring to Europa
3, G	Referring to Ganymede
COF	Referring to the centre-of-figure
extraction	Referring to the achievable subpixel precision
l	Degree of a spherical harmonic coefficient
m	Order of a spherical harmonic coefficient
min	Referring to a minimum
NAC	Referring to Cassini's Narrow Angle Camera
NavCam	Referring to JUICE's Navigation Camera
obs	Referring to an observation
sc, S/C	Referring to a spacecraft
α	Referring to the right ascension
δ	Referring to the declination

1

Introduction

Since its first observations dating back to prehistoric times, the exploration of Jupiter, the largest planet in the Solar System, has slowly but steadily accelerated. Galileo Galilei's discovery of 'his' moons of Jupiter in 1610 shattered the views of the Catholic Church in Italy and Europe - if other celestial objects apart from Earth were also orbited by natural satellites, could geocentrism still be trusted? However, essentially removing 'God's creation' from the centre of the universe meant opposing the Church and thus simultaneously paved the way for both heliocentrism and Galileo's rise as Antichrist. Nonetheless, over the past five decades, Jupiter and the Galilean moons - Io, Europa, Ganymede, and Callisto - have become one of the most frequently studied parts of the Outer Solar System. In particular, owing to the assumed presence of sub-surface oceans, the Galilean satellites are among the most promising candidates for potential extraterrestrial habitats within our Solar System. Ultimately, understanding the dynamics of the Jovian system - a miniature planetary system of its own right - is a means to shed light on the general existence and stability of these presumed habitable worlds as well as the formation and evolution of the entire Solar System (*e.g.* Fuller et al., 2016; Heller et al., 2015; Samuel et al., 2019). To this end, both the National Aeronautics and Space Administration (NASA) and the European Space Agency (ESA) have denoted two large science missions, Europa Clipper and JUICE (Jupiter Icy Moons Explorer), respectively, to the study of the icy moons of Jupiter.

The dynamics of the four Galilean satellites are strongly influenced by the extensive tidal stretching and squeezing between the moons and Jupiter, exhibiting a unique link between orbital and thermal energy, capable of uniquely shaping the interior characteristics of the four moons (*e.g.* Greenberg, 2010; Steinke, 2021). Notably, the tidal coupling between Jupiter and Io - with the latter being the most volcanically active object in the Solar System due to tidally induced heating (*e.g.* Davies, 2007; Peale et al., 1979) - significantly drives the long-term evolution of the Jovian system. In essence, given a non-rigid body, tidal interactions manifest themselves as elongated tidal bulges (Hussmann et al., 2010). Owing to the slight eccentricity and inclination of the orbit of Io (and the remaining Galilean satellites) and the tidal locking causing the rotation rate to equal the orbital mean motion over the course of one orbit, periodically librating tides are induced (Kaula, 1964). The kinetic energy stored within these libration tides and the moons' viscoelastic response subsequently results in friction and thus dissipation into heat. Hypothetically, while dissipation in Io would dampen the eccentricity of the orbit - thus counteracting its cause by circularising the motion of Io - the current state of Io on its own would not be stable and subject to considerable changes in its orbital elements (*e.g.* Yoder, 1979; Yoder and Peale, 1981). Yet, by forcing the orbits of the moons to always be slightly eccentric - owing to the so-called Laplace resonance between Io, Europa, and Ganymede (*e.g.* Lainey et al., 2006; Lari, 2018) - the complex dynamics of the Galilean moons stabilise the overall system (Greenberg, 2010). To this end, we require highly accurate ephemerides of the Galilean moons to detect long-term effects due to tidal dissipation - exploiting the thermo-mechanical coupling, these effects can be directly linked to the tidal heating as well as indirectly to the long-term evolution and interior structure of the satellites (Greenberg, 2010; Lainey et al., 2004, 2009, 2012).

To date, ephemeris solutions for the Galilean moons are mainly based on optical ground-based astrometric observations spanning a period of more than a century, irregularly supplemented by space-based astrometric images and tracking data from Voyager and Galileo (Jacobson et al., 2000; Lainey et al., 2004, 2009). Even though old astrometry usually exhibits high associated uncertainties (up to hundreds of kilometres) - owing to their extensive temporal coverage - classical ground-based observations are crucial for reconstructing the long-term orbital dynamics of the Jovian system (*e.g.* Dias-Oliveira et al., 2013; Lainey et al., 2009; Vienne, 2008). Nevertheless, the determination of extremely weak dynamical effects (such as tidal dissipation) requires significantly more accurate measurements of the states of the Galilean satellites (*e.g.* Fayolle et al., 2021). While the dynamics of Ganymede (in particular via the orbital phase of JUICE) and Europa (mainly via the various flybys of Europa Clipper) are going to be observed to an unprecedented level of accuracy (Fayolle et al., 2022; Magnanini et al., 2023), the absence of flybys of Io due to its harsh radiation-environment results in a significantly skewed data set. Even though we expect significant improvements as a result of the global inversion of existing ground-based astrometric observations (Fayolle et al., 2023), the combined radio science solution by JUICE and Europa Clipper is going to greatly dominate the estimation of the moons' ephemerides over the missions' time spans. Given that the state of Io is only indirectly constrained via the Laplace resonance, correlations between the states of the respective moons make the reconstruction of the satellites' dynamics unstable. Thus, to improve the stability of Io's ephemeris solution, merging the radio science data from JUICE and Europa Clipper with optical space-based astrometry by the imaging subsystem of JUICE has been suggested to constrain the dynamics of Io (*e.g.* Dirkx et al., 2017; Fayolle et al., 2022). A similar approach has previously been used for the ephemeris determination of the Saturnian satellites using optical data taken by Cassini (*e.g.* Lainey et al., 2012, 2017, 2020).

However, while the analysis of orbital dynamics is usually performed with respect to the centre-of-mass (COM) of natural satellites - with spacecraft radio science also being directly sensitive to the position of the centre-of-mass - optical space-based astrometry provides measurements of the position of a body's centre-of-figure (COF) in an absolute reference frame (Pasewaldt et al., 2012). For most natural satellites - with the Moon being a prominent exception (Smith et al., 1997; Zuber et al., 1994) - a quantification for the offset between the respective COM and COF is lacking. Yet, given the high expected accuracy of space-based astrometry, this offset could potentially be one of the most dominant - but so far unaccounted (Fayolle et al., 2023) - sources of error in the astrometric reduction of space-based optical data of Io. Furthermore, obtaining a measure of the offset between the centre-of-figure and centre-of-mass of Io yields an entirely new constraint on the physical state of Io. To date, the interior structure and composition of Io remain highly debated. While various types of observations constrain the moon's interior, they lead to a - sometimes even contradicting - intricate chain of logical arguments to which the offset between the COF and COM will add a new link. Potentially, a new constraint might allow us to draw conclusions on the melt fraction of Io's mantle or variations in crustal thickness and asymmetry in its internal composition. As outlined by Steinke (2021), exploiting the tidal coupling between Io and Jupiter, this could, in turn, lead to an improvement in our understanding of how tidal dissipation, melting, and heat transport interact.

1.1. Research Objective

As above-outlined, a better understanding of the tidal dissipation inside Io would lead to significant advances in modelling the evolution and formation of the Jovian system and tidally heated bodies in general. Yet, the absolute lack of flybys of Io by either JUICE or Europa Clipper results in a significantly imbalanced data set, highlighting the need for optical space-based astrometric observations of Io to improve and stabilise current ephemeris-estimations. However, the offset between the centres of figure and mass, i.e. the discrepancy between what can be measured and what should be the model input, might have a detrimental effect on the overall achievable uncertainty of space-based imaging and the orbital solution of Io. To this end, we have formulated the following principal research objective:

The goal of this thesis is to estimate and analyse the discrepancy between the centre-of-figure and centre-of-mass of Io, and subsequently determine the ability of optical space-based astrometric observations to contribute to the overall orbital solution.

To reach this objective in a structured way, it is split into several research questions, which shall be briefly addressed. First, we have to set up an environment that enables us to simulate optical space-based observations, taking observational and imaging constraints into account. Furthermore, we have to develop an analytical framework that mimics the error induced by an optical reduction pipeline in order to derive realistic uncertainties associated with space-based astrometry observations. This forms the foundation of the following steps. We phrase the following research question:

RSQ 1: *How can we simulate optical space-based astrometric observations whilst simultaneously deriving realistic associated uncertainties?*

In all subsequent steps, we will use these simulated space-based observations and their respective uncertainties within an estimation framework to emulate the effects of the discrepancy between the centre-of-figure and centre-of-mass of Io to answer the following research questions:

RSQ 2: *How can we account for the COF-COM-offset of Io within our dynamical model?*

RSQ 3: *To what extent will different relative observation geometries and uncertainties of optical observations influence the formal errors of the estimated COF-COM-offset?*

RSQ 4: *What is the influence of the radio science quality on the space-based astrometry's ability to constrain the estimation of the COF-COM-offset and contribute to the orbital solution?*

Ultimately, to place the importance of the potential existence of an offset between Io's centre-of-figure and centre-of-mass into a broader scientific context, a final research question is formulated:

RSQ 5: *Which insights can a measure of the discrepancy between the centre-of-figure and centre-of-mass of Io give us on the interior structure of Io?*

1.2. Report Outline

To constrain the offset between the centre-of-figure and centre-of-mass and improve the quality of the orbital solution of Io using optical space-based astrometry, this thesis develops an estimation framework to account for a potential discrepancy between the imaged centre-of-figure and propagated centre-of-mass of Io. The main part of this thesis has been written in the form of a scientific paper, presented in Chapter 2. In-depth conclusions and recommendations for future work given in Chapter 3 complement the contents of the paper. Furthermore, to allow a holistic interpretation of the provided results, additional information is outlined in the appendices to this work. Introductory, the choice of suitable integrator and propagator settings is delineated in Appendix A, followed by the main verification and validation steps that have been performed alongside the work on this thesis in Appendix B. In particular, this entails proving the consistency of the implemented dynamical model including the presence of the Laplace resonance in Appendix B.1, as well as the validation of optical observation constraints in Appendix B.2. Subsequently, Appendix B.3 verifies the robustness of the implemented estimation framework. Finally, in Appendix C, we present additional material that complements the results discussed in the journal paper.

2

Journal Paper

The core methodology, results and conclusions of this thesis have been written in the form of a scientific paper to be submitted to the Astronomy and Astrophysics journal. Within this chapter, the manuscript, adhering to the required template, is provided.

Astronomy & Astrophysics
December 19, 2023

Constraining the Ephemeris and Interior Structure of Io using Space-Based Astrometry by JUICE

K.G. Zenk

Delft University of Technology, Kluyverweg 1, 2629HS Delft, The Netherlands
e-mail: `k.g.zenk@student.tudelft.nl`

December 19, 2023

ABSTRACT

Context. Being among the most promising candidates for potential extraterrestrial habitats within our Solar System, the Galilean satellites are going to be extensively studied by the upcoming JUICE and Europa Clipper missions. Both spacecraft will provide intensive amounts of radio science tracking data. Yet, with no scheduled flybys of Io, the resulting radio science data set is going to be skewed towards the three outer satellites. Thus, to stabilise the numerical data inversion, optical space-based astrometry by the imaging subsystem of JUICE is crucial to constrain the dynamics of Io. Yet, being sensitive to a body's centre-of-figure, instead of the propagated centre-of-mass, space-based imaging introduces a discrepancy between the dynamical and observational model.
Aims. Explicitly accounting for the offset between the observed centre-of-figure (COF) and the propagated centre-of-mass (COM) during ephemeris estimation could however mitigate the influence of the discrepancy on the orbital solution of Io.
Methods. To quantify this, we have performed the inversion of simulated optical astrometric observations by JUICE. Using suitable *a priori* covariance matrices, the initial state of Io has been constrained to the expected level of formal uncertainties of a combined JUICE and Europa Clipper radio science solution. By assessing the contribution of the optical observations to the ephemeris as a function of the radio science true-to-formal-error ratio, we discuss to which extent space-based imaging could help to either validate the merely indirectly obtained radio science data or constrain the orbital solution of Io. Main drivers of the formal errors in the offset between the COF and COM have been cast into an algorithm for the selection of optical observation epochs.
Results. The contribution of optical space-based astrometry to the COF-COM-offset of Io and its estimated state highly depends on the observations' quantity, quality, and geometry. Significant contributions to the orbital solution already occur for reasonable radio science true-to-formal-error ratios, confirming the initial premise of using optical space-based astrometry to stabilise the imbalanced radio science data set. Reductions in the obtainable uncertainties for the COF-COM-offset range from about 20 to 50 per cent - depending on the number of observations - using suitable algorithms to select the epochs at which observations are to be simulated. In particular, observations during the high-inclination phase have proven especially beneficial.
Conclusions. Significant constraints of the discrepancy between the centre-of-figure and centre-of-mass and the orbital solution of Io have been obtained. This potential of space-based imaging thus motivates future research to stabilise the orbital solution of Io.

Key words. astrometry – centre-of-figure – ephemerides – planets and satellites: Galilean moons – methods: data analysis

1. Introduction

The Galilean satellites are among the most promising candidates for potential extraterrestrial habitats within our Solar System. To investigate the general existence and stability of these presumed habitable worlds - in particular, the presence of subsurface oceans - as well as to shed light on the formation of the entire Solar System, understanding the evolution of these moons is crucial (*e.g.* Fuller et al. 2016; Heller et al. 2015; Samuel et al. 2019). In particular, tidal dissipation and heating - estimable by meticulously reconstructing the dynamics of the Galilean satellites - are key to the orbital evolution of planetary systems (Dirkx et al. 2017; Greenberg 2010; Schubert et al. 2004). Hence, the significant tidal coupling between Jupiter and Io - with the latter being the most volcanically active object in the Solar System due to tidally induced heating (*e.g.* Davies 2007; Peale et al. 1979) - distinctively drives the long-term evolution of the Jovian system. Yet, given the complex dynamics of the Galilean satellites due to the Laplace resonance between Io, Europa, and Ganymede (*e.g.* Lainey et al. 2006; Lari 2018), improved ephemerides' solutions are necessary to detect the secular signatures of tidal mechanisms (Greenberg 2010; Lainey et al. 2004, 2009, 2012).

To date, ephemeris solutions for the Galilean moons are mainly based on optical ground-based astrometric observations spanning a period of more than a century, irregularly supplemented by space-based astrometric images and tracking data from Voyager and Galileo (Lainey et al. 2004, 2009; Lieske 1998; Jacobson et al. 2000). Even though classical ground-based astrometric observations are indispensable to reconstruct the long-term orbital dynamics of the Jovian system (*e.g.* Vienne 2008; Lainey et al. 2009; Dias-Oliveira et al. 2013), the determination of extremely weak dynamical effects (such as tidal dissipation) requires significantly more accurate measurements of the states of the Galilean satellites (Fayolle et al. 2021). Thus, radio science tracking data of both ESA's upcoming JUICE and NASA's Europa Clipper missions will provide highly accurate - yet indirect - constraints, anticipated to yield pivotal insights into the dynamics of the Galilean satellites (*e.g.* Fayolle et al. 2023).

However, while the dynamics of Ganymede (in particular via the orbital phase of JUICE) and Europa (mainly via the various flybys of Europa Clipper) are going to be observed to an unprecedented level of accuracy (Cappuccio et al. 2020; Fayolle et al. 2022; Magnanini et al. 2023), the absence of flybys of Io due to its harsh radiation-environment results in a significantly skewed data set. Even though we expect significant improvements as a result of the global inversion of existing ground-based astrometric observations (Fayolle et al. 2023), the combined radio science solution by JUICE and Europa Clipper is going to greatly dominate the estimation of the moons' ephemerides over the time spans of the missions. With the state of Io only indirectly constrained via the Laplace resonance, the correlations between the respective moons' states render the reconstruction of the satellites' dynamics unstable, while simultaneously leading to a rapid increase in the propagated uncertainties of Io outside of the missions' time spans. To stabilise the estimation of Io's ephemeris solution, merging the radio science data from JUICE and Europa Clipper with optical space-based astrometry by the imaging subsystem of JUICE has been suggested to constrain the dynamics of Io (*e.g.* Dirkx et al. 2017; Fayolle et al. 2022), as it has previously been done for the Saturnian satellites using optical data taken by Cassini (Lainey et al. 2012, 2017, 2020).

In general, space-based imaging of natural satellites has become increasingly popular within the field of astrometry. Recent applications include observations of Saturn's satellites by the Hubble Space Telescope (French et al. 2006), astrometry performed on images of the Martian satellites Deimos and Phobos taken by the Mars Express mission (Oberst et al. 2006; Willner et al. 2008; Pasewaldt et al. 2012), as well as reductions of observations taken by Cassini of both Amalthea and Thebe (Cooper et al. 2006), and a series of Saturnian satellites (Tajeddine et al. 2013, 2015). Furthermore, owing to the relative proximity of space-based observers, space-based astrometric observations yield an unparalleled level of accuracy - compared to classical astrometry and the observation of mutual phenomena from Earth - in the order of a mere few kilometres (Tajeddine et al. 2013, 2015). Besides their low level of formal uncertainties, the different observation geometries compared to ground-based observations and the independence of Jupiter's opposition make space-based astrometry highly interesting (*e.g.* Fayolle et al. 2023). Overall, space-based imaging has proven essential in the accurate determination of ephemerides (Gomes-Júnior et al. 2022; Tajeddine et al. 2015).

However, while the inversion of orbital dynamics is usually performed with respect to the centre-of-mass (COM) of natural satellites, optical space-based astrometry yields the position of a body's centre-of-figure (COF) in an absolute reference frame (*e.g.* Pasewaldt et al. 2012). For most natural satellites - with the Moon being a prominent exception (Smith et al. 1997; Zuber et al. 1994) - a quantification for the offset between the respective centre-of-mass and centre-of-figure is lacking. Nevertheless, given the high expected accuracy of space-based astrometry - up to one kilometre at times for Cassini (Tajeddine et al. 2015) - already small offsets could potentially be one of the most dominant - but so far unaccounted - sources of error in the astrometric reduction of space-based optical data of Io. Thus, even though the combined tracking data of JUICE and Europa Clipper, as well as expected future improvements due to global inversion strategies will already significantly enhance and balance the orbital solution of Io (Fayolle et al. 2023), the realistic reduction of space-based astrometry is crucial to stabilise the data inversion. Furthermore, optical observations will yield an independent data-subset which might prove beneficial to validate the merely indirectly constrained radio science solution of Io.

Obtaining a measure of the offset between the centre-of-figure and centre-of-mass of Io furthermore yields an entirely new constraint on the physical state of Io, potentially allowing us to draw conclusions on the melt fraction of Io's mantle or variations in crustal thickness and asymmetry in its internal composition. Exploiting the tidal coupling between Io and Jupiter, this could, in turn, lead to an improvement in our understanding of how tidal dissipation, melting, and heat transport interact (Steinke 2021). To date, the interior structure and composition of Io remain highly debated. Even though various types of observations constrain the moon's interior, they are usually a sufficient but not necessary condition, leading to a - sometimes even contradicting - intricate chain of logical arguments to which the offset between the COF and COM will add a new link. Nonetheless, it is crucial to find a consistent description of Io's internal structure that is in line with all available observations and physical and chemical laws (Steinke 2021). As of yet, constraints of the interior of Io have thus mainly been based on inferences drawn from measurements of both the gravity (*e.g.* Anderson et al. 2001; Moore et al. 2007) and magnetic field (Khurana et al. 2011), as well as observations of the topography (Thomas et al. 1998), the ubiquitous volcanoes (Keszthelyi et al. 2007; Davies et al. 2023), or the oscillation of auroral spots (Roth et al. 2017).

To improve the quality of the orbital solution of Io using optical space-based astrometry and constrain the offset between the centre-of-figure and centre-of-mass, this paper develops an estimation framework to account for a potential discrepancy between the imaged centre-of-figure and propagated centre-of-mass of Io. To this end, space-based astrometric observations taken by the NavCam of JUICE are simulated. Owing to the substantial variations in relative observation geometries and formal uncertainties, suitable epoch selection algorithms are implemented and reviewed. Using the results by Fayolle et al. (2023), the estimated formal errors are constrained to the expected level of uncertainties of the combined radio science solution of JUICE and Europa Clipper without having to implement their intricate tracking set-up. Finally, we discuss how the found results could either validate the radio science solution or better constrain the estimated orbital solution and simultaneously shed light on the formation and interior structure of Io.

Analytical models used for the mathematical description and propagation of Io's orbital dynamics are first delineated in Section 2, covering gravitational interaction, rotation models, and the computation of tides. Subsequently, Section 3 gives an outline of how space-based optical observations are simulated, followed by a brief overview of the relevant foundations of orbit determination in Section 4 before presenting our results and findings in Section 5. Finally, we discuss the implications of the provided outcomes on the validation of the radio science solution and the estimation of the orbit of Io, as well as any arising constraints for the satellite's interior structure, before conclusions can be drawn in Sections 6 and 7, respectively.

2. Orbital Dynamics and Models

Within this section, we delineate the different dynamical models used to propagate the state of Io. Generally, these are largely similar to those by Lainey et al. (2004, 2009); Fayolle et al. (2022). Besides, following the work by Dirkx et al. (2016), the selection of models has been driven by their potential relevance in the context of the JUICE mission. In Section 2.1, we give an outline of the mechanics of gravitationally interacting extended bodies followed by the models used to describe rotation and tidal interactions in Section 2.2 and 2.3. Subsequently, we present a comprehensive overview of the explicit equations of motion that describe the dynamics of Io in Section 2.4 before briefly highlighting any relevant physical characteristics of the Jovian system in Section 2.5.

2.1. Gravitational Interactions

In general, the gravitational acceleration of an arbitrary body i due to body j can be decomposed into the interactions between two point masses, between one point mass and an extended body, and between two extended bodies (Lainey et al. 2004):

$$\ddot{\boldsymbol{r}}_{ij} = \ddot{\boldsymbol{r}}_{\bar{i}\bar{j}} + \ddot{\boldsymbol{r}}_{\bar{i}\hat{j}} + \ddot{\boldsymbol{r}}_{\hat{i}\bar{j}} + \ddot{\boldsymbol{r}}_{\hat{i}\hat{j}}, \tag{1}$$

where $\boldsymbol{r}_{ij} = \boldsymbol{r}_i - \boldsymbol{r}_j$ denotes the vector between the centres-of-mass of the two bodies, and indexed bars or hats indicate treatment as a ponctual or extended body, respectively. It is common practice to omit the last term delineating - very small - extended body interactions (Lainey et al. 2004), an assumption further justified in the work of Dirkx et al. (2016, 2019). Introducing the gravitational potential functions U_i and U_j of bodies i and j, respectively, the remaining terms can be written as

$$\ddot{\boldsymbol{r}}_{\bar{i}\bar{j}} = \mu_j \nabla U_{\bar{j}}\left(\boldsymbol{r}_{ij}\right), \tag{2a}$$

$$\ddot{\boldsymbol{r}}_{\hat{i}\bar{j}} = \mu_j \nabla U_{\hat{j}}\left(\boldsymbol{r}_{ij}\right), \tag{2b}$$

$$\ddot{\boldsymbol{r}}_{\bar{i}\hat{j}} = -\mu_j \nabla U_{\hat{i}}\left(-\boldsymbol{r}_{ij}\right), \tag{2c}$$

where μ_j denotes the gravitational parameter of body j gravitationally interacting with body i. For the explicit expression of the gravitational potentials, we have

$$U_{\bar{j}}\left(\boldsymbol{r}_{ij}\right) = \frac{1}{r_{ij}}, \tag{3a}$$

$$U_{\hat{j}}\left(\boldsymbol{r}_{ij}\right) = \frac{1}{r_{ij}} \sum_{l=2}^{\infty} \sum_{m=0}^{l} \left(\frac{R_j}{r_{ij}}\right)^l \times P_{lm}\left(\sin(\phi_{ij})\right)\left(C_{lm}^{(j)} \cos(m\lambda_{ij}) + S_{lm}^{(j)} \sin(m\lambda_{ij})\right), \tag{3b}$$

where R_j is the reference radius of the spherical harmonic expansion (usually the equatorial radius of body j), while ϕ_{ij} and λ_{ij} are latitude and longitude of body i with respect to body j, respectively. P_{lm} denotes the so-called associated Legendre polynomial of degree l and order m, and $C_{lm}^{(j)}$ and $S_{lm}^{(j)}$ are the spherical harmonic coefficients associated with body j and are a measure of the internal mass distribution. In Section 2.5, these properties are discussed in more detail in the context of the Jovian system.

2.2. Rotation Models

We treat Io to be in a perfectly tidally locked corotant state around Jupiter (i.e. $\lambda_{(\mathrm{Io,\,Jupiter})}$ is equal to zero in Eq. 3b), neglecting any periodic variations due to free and forced librations. While this assumption is in line with the majority of dynamical models (*e.g.* Lainey et al. 2004; Lari 2018), recent models sometimes include physical or geometric librations (*e.g.* Dirkx et al. 2016). Qualitatively, variations in the amplitude of the librations have an almost identical effect on the orbital evolution as the C_{20} and C_{22} gravity field coefficients. However, given the conceptual nature of this work, complexifying the model in this particular aspect can be safely omitted. Besides, assuming the moon to be in a corotant state, an analytical formulation for the tidal interactions between Jupiter and Io can be found, leading to simplified expressions for the tidal models.

2.3. Tidal Models

Tidal interactions and tidal dissipation, in particular, have a significant influence on the dynamics and long-term thermal-orbital evolution of the Jovian system (*e.g.* Lainey et al. 2009; Lari 2018). Physically, tides manifest themselves as deformations of the shape of a body and hence as variations of its gravity field. Kaula (1964) has been the first to provide an in-depth analysis of tidal effects by expanding the gravitational potential delineated in Eq. 3b. Besides this implicit approach, analytical models that explicitly include tidal interactions and dissipation in the dynamical model have been developed (Mignard 1979; Lainey et al. 2007, 2009). In essence, these models incorporate the time lag Δt between the position of the tide-inducing satellite and the tidal bulge on its primary,

$$\Delta t = \frac{T \arctan(1/Q)}{2\pi}, \tag{4}$$

which is a function of the period of the main tidal excitation T and the quality factor Q. For tides raised on the primary, $T = \pi/(\Omega - n_i)$, while for tides acting on a corotant satellite, $T = 2\pi/n_i$, where Ω and n_i are the spin frequency of the primary and the mean motion of the satellite, respectively (Lainey et al. 2009). The force received by body i of mass m_i as a result of the tides it raises on body j is equal to (Lainey et al. 2007):

$$\boldsymbol{F}_{\bar{i}\hat{j}} = -3\frac{k_2^j G m_i^2 R_j^5}{r_{ij}^7} \Delta t \left(2\frac{\boldsymbol{r}_{ij}}{r_{ij}} \frac{\boldsymbol{r}_{ij} \cdot \dot{\boldsymbol{r}}_{ij}}{r_{ij}^2} + \frac{\boldsymbol{r}_{ij} \times \boldsymbol{\Omega}_j + \dot{\boldsymbol{r}}_{ij}}{r_{ij}}\right), \tag{5}$$

where k_2^j, R_j, Δt, and $\boldsymbol{\Omega}_j$ are the Love number, equatorial radius of the body undergoing tidal deformation, the time-lag, and the angular velocity, respectively. However - since this analytic formulation requires a very high level of consistency between the orbital, rotational, and tidal dynamics - to correctly account for the tides raised on a satellite, the final term is usually simplified using $\boldsymbol{\Omega}_j = \boldsymbol{r}_{ij} \times \dot{\boldsymbol{r}}_{ij}/r_{ij}^2$ (i.e. essentially assuming the satellite to be in a corotant state), thus yielding an expression for purely radial tides. Murray & Dermott (1999) have found that the contribution of librational tides is exactly equal to 4/3 times the energy dissipated by radial tides, giving:

$$\boldsymbol{F}_{\bar{i}\hat{j}} = -3\frac{k_2^j G m_i^2 R_j^5}{r_{ij}^7} \Delta t \left(7\frac{\boldsymbol{r}_{ij}}{r_{ij}} \frac{\boldsymbol{r}_{ij} \cdot \dot{\boldsymbol{r}}_{ij}}{r_{ij}^2}\right), \tag{6}$$

where the superposition of radial (3) and librational (4) tides constitute the total factor (7) within the brackets. Finally, note that the resulting force is entirely radial, with the periodic contribution of librational tides having been averaged such that the same amount of energy is dissipated (Lari 2018).

2.4. Equations of Motion

The equations of motions are integrated numerically in a jovicentric frame with inertial axis orientation (ECLIPJ2000) using the TU Delft Astrodynamics Toolbox (tudat)[1] with in-depth explanations hereof given by Dirkx et al. (2019, 2022). Based on the preceding building blocks, a comprehensive expression for the equation of motion for a satellite i of mass m_i around its central planet of mass m_0 is given by

$$\begin{aligned}\ddot{\boldsymbol{r}}_i = {} & \nabla U_{0i}\left(\boldsymbol{r}_i\right) - \nabla U_{i0}\left(-\boldsymbol{r}_i\right) + \sum_{j=1, j\neq i}^{N} \nabla U_{ji}\left(\boldsymbol{r}_{ji}\right) - \nabla U_{j0}\left(-\boldsymbol{r}_j\right) \\ & + \frac{(m_0 + m_i)}{m_i m_0}\left(\boldsymbol{F}_{\bar{i}\hat{0}} - \boldsymbol{F}_{\bar{0}\hat{i}}\right) - \frac{1}{m_0} \sum_{j=1, j\neq i}^{N} \left(\boldsymbol{F}_{\bar{j}\hat{0}} - \boldsymbol{F}_{\bar{0}\hat{j}}\right),\end{aligned} \tag{7}$$

---

[1] Documentation: https://tudat-space.readthedocs.io.
Source code: https://github.com/tudat-team/tudat-bundle.

where $U_{ij}\left(\boldsymbol{r}_{ij}\right)$ is the combined gravitational potential (including the respective gravitational parameter) directly obtained from Eqs. 1 and 2, and $\boldsymbol{F}_{\bar{i}\hat{j}}$ is given by Eq. 5. In particular, when propagating the dynamics of Io using Eq. 7, the following comprehensive overview of models have been taken into account:

- the mutual spherical harmonic acceleration between Jupiter and Io, with Jupiter's gravity field expanded up to degree 12 and order 0, and that of Io up to degree and order 2,
- the mutual spherical harmonic accelerations between Io and Europa, Ganymede, and Callisto, with the gravity fields of all bodies expanded up to degree and order 2,
- the point-mass accelerations exerted by Saturn and the Sun,
- the acceleration exerted on Io due to tidal dissipation in Jupiter forced by Io,
- the acceleration on Io due to tidal dissipation in Io forced by Jupiter.

It must be stressed that while we propagate the state of Io, the trajectory of JUICE stems from the CReMA 5.1 trajectory[2], distributed by ESA in the form of SPICE kernels. Finally, in terms of celestial bodies, the scope of the analysis has been restricted to the mere propagation of the state of Io. Given that the orbital uncertainties of the remaining three Galilean satellites are significantly lower, as well as their moderate correlations with the initial state of Io (Fayolle et al. 2023), taking their states from the respective SPICE kernels is thus more than justified in the context of the conceptual nature of this work.

2.5. *Physical Characteristics of the Jovian System*

To date, the best estimation for the gravity field coefficients of the Galilean moons stems from flyby data of the Galileo mission and are limited to the J_2 and C_{22} coefficients of each moon (Schubert et al. 2004). However, as a notion of caution, Dirkx et al. (2016) mention that while the two coefficients could be determined independently for Io, for the other Galilean moons hydrostatic equilibrium - implying $J_2 = 10/3\ C_{22}$ - had to be assumed. Table 1 gives a comprehensive summary of the gravitational parameter GM and the unnormalised coefficients J_2 and C_{22} based on Schubert et al. (2004).

Table 1. Gravity results adapted from Schubert et al. (2004).

Body	GM $[km^3 s^{-2}]$	J_2 $(\times 10^6)$	C_{22} $(\times 10^6)$
Io	5959.91 ± 0.02	1859.5 ± 2.7	558.8 ± 0.8
Europa	3202.72 ± 0.02	435.5 ± 8.2	131.5 ± 2.5
Ganymede	9887.83 ± 0.03	127.53 ± 2.9	38.26 ± 0.87
Callisto	7179.29 ± 0.01	32.7 ± 0.8	10.2 ± 0.3

Concerning the gravity field of Jupiter, the first rigorous data-reduction of the Juno mission by Iess et al. (2018) has doubled the number of available zonal field coefficients to degree 12 - whilst also greatly reducing the respective uncertainties - which will be used throughout this work. Not being explicitly stated by Iess et al. (2018), the value for GM has been taken from Folkner et al. (2017). On a final note, realise that the tidal properties of the Galilean moons used in Eqs. 5 and 6 are poorly constrained. Solely the characteristics of Io have been determined by Lainey et al. (2009) to $k_2/Q = 0.015 \pm 0.003$. In a concurrent analysis, an estimate of $(1.102 \pm 0.203) \cdot 10^{-5}$ has been found for Jupiter's value of k_2/Q. Finally, Lainey et al. (2009) have found the period of the main tidal excitation for tides raised on Jupiter by Io to be equal to 23.3 rad/day, and Lari (2018) gives a value of 203.49 degrees/day for Io's mean motion.

3. Simulation of Optical Observations

In essence, the overall idea of space-based optical astrometry differs only marginally from its Earth-based counterpart: the position of an imaged celestial body - typically given as right ascension and declination - is determined with respect to an absolute reference frame (Arlot 2019). Nonetheless, given the relative proximity of space-based observers, the two respective data-reduction methods exhibit significant differences. Hence, this section first delineates the dominant sources of uncertainty of optical space-based astrometric observations in Section 3.1. Finally, Section 3.2 outlines different types of observation epoch selection algorithms alongside their respective underlying drivers.

3.1. *Optical Space-Based Astrometry*

According to the model applied by Tajeddine et al. (2013), three main sources of error constitute the overall uncertainty of space-based astrometric observations: errors within the pointing correction (σ_{p}), uncertainties related to determining the centre-of-figure (σ_{c}), and the positional accuracy of the spacecraft itself (σ_{sc}). First, σ_{p} accounts for the finite accuracy of the astrometric calibration of the orientation and pointing direction of the camera (Tajeddine et al. 2013). Second - also taking uncertainties within the shape model into account - σ_{c} delineates how well the position of the centre-of-figure can be reduced from the detectable limb of the satellite. Finally, σ_{sc} describes how the uncertainty in the position of the spacecraft directly propagates into the accuracy of the state of the moon. For the total observational uncertainty of space-based imaging expressed in right ascension α and declination δ, thus follows (Pasewaldt et al. 2012; Tajeddine et al. 2013):

$$\sigma_\alpha = \sqrt{\left(\sigma_{\mathrm{p}}^2 + \sigma_{\mathrm{c}}^2 + \sigma_{\mathrm{sc}}^2\right)} / \cos\delta, \tag{8a}$$

$$\sigma_\delta = \sqrt{\left(\sigma_{\mathrm{p}}^2 + \sigma_{\mathrm{c}}^2 + \sigma_{\mathrm{sc}}^2\right)}. \tag{8b}$$

3.1.1. Pointing Uncertainty

In practice, the pointing correction of the imaging subsystem is achieved using the catalogued positions of imaged reference stars - such as the Gaia DR2 and EDR3 catalogue (Gaia Collaboration 2018, 2021). However, since Tajeddine et al. (2013) base their applied reduction technique on the actual optical properties of space-based images (such as the camera's constant scale factors or errors in a star's position due to the projection of the image from the celestial sphere to the tangential observation plane of the camera), it falls short of the description of simulated uncertainties. To this end, Melman (2018) has modelled errors within the pointing correction using a theory for the accuracy of a star tracker by Liebe (1995). Thus, the uncertainty σ_{p} can be described as a function of the size of the field of view of the camera FOV, the achievable subpixel precision of the stars' position $\sigma_{\mathrm{extraction}}$, and the number of pixels and stars in the field of view, N_{pixels} and N_{FOV}, respectively:

$$\sigma_{\mathrm{p}} = \frac{FOV \cdot \sigma_{\mathrm{extraction}}}{N_{\mathrm{pixels}} \cdot \sqrt{N_{\mathrm{FOV}}}}. \tag{9}$$

---

[2] https://www.cosmos.esa.int/web/spice/spice-for-juice

For Cassini, Tajeddine et al. (2013) report a value of approximately 0.552 pixels for $\sigma_{\text{extraction}}$, which also seems a reasonable estimate for the imaging subsystem of JUICE, assuming similar data-reduction techniques. Since the pointing uncertainty is a function of the instantaneous number of background stars visible in the field of view (FOV), no absolute *a priori* uncertainty for the pointing correction is readily available. However, given that the overall uncertainty of space-based imaging will be mainly dominated by the error within the determination of the centre, with the σ_{p} about one and σ_{sc} around two orders of magnitude smaller, respectively (Melman 2018). Furthermore, given the quadratic contributions to the root in Eq. 8, we assume the number of background stars to be fixed to its average value - estimated to approximately 800 stars by Melman (2018).

3.1.2. Centre-of-Figure Uncertainty

To determine the uncertainty within the determination of the centre-of-figure (i.e. how well a given shape model can be fitted to the detectable limb of a satellite), Antreasian et al. (2005) have developed an expression that gives the uncertainty σ_{c} as a function of the apparent diameter d_a, and thus the position of the spacecraft with respect to the imaged satellite:

$$\sigma_{\text{c}}^2 = \sigma_{\text{min}}^2 + (C \cdot d_a)^2 \,, \tag{10}$$

where σ_{min} is a fixed weighting factor, and C is a scaling factor related to the moon's surface roughness. Originally applied to Cassini, Antreasian et al. (2005) propose using a value of 0.25 pixels for the minimum weight σ_{min} while using a value of C equal to either 0.02 or 0.01 for heavily cratered or smooth moons, respectively.

For Cassini, however, Melman (2018) finds poor agreement between the approach by Antreasian et al. (2005) (using the therein stated values for σ_{min} and C) and the values provided by Tajeddine et al. (2015) based on a novel but not further delineated limb-fitting scheme, with the found analytic expression (Eq. 10) yielding too pessimistic results. To this end, we have used the obtained uncertainties for the five Saturnian moons' declination by Tajeddine et al. (2015) as provided in the supplementary information[3] alongside the moons' instantaneous apparent diameter to fit the variable parameters within the model by Antreasian et al. (2005) using a non-linear least-squares algorithm (see Section 4.1). The individual fitted values for the five Saturnian moons analysed by Tajeddine et al. (2015) are presented in Table 2, together with the respective coefficient of determination. An in-depth outline of the fitting process as well as an analysis of the results can be found in Appendix A.

Table 2. Fitted values for the weighting factor σ_{min} and scaling factor C, as well as the resulting coefficient of determination R^2 for the five Saturnian moons delineated by Tajeddine et al. (2015).

Moon	σ_{min}	C	R^2
Tethys	0.087 ± 0.0011	0.00062 ± 0.00014	0.6345
Dione	0.083 ± 0.0010	0.00052 ± 0.00015	0.6735
Rhea	0.076 ± 0.0011	0.00077 ± 0.00009	0.6293
Iapetus	0.086 ± 0.0012	0.0014 ± 0.00013	0.7964
Phoebe	0.141 ± 0.0051	0.0021 ± 0.0011	0.4582

Given that the geometrical specifications of the corresponding field-of-views significantly differ between the imaging subsystems of Cassini and JUICE (see Table 3), we have to scale the limb-fitting uncertainty by Tajeddine et al. (2015) using a factor of $FOV_{NavCam}/FOV_{NAC} = 4/0.35$ to mimic the results that would have been expected when using a NavCam-like camera instead of Cassini's NAC. Using the averaged parameters given in Table 2, we find values of 0.095 pixels and 0.0014 for σ_{min} and C, respectively, which are approximately one order of magnitude lower than those originally proposed by Antreasian et al. (2005). On a final note, realise that this discrepancy in essence illustrates the level of improvement achieved over a time span of about ten years within photometric reduction techniques.

Table 3. Comparison of the camera specifications of Cassini's NAC (Narrow Angle Camera, Tajeddine et al. 2013) and JUICE's NavCam (Navigation Camera, Boutonnet et al. 2018).

Camera	Field-of-view [deg]	Resolution [pixels]
Cassini NAC	0.35 × 0.35	1024 × 1024
JUICE NavCam	4 × 4	1024 × 1024

3.1.3. Spacecraft Position Uncertainty

Finally, the overall achievable accuracy in the observed position of the satellite depends on the uncertainties in determining the spacecraft's position. According to Tajeddine et al. (2013), the influence of the spacecraft uncertainty on the uncertainty in the lateral position of the satellite can be expressed as:

$$\sigma_{sc} = \arcsin\left(\frac{\sigma_{S/C}}{D}\right), \tag{11}$$

where D is the distance between the spacecraft and the satellite, and $\sigma_{S/C}$ is the total uncertainty in the position of the spacecraft. For Cassini, Tajeddine et al. (2013) assume a position uncertainty $\sigma_{S/C}$ of 100 metres. Given the largely comparable tracking equipment of Cassini and JUICE outside of any flyby- or orbital phases, a position uncertainty of 100 metres seems to be a reasonable approximation for the expected accuracy of JUICE, as well. Nonetheless, note that the contribution of the uncertainty in the spacecraft position - about two orders of magnitude smaller than the limb-fitting error (Melman 2018) - to the overall uncertainty of space-based astrometry is almost entirely negligible.

3.2. Selection of Observation Epochs

Since both the overall uncertainty and the relative geometry of optical space-based astrometry are a function of the position of JUICE relative to the one of Io - and thus their respective orbits - the selection of epochs at which we simulate optical observations will have a significant impact on the orbital solution. Since the image-acquisition-planning for the NavCam instrument is not firmly chosen yet, potential recommendations for an effective observation scheme are of particular importance. Besides any influence of the outlined mission design, the changing observation geometry entails the need to define a set of viability criteria to dismiss any physically implausible observations, for instance, due to the presence of either Jupiter or the Sun in the camera's FOV. These constraints will be briefly delineated in Section 3.2.1. Further, in Section 3.2.2, we propose the implementation of four different algorithms for the selection of the epochs at which optical observations are to be simulated.

---

[3] http://cdsarc.u-strasbg.fr/viz-bin/qcat?J/A+A/575/A73.

3.2.1. Observation Schedule and Constraints

To date, the current mission design of JUICE stipulates an optical space-based astrometric observation schedule covering the period from Jupiter Orbit Insertion (July 2031) up to Ganymede Orbit Insertion (December 2034). Within this period, we have implemented an artificial imaging cadence of one observation per 30 minutes. However, from an observational point-of-view, only a limited number of all potential epochs is considered feasible, as well. As stated by Boutonnet et al. (2018), no images are to be taken during the 12 hours directly before and after the moment of closest approach of all lunar flybys performed by JUICE. Boutonnet et al. (2018) further constrains any observations by the following geometric conditions:

- a minimum Sun-Spacecraft-Moon angle,
- a minimum Jupiter-Limb-Spacecraft-Moon angle,
- a maximum Sun-Moon-Spacecraft angle (Phase angle).

By limiting the influence of other celestial bodies' brightness on the saturation of the digital imagining sensor, both the minimum Sun-Spacecraft-Moon and Jupiter-Limb-Spacecraft-Moon angles ensure sufficient visibility of background stars in the camera's FOV. Moreover, since a reasonable part of the visible surface of Io needs to be illuminated by the Sun to avoid erroneous fits of the satellite's limb, as well as to avoid loss of contrast due to imaging into direct sunlight, a maximum phase angle needs to be introduced (Cooper et al. 2014). While the minimum Sun-Spacecraft-Moon angle (30 degrees) and the maximum Sun-Moon-Spacecraft angle (130 degrees) have been fixed to constant values, the minimum Jupiter-Limb-Spacecraft-Moon angle depends on the apparent size of Jupiter. For an imaged size greater than 4 degrees, the minimum Jupiter-Limb-Spacecraft-Moon angle has been set to 5 degrees, while a distance to Jupiter's limb of 10 degrees is required otherwise. Finally, note that any other constraints given by Boutonnet et al. (2018) - such as the minimum number of pixels to be filled by the imaged satellite - have never constrained the observations.

3.2.2. Epoch Selection Algorithms

To investigate the influence of both the overall uncertainty and the relative geometry of space-based images, we propose four distinct epoch selection algorithms:

- a randomised approach,
- a geometry-driven approach,
- an uncertainty-driven approach,
- an uncertainty- and geometry-driven hybrid approach.

Trivially, an entire randomised selection - out of the total feasible subset - takes place when using the randomised approach. Hence, no priority is given to individual epochs, justifying the omission of any further explanation.

Different relative observation geometries are crucial to constrain the offset between a celestial body's COF and COM (Pasewaldt et al. 2012). Hence, given a certain number of (planned) observations, we expect improvements in the estimation of the formal errors of the COF-COM-offset for a diversified set of observation geometries. Owing to the number of feasible observations being constrained by the minimum Jupiter-Limb-Spacecraft-Moon angle (see Section 3.2.1) and the mostly equatorial observation geometry of JUICE, the along-track position of Io will be much less prominently observed than the radial or normal direction. Thus, to diversify the set of chosen observation geometries, we introduce a patterned grid of relative observation angles with the along-track axis of Io over the entire available range - 0 degrees up to 180 degrees, with values between 180 degrees and the 'full' circle's 360 degrees reduced by 180 degrees due to the periodicity of the cosine. Based on the total number of observations, the angular spread between two neighbouring points on the grid is evaluated. The relative geometry of an arbitrary epoch is used as initial entry to the grid, with the remaining entries given by the angular spread. Finally, epochs are selected based on the distinct points of the geometric grid.

As previously outlined in Section 3.1, the achievable uncertainty of optical space-based astrometric images is closely linked to the instantaneous observation geometry, in particular, the relative distance between JUICE and Io. Given otherwise similar estimation conditions, higher (absolute) accuracies, by definition, yield lower estimated formal errors (see Section 4.2). Hence, even though the exact estimation conditions will vary slightly, we expect improvements in the estimation of the formal errors of the COF-COM-offset if epochs at which we simulate optical space-based astrometry with lower associated (absolute) uncertainties are specified. We thus introduce an uncertainty-driven algorithm selecting the best X epochs purely based on their expected (metric) uncertainty, with the best X equal to the total number of observations. However, owing to the operational constraints of the NavCam - for instance observations of the reaming three moons for navigational purposes - a random selection is performed out of the $1.2X$ most accurate epochs, making our simulations more realistic and lenient in the choice of epochs.

Finally, we expect synergistic effects by merging the underlying ideas of the uncertainty and geometry-driven algorithms in a so-called hybrid approach. To this end, all feasible epochs are initially sorted according to their respective (absolute) uncertainty and grouped into N ascending subsets, with N equal to the ratio between the total number of feasible epochs and simulated observations. From the most accurate subset onward, the angular spread is evaluated per subset using an equally-spaced grid identical to the above-outlined one. However, in contrast to the prior geometry-driven approach, we permit a maximum allowed error margin of 10 per cent between the simulated and searched angle for an epoch to be successfully selected. Subsequently, any remaining angles (i.e. relative observation geometries nonexistent in the current, more accurate subset) are looked for within the following subset until either the angular grid is depleted or the iteration has reached the final subset. Given the latter case, the angular error margin is increased by 10 per cent, and all remaining epochs are re-grouped into M subsets - with M equal to the ratio of the number of all potentially left and simulated observations - followed by the next iteration of the algorithm. Whilst primarily an uncertainty-driven approach, by gradually loosening the maximum allowed angular error margin, we ensure the distribution of the epochs' observation geometries across the entire range of available relative angles with Io's along-track axis.

4. Determination of Orbits

In this section, we briefly describe how the solution for the orbit of Io is determined from simulated optical space-based astrometric observations. We present the mathematical foundations of 'full' orbit estimation, and generating and propagating covariance matrices in Sections 4.1 and 4.2, respectively. Subsequently, we argue for and against the use of different approaches to model the offset between the COF and COM in Section 4.4. Finally, we discuss how we constrain our analysis to the expected average level of uncertainty of Io's radio science solution using a suitable *a priori* covariance matrix in Section 4.3.

4.1. Orbit Estimation

Overall, orbit estimation tries to minimise the residuals between the observations and the respective numerically computed values (i.e. the observables predicted by the propagated equations of motion, see Section 2.4). Using a least-squares algorithm (*e.g.* Montenbruck & Gill 2000; Milani & Gronchi 2010), this can mathematically be defined as finding the set of estimated parameters $\boldsymbol{q}^{lsq}$ that minimises the so-called loss function:

$$J(\boldsymbol{q}) = \boldsymbol{\rho}^T \boldsymbol{\rho} = (\boldsymbol{z} - \boldsymbol{h}(\boldsymbol{q}))^T (\boldsymbol{z} - \boldsymbol{h}(\boldsymbol{q})), \tag{12}$$

where the vector $\boldsymbol{z}$ contains the computed observables and the non-linear function $\boldsymbol{h}(\boldsymbol{q})$ denotes the set of observations at identical points in time. The vector $\boldsymbol{q}$ usually contains the initial state $\boldsymbol{x_0}$ and any parameters $\boldsymbol{p}$ of interest that influence the dynamical or observational models (i.e. $\boldsymbol{q} = [\boldsymbol{x_0}; \boldsymbol{p}]$). By linearising the function $\boldsymbol{h}(\boldsymbol{q})$ with respect to a reference state $\boldsymbol{q}^{ref}$ we obtain the observations partials (or design) matrix $\boldsymbol{H}$, such that:

$$\rho \approx \Delta z - \boldsymbol{H}\Delta\boldsymbol{q} \quad \text{with} \quad \boldsymbol{H} = \frac{\partial \boldsymbol{h}(\boldsymbol{q})}{\partial \boldsymbol{q}^{ref}}, \tag{13}$$

where $\Delta\boldsymbol{q}$ and Δz are taken with respect to their respective reference values $\boldsymbol{q}^{ref}$ and $\boldsymbol{h}\left(\boldsymbol{q}^{ref}\right)$. Thus, the solution to the least-squares equation is given by (Montenbruck & Gill 2000):

$$\Delta\boldsymbol{q}^{\mathrm{lsq}} = \left(\boldsymbol{H}^T \boldsymbol{W} \boldsymbol{H}\right)^{-1} \left(\boldsymbol{H}^T \boldsymbol{W} \Delta z\right). \tag{14}$$

Realise that this equation is usually evaluated in an iterative process. Finally, we have introduced the weight matrix $\boldsymbol{W}$ to account for different levels of observation uncertainties. Usually, this weight matrix is set as a square diagonal matrix with $\boldsymbol{W}_{ii} = \sigma_{h,i}^{-2}$, implicitly assuming all uncertainties to be uncorrelated white noise with a Gaussian distribution.

4.2. Covariance Analysis

Given the conceptual nature of this work, we are mainly interested in the relative contribution of space-based astrometry to the orbital solution and the overall ability of optical observations to constrain the offset between the COF and COM of Io (see Section 4.4). To this end, the analysis in this work will be restricted to covariance analyses. Note that we have already implicitly introduced the covariance matrix as the first factor of the linear least-squares solution (see Eq. 14):

$$\boldsymbol{P} = \left(\boldsymbol{H}^T \boldsymbol{W} \boldsymbol{H}\right)^{-1}. \tag{15}$$

To obtain the formal errors σ_j of the estimated parameters at a later time t, the initial covariance matrix $\boldsymbol{P}(t_0)$ can then be used to compute the covariance at any time t (*e.g.* Fayolle et al. 2022):

$$\boldsymbol{P}(t) = [\boldsymbol{\Phi}(t, t_0); \boldsymbol{S}(t)]\, \boldsymbol{P}(t_0)\, [\boldsymbol{\Phi}(t, t_0); \boldsymbol{S}(t)]^T. \tag{16}$$

The state transition and sensitivity matrix - denoted by $\boldsymbol{\Phi}(t, t_0)$ and $\boldsymbol{S}(t)$, respectively - are given by:

$$\boldsymbol{\Phi}(t, t_0) = \frac{\partial \boldsymbol{x}(t)}{\partial \boldsymbol{x}_0}; \quad \boldsymbol{S}(t) = \frac{\partial \boldsymbol{x}(t)}{\partial \boldsymbol{p}}. \tag{17}$$

Finally, we have to stress that the results of covariance analyses must be treated with caution since they are known to provide an overly optimistic assessment of the found accuracy. It is crucial to distinguish between true and formal errors - only in the Utopian case that the applied dynamical and observational models are an ideal representation of reality, any formal errors given by a covariance analysis would be equal to the true errors of the system (*e.g.* Dirkx et al. 2019). For planetary ephemerides, Jones et al. (2015, 2020) estimate a true-to-formal-error ratio of about 2-3. However, when estimating dynamical parameters from tracking data, the additional positional uncertainty of the respective spacecraft directly propagates into the associated true-to-formal-error ratios. For the estimation of Mars' gravity field from tracking data of the Mars Reconnaissance Orbiter, for instance, Konopliv et al. (2011) have found substantially larger true-to-formal-error ratios (5-20), while for the second-degree Love-number they have found a ratio of approximately 10. Furthermore, owing to the tracking data of JUICE and Europa Clipper predominately obtained during the orbital phase around Ganymede and the many flybys of Europa, respectively, the absolute lack of flybys of Io leads to a significantly imbalanced data set. Given the indirect estimation of the state of Io, a substantial true-to-formal-error ratio of the radio science solution - potentially even surpassing the above-stated values - could still be reasonable. Finally, this point is further emphasised by the fact that - due to the high-accuracy tracking - potentially mismodelled dynamical effects will noticeably affect the estimation, resulting in an even higher true-to-formal errors ratio (Fayolle et al. 2022).

4.3. Constraining the Solution by Radio Science Uncertainty

Usually, some information on the *a priori* accuracy of the reference state used as the initial estimate of the linear least-squares algorithm is readily available. To incorporate this *a priori* covariance matrix $\boldsymbol{P}_0^{-1}$, Eq. 15 can be slightly expanded and thus takes the form:

$$\boldsymbol{P} = \left(\boldsymbol{P}_0^{-1} + \boldsymbol{H}^T \boldsymbol{W} \boldsymbol{H}\right)^{-1}. \tag{18}$$

By accounting for prior knowledge of the estimated parameters, *a priori* matrices stabilise problems for which the numerical inversion of $\boldsymbol{H}^T\boldsymbol{W}\boldsymbol{H}$ becomes strongly ill-posed. For instance, the indirect determination of Io's ephemeris via the Laplace resonance (see Section 4.2) poses such a problem.

To constrain the orbit determination of Io to the expected uncertainty of the radio science solution - omitting the rigorous implementation of the radiometric tracking scheme of JUICE and Europa Clipper - we want to mimic the resulting (average) propagated formal errors arising from a radiometric tracking set-up similar to the one presented by Fayolle et al. (2023) within our *a priori* knowledge strategy. To this end, we have extended a method by Lainey et al. (2007), originally used to fit the initial state of the Martian moons to their respective ephemerides. In particular, we propose a twofold approach - while the first step is an exact replica of the approach by Lainey et al. (2007), the second part slightly extends the scope in order to mimic the propagated formal radio science errors.

First, we fit the initial state of Io to the NOE-5-2021[4] ephemerides of the Jovian system using a 'full' estimation framework (see Section 4.1). Following Lainey et al. (2007), we treat the respective ephemeris states as simulated observables with no assigned weights to mitigate any discrepancies between the dynamical model and the ephemeris solution. Second, the same set-up - now using the updated initial state - is used to obtain the formal errors of Io's state using a covariance analysis. However, while no weights are assigned to the observables

---

[4] https://ftp.imcce.fr/pub/ephem/satel/NOE/JUPITER/.

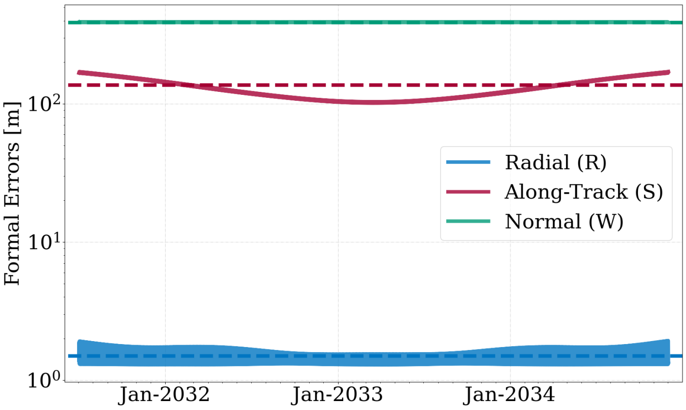

Fig. 1. Evolution of the formal *a priori* radio science uncertainties in the position of Io over the duration of the Jovian orbital phase of JUICE. Dashed lines indicate the average values by Fayolle et al. (2023).

within the ‘full’ state estimation, we have now iteratively chosen the observables’ weights such that the resulting (average) propagated formal errors are almost identical to those arising from a radiometric tracking set-up similar to the one presented by Fayolle et al. (2023). Using the therein found average uncertainties in radial ($\sigma_R = 1.5$ m), along-track ($\sigma_S = 137$ m), and normal ($\sigma_W = 387$ m) direction of the state of Io, the expression $\sqrt{n} \times [\sigma_R; \sigma_S; \sigma_W]$ yields a reasonable initial estimate for the implemented weights, where n is the total number of simulated observations. Figure 1 visualises the propagated formal errors (obtained via Eq. 16) of the resulting *a priori* covariance matrix.

However, it has to be stressed that - using the above-described strategy - our estimation is limited to the state of Io. While the computed *a priori* information accounts for the (static) uncertainties in the other moons’ states, we merely mimic any influence that the propagated uncertainties in these states could have on the covariance of Io. Moreover, we explicitly ignore any contribution space-based astrometry of Io might have to the solution of the remaining Galilean satellites, potentially leading to significant decorrelations of the respective initial states. However, given the conceptual nature of this work, we can reasonably neglect these influences. Nevertheless, note that the resulting formal errors for Io might be slightly too optimistic.

So far, we have merely considered the formal uncertainties given by the estimation set-up used by Fayolle et al. (2023). Yet, as previously highlighted in Section 4.2, we expect the true errors of Io’s radio science solution to be significantly greater. Hence, in Section 5.3, we will explicitly analyse the impact of a non-unity true-to-formal-error ratio on its ability to constrain the orbital solution of Io. The contribution c_q of the *a priori* information to the solution of each estimated parameter will be evaluated as follows (*e.g.* Floberhagen 2001; Fayolle et al. 2022):

$$c_q = \boldsymbol{I} - \boldsymbol{P}\boldsymbol{P}_0^{-1}, \tag{19}$$

where $\boldsymbol{I}$ is the identity matrix, while $\boldsymbol{P}$ and $\boldsymbol{P}_0^{-1}$ denote the estimated and *a priori* covariance matrix. A c_q equal to nought indicates that the respective parameter’s estimation is based on the provided *a priori* information, while a value of unity implies that it relies solely on the observations.

4.4. Modelling of the COF-COM-Offset of Io

In general, the offset between the centre-of-figure (COF) and centre-of-mass (COM) of a celestial body is expressed as a constant vector in a body-fixed frame. Hence, the mathematical representation of the COF-COM-offset of Io is *de facto* perfectly decoupled from any assumed shape model. While the choice of the orientation of the body-fixed reference frame is entirely arbitrary, given the previously discussed geometric implications with the observability of the along-track position of Io (see Section 3.2.2), the body-fixed RSW-frame has been found to be especially suitable to express the COF-COM-offset of Io. The RSW-frame is defined such that the x-axis radially points from Io to Jupiter (R), the y-axis is tangentially aligned with Io’s along-track direction (S), and the z-axis normally completes the reference frame (W). Usually, the offset between the COF and COM enters the equations of motion by way of the gravity field. In particular, the body-fixed position of any celestial body’s COM with respect to its COF is related to its unnormalised gravity field coefficients of degree and order one (C_{10}, C_{11}, and S_{11} - with S_{10} equal to zero, by definition) as follows:

$$\boldsymbol{r}_{\mathrm{COM}} = \left[\begin{array}{ccc} RC_{11} & RS_{11} & RC_{10} \end{array}\right], \tag{20}$$

where R is the mean radius of the celestial body of interest. Rearranging Eq. 20 thus yields an expression for the COF-COM-offset in terms of non-zero degree and order one gravity field coefficients that can be readily implemented in the dynamical model of Io (see Section 2). However, owing to the choice of gravitational, rotational and tidal models, it has been found that a gravitational representation of the COF-COM-offset of Io leads to issues with the consistency of the dynamical model. To this end, it is crucial to stress the general assumption of Eq. 20 - instead of the COM, the COF is now being treated as the ‘new’ origin of the body-fixed frame. Thus, while we obtain a consistent description of a body’s gravitational dynamics, by shifting the body-fixed frame-origin to the COF, non-zero degree and order one gravity field coefficients introduce an artificial discrepancy to the implemented analytical tidal model (see Section,2.3), developed with respect to a body’s COM. For Io, changing the origin of the underlying frame indirectly leads to variations in the energy dissipated into its orbit via the tidal interaction with Jupiter. For long propagation times, this discrepancy in orbital energy results in large mismatches in the orbital position. Hence, we had to discard this modelling approach.

Retaining the underlying idea of modelling the COF-COM-offset of Io as a constant vector in Io’s body-fixed RSW-frame, instead of altering the properties of the dynamical model, we introduce a difference between the models used within the simulation of observations and state propagation. Thus, while entering the observation equation, the COF does not influence the dynamical equations of motion. Mathematically, this is expressed as:

$$\boldsymbol{r} = \tilde{\boldsymbol{r}}_{\mathrm{Io}}(t) - \boldsymbol{r}_{\mathrm{sc}}(t_{\mathrm{obs}}) \quad \text{with} \quad \tilde{\boldsymbol{r}}_{\mathrm{Io}}(t) = \boldsymbol{r}_{\mathrm{Io}}(t) + \boldsymbol{R}(t)\,\boldsymbol{r}_{\mathrm{COF}}, \tag{21}$$

where $\boldsymbol{r}$ is the position of Io’s COF with respect to JUICE. Furthermore, $\tilde{\boldsymbol{r}}_{\mathrm{Io}}(t)$ and $\boldsymbol{r}_{\mathrm{Io}}(t)$ are the position of Io’s COF and COM, respectively, both being expressed in a frame with inertial orientation. Thus, their relationship is expressed using the constant offset-vector in a body-fixed frame - $\boldsymbol{r}_{\mathrm{COF}}$ - which is rotated from an Io-fixed to an inertial reference frame using a suitable rotation matrix $\boldsymbol{R}(t)$. Finally, $\boldsymbol{r}_{\mathrm{sc}}(t_{\mathrm{obs}})$ denotes the position of JUICE, with the difference $t_{\mathrm{obs}} - t$ being equal to the observation’s light-time. In essence, this process explicitly accounts for the offset between the observed COF and propagated COM, unlike the implicit estimation framework typically applied to space-based astrometric observations. Since the offset between Io’s COF and COM has so far not been estimated, by design, optical observations are always treated as being taken

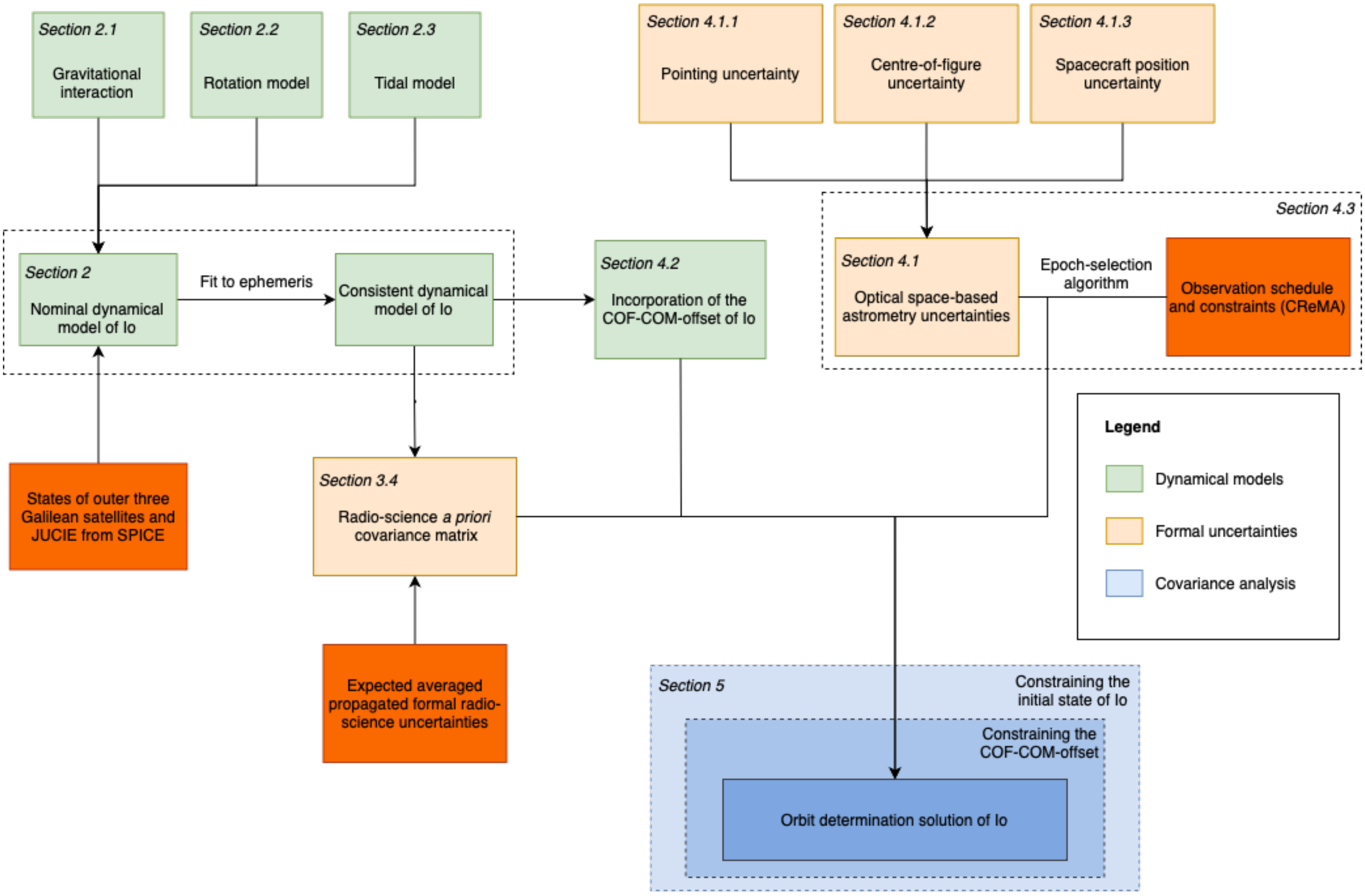

Fig. 2. Flowchart summarising the methodology followed in this work.

with respect to the COF. Yet, any optical observables are implicitly treated as being taken with respect to the imaged body's COM introducing a discrepancy between the observation and estimation models. However, by explicitly estimating the offset between the COF and COM alongside the initial state of Io, we eliminate the model-discrepancy, thus potentially improving the overall orbital solution.

Finally, it has to be reiterated that the results presented in Section 5 have not been obtained using 'full' orbit estimations but are limited to the formal errors arising from mere covariance analyses. In particular, we have evaluated the following parameters over a single, global estimation arc:

- initial state in a jovicentric frame,
- offset between the COF and COM in a body-fixed frame.

Since we simulate observations of the right ascension and declination of the celestial position of Io - its COF to be precise - with respect to JUICE, to estimate the discrepancy between the COF and COM, the following partials have to be added to the design matrix (see Section 4.2):

$$\frac{\partial(\alpha,\delta)}{\partial \boldsymbol{r}_{\mathrm{COF}}} \rightarrow \boldsymbol{H}. \tag{22}$$

While the derivation of such partials is far from trivial, conceptually, the estimation of offset between the COF and COM and the estimation of the body-fixed position of a ground-station are identical. Hence, the required partials are readily available (see *e.g.* Montenbruck & Gill 2000).

5. Results

As illustrated by our flowchart in Figure 2, we have initially delineated the different dynamical models used to propagate the state of Io (see Section 2). Subsequently, the state of Io has been fitted to the NOE-5-2021 ephemeris in order to obtain a consistent representation of its dynamics, followed by an outline of the approach used to constrain our analysis to the averaged propagated radio science formal errors - that would arise from a radiometric tracking set-up similar to the one used by Fayolle et al. (2023) - via a suitable *a priori* covariance matrix (see Section 4.3). An analytical model for the computation of the uncertainties associated with optical space-based observations has subsequently been implemented and optimised using past imagining-data obtained by Cassini (see Section 3.1). By casting these analytically evaluated uncertainties, the relative observation geometry, and the observational viability criteria into four different types of epoch selection algorithm (see Section 3.2), we have simulated optical space-based observations that are going to be used to generate the results of our covariance analyses discussed within this section. We analyse the formal errors in the estimation of the offset between the COF and COM of Io obtained using the previously delineated orbit-determination algorithm in Section 5.2, followed by a discussion of the impact of the true-to-formal-error ratio of the *a priori* radio science solution on the estimation's overall ability to constrain the COF-COM-offset and the orbital solution of Io in Section 5.3. First, however, Section 5.1 outlines the influence of different observation geometries on the quality of the obtained orbital solution.

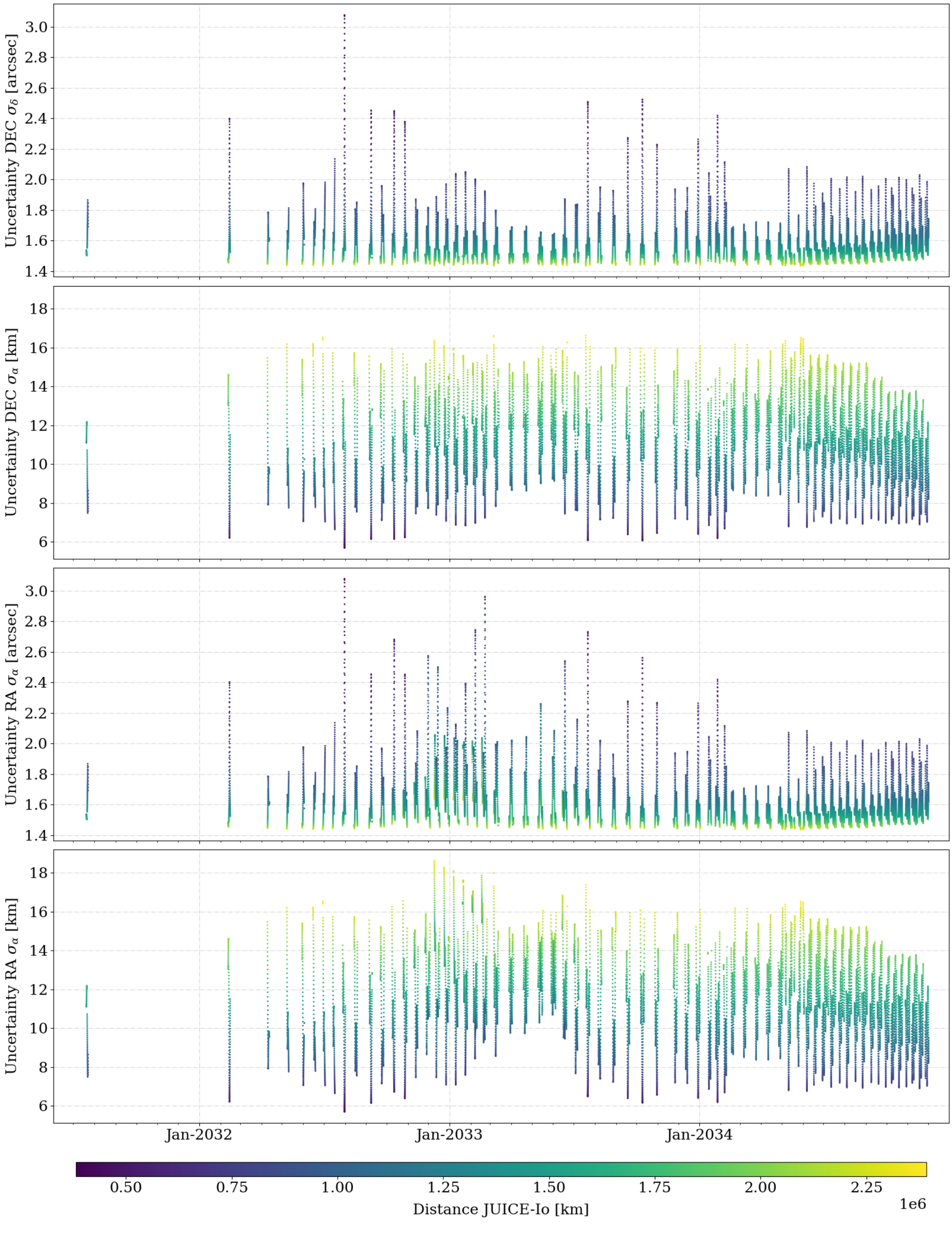

Fig. 3. Relative and absolute (metric) uncertainty of space-based astrometry in right ascension (RA) and declination (DEC) for all potentially feasible epochs. Feasibility has been determined according to the previously defined viability criteria (see Section 3.2). The positions to calculate the distance between JUICE and Io have been taken from the associated SPICE kernel and the propagated orbit, respectively.

5.1. Contributions of Different Observation Geometries

As discussed in Section 3.2.2, four different algorithms for the selection of the epochs at which space-based astrometric observations are to be simulated have been implemented - a purely randomised approach, a geometry-driven approach, an uncertainty-driven approach, and a hybrid approach. To characterise their underlying drivers, we first analyse the overall relationship between the observation geometry and the absolute optical uncertainty in Section 5.1.1, followed by a detailed discussion of the general behaviour of the relative observation geometry in Section 5.1.2. Finally, the respective contributions in terms of absolute uncertainty and observation geometry are analysed in Section 5.1.3.

5.1.1. Observation Geometry - Absolute Uncertainties

Constraining the number of potential observations by the previously discussed observation viability criteria (see Section 3.2.1) results in a total of about 15,000 feasible - i.e. all constraints being met - epochs. We can group them into 70 distinct arcs. Over the entire duration of the Jovian orbital phase of JUICE - not to be confused with the orbital phase around Ganymede - this corresponds to a reduction of potential space-based astrometric observations by about 75 per cent (i.e. space-based astrometry is only feasible over 25 per cent of the total duration of the orbital phase around Jupiter).

Given the instantaneous observation geometry, in particular the distance between JUICE and Io, we simulate an optical data reduction pipeline for the remaining astrometric observations using Eq. 8, yielding uncertainties in right ascension and declination for Io over time, visualised in Figure 3. By definition (see Eq. 8), errors in right ascension are always greater than or equal to those in declination, leading to elongated uncertainty ellipses for inclined orbits of JUICE. Overall, optical uncertainties range from a baseline of around 1.5 arcsec to slightly more than 3.0 arcsec, or approximately 6 km up to 18 km, expressed metrically using simple trigonometry. The expected errors are consistent with the range of values used by Dirkx et al. (2017), even though these were only rough estimates.

In particular, Figure 3 exhibits two general trends - first, uncertainties in radians increase with decreasing proximity of JUICE to Io, and second, the most erroneous relative observations correspond to the lowest absolute (metric) uncertainties. Via the apparent diameter of Io, the limb-fitting uncertainty is indirectly related to the distance to JUICE - the further away one takes an image, the smaller the diameter and hence the limb-fitting error. If we had moreover rigorously modelled the number of background stars, this effect would have been even slightly more pronounced. More stars are expected to be visible if Io covers a smaller fraction of the FOV. However, as we distinctively see in Figure 3, this is more than compensated for in terms of absolute uncertainties by an antagonistic effect, with closer distances directly translating to lower metric errors.

5.1.2. Observation Geometry - General Behaviour

As already briefly touched upon in Section 3.2.2, besides the influence of the distance between JUICE and Io on the overall error budget, Pasewaldt et al. (2012) have highlighted that different relative observation geometries of the images being taken are crucial to constrain the offset between the COF and the COM. To this end, we have analysed the relative observation geometry between JUICE and the body-fixed RSW-frame of Io with each

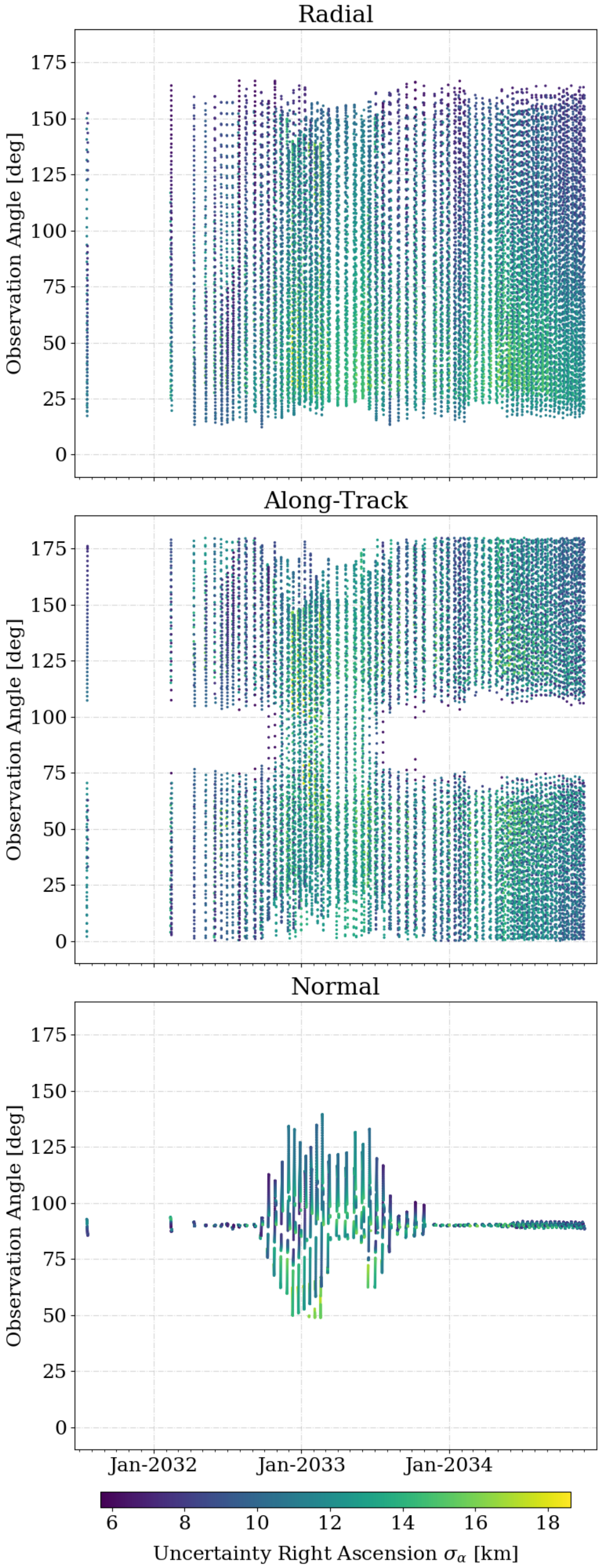

Fig. 4. Behaviour of the relative observation geometry between JUICE and the body-fixed axes of Io (radial, along-track, and normal) over the duration of the Jovian orbital phase. Observations have been filtered according to the previously defined viability criteria (see Section 3.2).

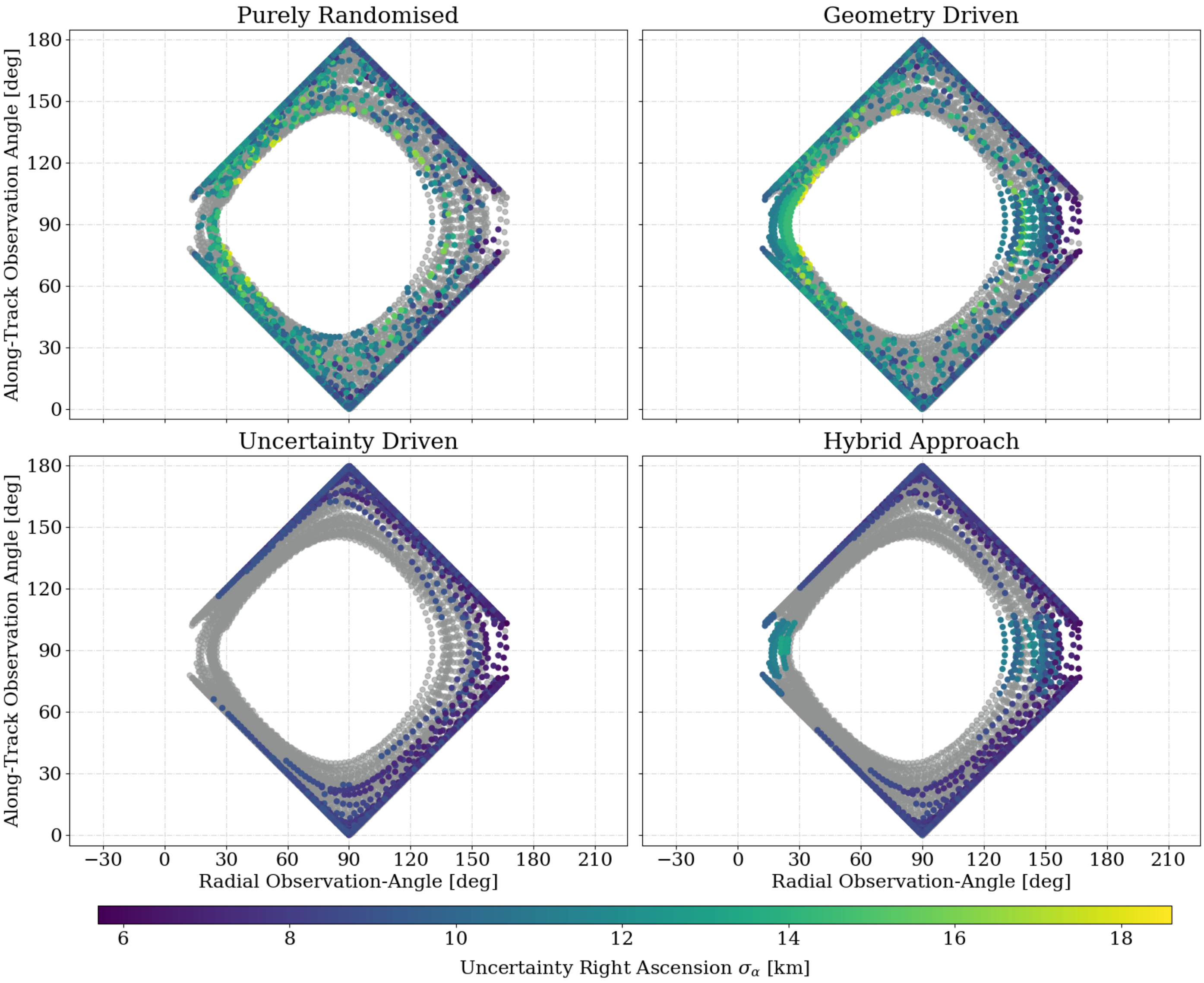

Fig. 5. Two-dimensional relative observation geometry of the radial and along-track contributions to the COF-COM-offset of Io (in grey). Each subplot exemplary illustrates the effect of the four proposed epoch-selection algorithms (see Section 3.2.2) using a total of 2,560 simulated observations. Selected epochs are highlighted as a function of the respective expected uncertainty in the satellite's right ascension.

of the three subplots in Figure 4 illustrating the observation angle with one individual axis (radial, along-track, or normal) over time. For vast parts of the orbital stage of JUICE, its orbit will closely coincide with the orbital plane of the Galilean moons. The high-inclination phase of JUICE is the only exemption to this approximation. Over 260 days - from October 2032 to August 2033 - the inclination of the spacecraft's orbit with respect to the Jovian equatorial plane is steadily increased up to about 22 degrees (Grasset et al. 2013). Hence, the observation angle with the normal (i.e. out-of-plane) axis of Io is usually equal to approximately 90 degrees, with values significantly deviating for non-zero inclinations during the high-inclination phase (see Figure 4). Outside of the high-inclination phase, we can thus treat the analysis of our problem as essentially being two-dimensional and focus on the observability of both the radial and along-track components of the offset.

Qualitatively, over the entire duration of the Jovian orbital phase, any potential radial contribution to the offset between the COF and COM of Io is observable to at least some degree. Since relative observation angles never approach the respective blind spots - either 0 degrees or 180 degrees - by a reasonable margin, any observation is thus sensitive to radial COF-COM-offsets. Unlike with the normal component, the high-inclination phase is not discernible from the data, with the angle visually not being influenced by an additional observation dimension. Moreover, we cannot observe any relation between the relative observation geometry and the associated uncertainties.

Neglecting the third dimension outside the previously identified high-inclination phase, no 'perfect' observations (i.e. observations encompassing a right angle with respect to JUICE) of the COF-COM-offset's along-track component are ever possible. The prominently centred white space in Figure 4 rigorously underlines this lack of observations during the planar parts of the Jovian orbital phase. Given the two-dimensional problem, these missing epochs correspond to an observation geometry with Jupiter, Io, and JUICE almost perfectly linearly aligned with respect to each other. Since the brightness of Jupiter would render any of these observations useless, they have been filtered by the Jupiter-Limb exclusion angle constraint (see Section 3.2). Only during the high-inclination phase - when JUICE either has a top-down or bottom-up view of Io, without Jupiter obstructing the FOV - 'perfect' observations of the along-track contribution are possible. Thus, the high-inclination phase exhibits significantly different behaviour than the planar parts of the Jovian orbital phase. Again, no relation between the relative observation geometry and the associated uncertainties is discernible.

While any radial or normal contributions to the COF-COM-offset are well observable over the entire duration of the orbital phase around Jupiter, outside of the high-inclination phase, the along-track component will be least observable. Since the minimum Jupiter-Limb-Spacecraft-Moon angle has motivated our particular choice of reference frame (see Section 3.2.2), this behaviour has already been anticipated. However, by design, this yields a single, poorly 'probed' component of the COF-COM-offset. Hence, circling back to the previously introduced argumentation by Pasewaldt et al. (2012), to best constrain the offset between the centre-of-figure and centre-of-mass of Io, the high-inclination phase is thus crucial since it allows for a complete range of different observation geometries.

5.1.3. Observation Geometry - Epoch Selection Algorithms

The two-dimensional relative observation geometry of the radial and along-track with respect to JUICE are provided in Figure 5 for the four proposed epoch-selection algorithms (see Section 3.2.2) using an exemplary set of 2,560 observations. Realise that owing to their lenient implementation, this is no absolute representation of any of the four methods but serves as a mere illustration of the overall trends. On a general note, epochs on the edges of the imaginary square are representative of a perfectly planar observation geometry (i.e. epochs outside of the high-inclination phase). Epochs geared towards the square's centre, however, indicate the increasing three-dimensionality of the problem and thus higher inclinations. Unsurprisingly, no trend in either uncertainty or geometry is visible within the purely randomised approach.

The geometry-driven approach, however, exhibits a clustering of observations centred around an observation angle with the along-track direction of 90 degrees, hence during the high-inclination phase. These epochs have been identified as essential to ensure an equally spaced geometric spread of the observations (see Section 5.1). Besides a clear improvement in the relative observation geometry of Io, however, we cannot discern any obvious differences to the randomised algorithm, neither within the associated uncertainties nor the ratio of observations between the high-inclination and Jovian orbital phase.

In contrast, the uncertainty-driven method selects a significant number of epochs outside of the high-inclination phase, identifiable by the visible grouping of observations along the edges of the imaginary square. Owing to the underlying algorithm, we conclude that epochs during the planar part of the Jovian orbital phase tend to have substantially lower associated uncertainties than those during the high-inclination of JUICE. We can explain this particular trend by two main reasons. First, owing to the direct relation between the declination of observations and the respective uncertainty in right ascension (see Eq. 8), any observation with a non-zero inclination will have a higher uncertainty given an otherwise identical geometry. When plotted as a function of the uncertainty in declination - instead of right ascension as is in Figure 5 - we have observed almost identical behaviour in the selected range of associated errors, further underlining this particular argumentation. Second, JUICE will perform a series of flybys around Callisto towards the end of the high-inclination phase (Grasset et al. 2013), leading to an increased mean distance - and thus smaller relative, yet greater absolute errors - of JUICE with respect to Io.

The proposed hybrid approach is essentially a combination of the two previously discussed geometry and uncertainty-driven algorithms (see Section 3.2.2). This relationship is clearly reflected in the data shown in Figure 5, as well. Owing to their favourable uncertainties, the majority of selected epochs still lie close to the edges of the imaginary square and hence during the planar parts of the Jovian orbital phase. Nevertheless, a significant number of observations is selected during the high-inclination phase. The associated observation angles are prominently centred around an observation angle with the along-track direction of 90 degrees, even though they possess a comparably higher absolute uncertainty.

Finally, we want to highlight that the plotted data of both the uncertainty-driven and the hybrid approach underline another distinct feature of the problem at hand - on the right side of the plot, where the corner of the imaginary square should be, we discern a series of points that one can describe as seemingly trickling down from the top half of the plot to the lower one. They all exhibit one of the lowest uncertainties of all feasible observations whilst simultaneously having a rare, but favourable - inclined and with close proximity to Io - observation geometry, making these points particularly beneficial to the estimation.

5.2. Formal Errors in the COF-COM-Offset

To assess how well the individual approaches cope with constraining the offset between the COF and the COM, we analyse their respective performances in terms of achievable formal errors as a function of the total number of observations (see Figure 6). Having limited our work to mere covariance analyses - instead of performing 'full' estimations - the formal errors in the COF-COM-offset are almost entirely independent of the offset's chosen value within the simulation of observations. Since, from a probability point of view, a three-dimensional COF-COM-offset of nought is the statistical best guess, a discrepancy of zero has been implemented and used throughout the entire work. Exploiting the realistic (i.e. slightly lenient) implementation of the respective algorithms, we have performed a rigorous Monte-Carlo analysis with each of the data points in Figure 6 representing the average value of 100 different covariance analyses for individual combinations of simulated epochs. In particular, two general trends are observable. First, an increase in the total number of observations always leads to lower formal errors, independent of the chosen algorithm, with the hypothetical use of all available epochs serving as the theoretical overall baseline. Second - trivially - the absolute difference in formal errors between the individual approaches is reduced for an increasing number of observations. Finally, while the relative differences similarly decrease as a function of the number of observations, Figure 6 shows that the final ratios nevertheless significantly differ from zero, underlying the high potential of suitable epoch selection algorithms even for high numbers of observations.

As a first approximation, the four algorithms can be divided into two groups based on their achievable formal errors - with the random and geometry-driven, as well as the uncertainty-driven and hybrid algorithms performing roughly similarly. This trend is especially pronounced for the behaviour of the formal errors in the normal direction. We find that the relative observation geometry has a negligible effect on the obtainable normal solution - which confirms our preliminary conclusion drawn in Section 5.1. Effectively, this decouples the out-of-plane contribution from that of the in-plane direction. Being essentially purely

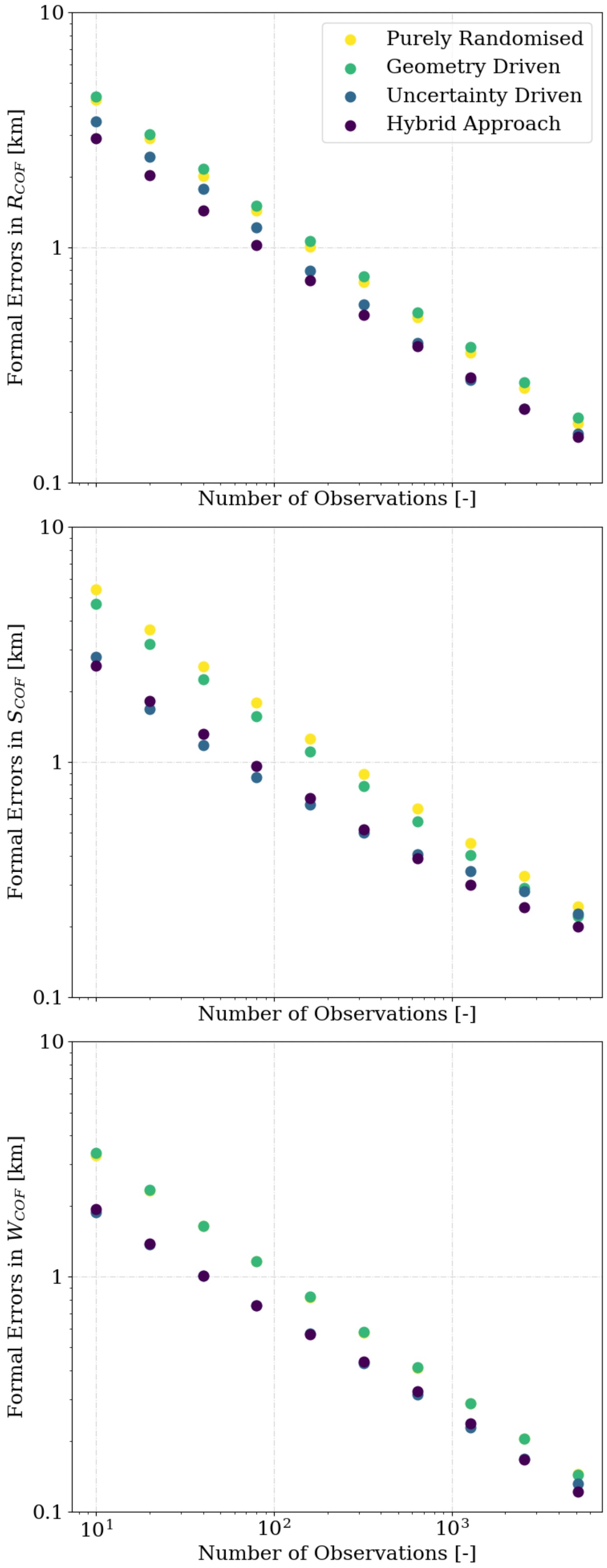

Fig. 6. Three-dimensional Monte-Carlo analysis of the formal errors in the estimation of the offset between the COF and COM for the four different selection algorithms in radial (R), along-track (S), and normal (W) direction as a function of the number of observations. Each data point represents the average value of 100 distinct covariance analyses.

uncertainty-driven, initial improvements in the estimation of the normal COF-COM-offset lie around 43 per cent (from 3.35 km to 1.9 km for ten different observations), with values gradually - yet slowly - approaching for increasing numbers of observations. Nonetheless, we can still observe improvement-ratios of approximately 21 per cent (from 290 m to 228 m) and 16 per cent (from 144 m to 121 m) for 2560 and 5120 observations, respectively.

For the two in-plane directions - radial and along-track - we find that the absolute uncertainty of the individual observations is the primary driver behind constraining the COF-COM-offset, with the relative observation geometry acting as a secondary criterion. Significant improvements between 30 and 50 per cent (for 10 observations), 27 and 34 per cent (for 1280 observations), and 17 and 18 per cent (for 5120 observations) in radial and along-track direction, respectively, are observable for the two distinct groups. Compared to the purely random selection, the geometry-driven approach performs as expected - lowering the error in the along-track direction at the almost negligible expense of a minor decline in the radial uncertainty. The hybrid algorithm, in comparison with the uncertainty-driven approach, surprisingly, exhibits an entirely contrary behaviour - significantly lowering the radial error while slightly raising the along-track one.

While, at first glance, not in line with the prior analysis, this can however be explained by the presence of the previously highlighted - ‘trickling’ - epochs exhibiting one of the highest accuracies whilst simultaneously having a favourable observation geometry in the chosen (uncertainty-driven) subset of observations (see Section 5.1.3). Having a similar observation geometry, not all of those epochs are thus chosen by the hybrid approach, leading to a slight degradation of the formal error. Nonetheless, perfectly in line with our prior conclusions, we find that optimising observation geometry of the selected epochs leads to a more circularised uncertainty ellipse, with errors in radial and along-track direction mutually approaching. On a final note, the three-dimensional ellipse of the hybrid approach, however, is never spherical but remains oblate in the out-of-plane component.

As of yet, we have indirectly assumed any influence of the temporal spread of the simulated observations over the time span of the Jovian orbital phase to be entirely negligible. To test this hypothesis, we have estimated the formal errors in the offset between Io’s COF and COM for different numbers of observations using a purely randomised approach as well as an algorithm that ensures a reasonable level of temporal spread averaged (see Table 4). We find that differences between the formal errors in the COF-COM-offset - with and without implementing an artificial temporal spread in the selection of epochs - are not greater than a few metres. Note that the most prominent absolute difference of 18 metres (R - 20 observations) equals a relative difference of less than one per cent and therefore negligible. With increasing numbers of observations, the differences either disappear entirely or become insignificant. The initial assumption to omit any temporal influence on our analysis is thus more than justified.

Concludingly, our analysis of the above-presented results has highlighted the high level of effectiveness of the hybrid approach - which will thus be chosen as exclusive epoch selection algorithm for the remaining results. Already low numbers of astrometric images (80 observations) yield low formal errors in the determination of the COF-COM-offset of about 1 kilometre - about one quarter of the number of observations required to obtain comparable uncertainties when randomly selecting epochs. Notably, for substantially higher numbers of observations, a hybrid hypothetical best-case scenario with formal uncertainties of approximately 200 metres and about 100 metres in the in-plane and out-of-plane directions, respectively, is achievable. How-

Table 4. Influence of temporal spread on the quality of the estimation. Formal errors averaged over 100 different combinations of randomly selected epochs for a total of 20 and 2560 observations are given in the top and bottom of the table, respectively.

Direction	Formal Errors with Time-Spread [km]	Randomised Formal Errors [km]
Radial (R)	2.920	2.902
Along-Track (S)	3.673	3.677
Normal (W)	2.318	2.319
Radial (R)	0.252	0.252
Along-Track (S)	0.328	0.329
Normal (W)	0.205	0.205

ever, less observations are to be expected. For the four regular Saturnian moons Tethys, Dione, Rhea, and Iapetus, a total of 5240 astrometric images has been taken (Tajeddine et al. 2015), equal to an average number of 1310 observations per moon. For Io, this number would thus translate to realistically attainable formal uncertainties of no more than 300 metres.

5.3. Impact of the Quality of the Radio Science Solution

So far, our analyses have been constrained to the expected uncertainty levels for Io's position based on a joint JUICE-Europa Clipper radio science analysis. While those are formal errors, however, recall that Jones et al. (2015, 2020) have estimated a true-to-formal-error ratio of about three for planetary ephemerides, with higher ratios up to 20 having been found by Konopliv et al. (2011) for the estimation of Mars' gravity field from spacecraft tracking data. Given the limited, indirect determination of the state of Io from a significantly imbalanced data set and the ill-posed inversion of the high-accuracy data, substantially greater ratios are to be expected (see Section 4.2). Mathematically, we can express the scaling of the formal errors σ_i and σ_j (correlated by a factor ρ_{ij}) and all associated covariance elements $\boldsymbol{P}_{ij}$ of a covariance matrix $\boldsymbol{P}(t)$ of size $n \times n$ as

$$\boldsymbol{P}(t) \rightarrow K\left[[\boldsymbol{\Phi}(t,t_0)\,;\boldsymbol{S}(t)]\,\boldsymbol{P}(t_0)\,[\boldsymbol{\Phi}(t,t_0)\,;\boldsymbol{S}(t)]^T\right], \tag{23a}$$

$$\boldsymbol{P}_{ij} \rightarrow \rho_{ij}\sqrt{K}\sigma_i\sqrt{K}\sigma_j = \rho_{ij}K\sigma_i\sigma_j \quad (i,j = 1\ldots n), \tag{23b}$$

$$\sigma_i \rightarrow \sqrt{K}\sigma_i \quad \text{and} \quad \sigma_j \rightarrow \sqrt{K}\sigma_j. \tag{23c}$$

The constant factor K is equal to the square of the true-to-formal-error ratio. Without loss of generality, we can further simplify the expression for a linearly scaled *a priori* covariance matrix to

$$\boldsymbol{P}(t) \rightarrow [\boldsymbol{\Phi}(t,t_0)\,;\boldsymbol{S}(t)]\,[K\boldsymbol{P}(t_0)]\,[\boldsymbol{\Phi}(t,t_0)\,;\boldsymbol{S}(t)]^T\,. \tag{24}$$

Any radio science true-to-formal-error ratio is thus incorporated by linearly scaling the original *a priori* covariance matrix $\boldsymbol{P}_0$. This scaled matrix will have two distinct effects on the ability to constrain the COF-COM-offset and the initial state of Io, discussed in Sections 5.3.1 and 5.3.2, respectively.

5.3.1. Constraining the COF-COM-Offset

The influence of variations in the true-to-formal-error ratio on the quality of our previous covariance analysis (see Section 5.2) as a function of the number of observations is shown in Figure 7. Again, we have performed a Monte-Carlo analysis for 100 different combinations of epochs that have been selected using the previously outlined hybrid algorithm.

In general, we expect 'interference' with the formal errors of the offset between COF and COM as soon as the artificially increasing *a priori* errors approach or exceed the estimated values of the formal uncertainties in the offset (for the latter, see Figure 6) - the estimation of the discrepancy between the COF and COM spills into that of the initial state, with the estimator no longer being able to entirely discern between the two effects. The *a priori* covariance matrix is not able to constrain the estimation of the initial state of Io to a point where the solution becomes sensitive to the COM-COF-offset. Hence, space-based astrometric observations begin to improve the overall orbit determination at the expense of accuracy within the formal errors of the COF-COM-offset, leading to distinct trends in the two in-plane (radial and along-track) and the out-of-plane (normal) directions.

In-plane direction: For the quality of the offset's radial solution, we observe that an increase in the true-to-formal-error ratio has no influence, with no row-wise change being observable in Figure 7. Since the average propagated *a priori* errors of Io (1.5 metres) are several orders of magnitude lower than the expected estimated formal errors of the COF-COM-offset (ranging from almost 3,000 to 150 metres), even - potentially unrealistically - high true-to-formal-error ratios will not lead to any interference. In contrast, the along-track component is significantly affected by changes in the true-to-formal-error ratio. We find column-wise 'uncertainty-plateaus' (this trend is especially pronounced for true-to-formal-error ratios of 13 and 21, and limited to regions with lower numbers of observations for higher ratios). Interference with the *a priori* covariance matrix causes an increase of the baseline solution towards which the obtainable formal uncertainties converge (see Section 5.2). While this baseline is originally driven by the maximum number of feasible epochs it is now a function of the scaled, averaged propagated *a priori* along-track error of Io.

Out-of-plane direction: For the normal component - in relative terms - the effect due to greater true-to-formal-error ratios becomes less pronounced for increasing numbers of observations. If only a small amount of images is being taken, scaling of the average propagated along-normal error (387 metres) begins to slightly interfere with the COF-COM-offset's estimated uncertainties. This can already be observed for ratios between three and five. While we cannot discern the emergence of any vertical 'uncertainty-plateaus', in stark contrast to the along-track direction, similar - but row-wise - behaviour is visible propagating towards a true-to-formal-error ratio of unity. Hence, while compared to the along-track direction any effects tend to occur for lower true-to-formal-error ratios, they are less clear-cut and exhibit a significantly lower gradient as a function of increasing ratio. Finally, for more than 320 observations, any influence of the true-to-formal-error ratio is reasonably negligible, exhibiting great resemblance with the radial demeanour.

Yet, if we recall the respective levels of average propagated *a priori* errors associated with the along-track and normal direction - 137 and 387 metres - the above-presented results differ from the intuitively thought demeanour. In particular, higher formal *a priori* errors are expected to lead to improve the overall orbit determination at greater expenses of accuracy within the formal errors of the COF-COM-offset). As previously outlined in Section 5.1.2, the out-of-plane offset between Io's COF and COM is almost always perfectly (i.e. uncorrelated from the remaining two directions) observable during the Jovian orbital phase of JUICE. Thus, given a sufficiently high number of observations, their information content is dense enough to simultaneously constrain the normal position of Io and the associated component of the COF-COM-offset.

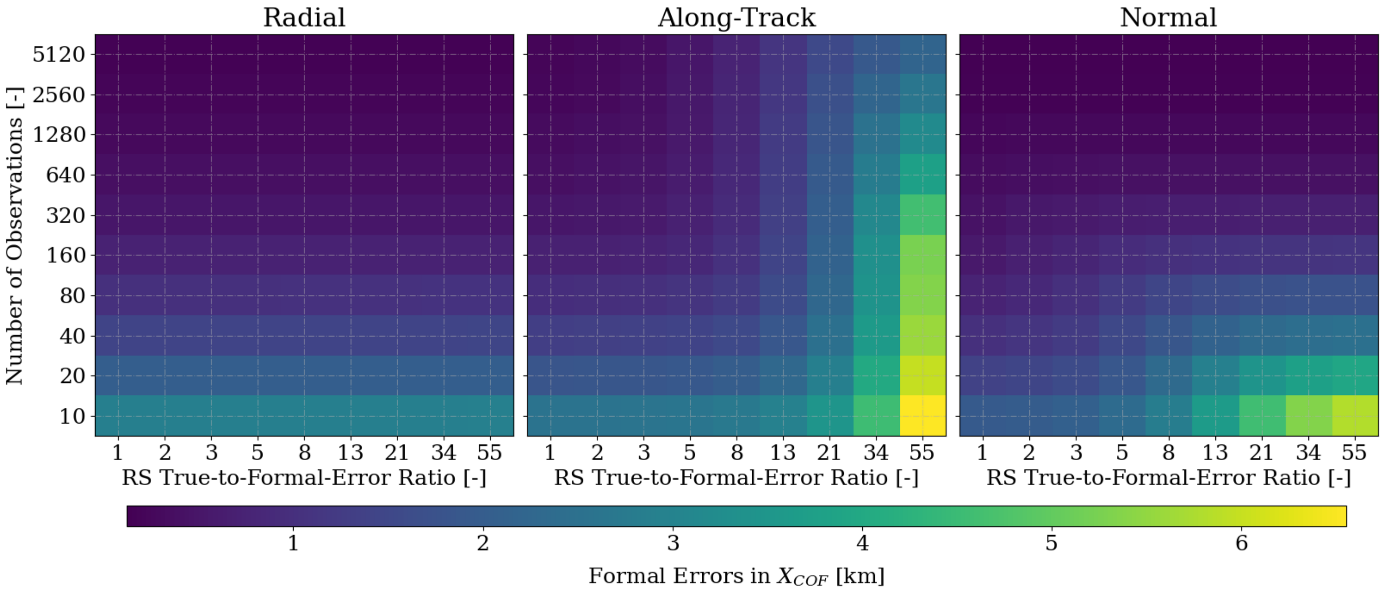

Fig. 7. Formal errors in the estimation of Io's COF-COM-offset as a function of the radio science (RS) true-to-formal-error ratio used as *a priori* information and the number of simulated observations. Each data point represents the average value of 100 distinct covariance analyses.

In contrast, given the difficult observation geometry, the along-track component is the most intricate observable direction. Thus, as has already been outlined in Section 5.1, observations of Io's along-track position are not only significantly correlated with the along-track component of the COF-COM-offset, but also with the offset's radial component. The radial position's correlations, on the other hand, are greatly reduced by the firmly constrained *a priori* state of Io. This behaviour is further underlined by the behaviour of the correlation matrices for different combinations of numbers of observations and radio science true-to-formal-error ratios shown in Figure 8. In particular, the increasing correlations between the along-track position of Io and the two in-plane directions of the COF-COM-offset as well as the inter-correlations of the latter underline the above-stated caveats. Finally, any observed constant along-track offset could be induced by both the COF-COM-offset and errors in the orbital solution - a constant normal offset can only be explained by a COF-COM-offset since errors in the out-of-plane direction (i.e. inclination) lead to periodic changes. Hence, even for substantial numbers of observations, it is not entirely possible to constrain both the position of Io and the along-track contribution to its COF-COM-offset to their prior levels. On a final note, while the three subplots in Figure 7 visually exhibit highly distinct behaviour, they are nevertheless subject to the same overall trend - even though they highlight entirely different parts hereof. In a hypothetical thought experiment, if we take the above-discussed distinct levels of *a priori* constraints, as well as the strong correlations within the orbital plane into account, the behaviours of all three subplots could be seen as *de facto* stackable - from the along-track direction at the bottom via the normal component to the radial contribution at the top. Hence, significantly more observations would be necessary to constrain the offset in along-track direction as well as the normal or even the radial contributions.

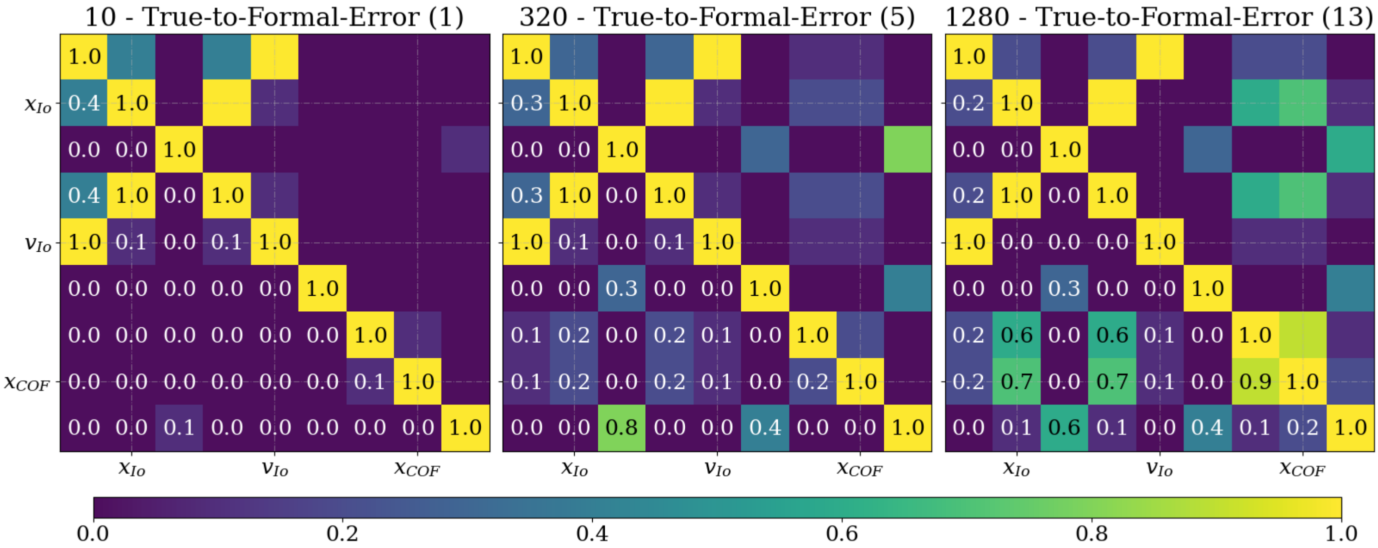

Fig. 8. Correlations between the Io's COF-COM-offset and its initial state expressed in a body-fixed RSW-frame for 10, 320, and 1280 observations and radio science true-to-formal-error ratios of 1, 5, and 13. Correlations have been averaged for 100 different combinations of epochs.

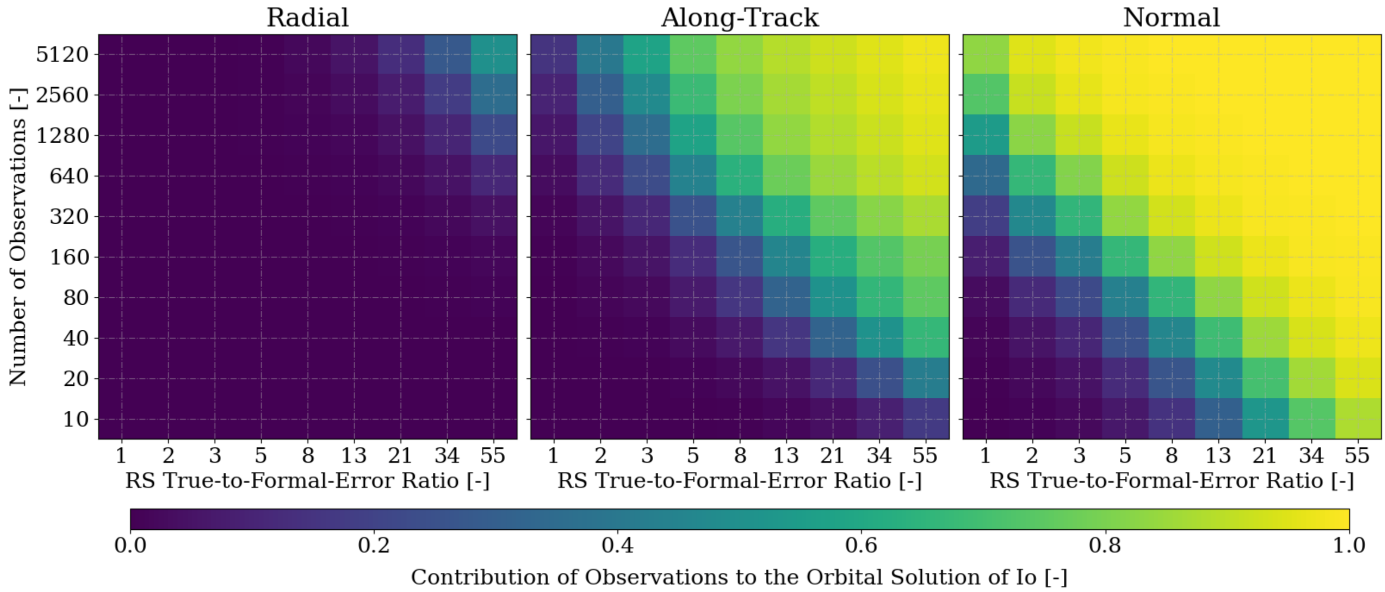

Fig. 9. Contribution of the optical space-based astrometric observations to the estimation of the initial state of Io as a function of the true-to-formal-error ratio of the radio science (RS) solution serving as *a priori* information and the number of simulated observations. Results are provided in radial (R), along-track (S), and normal (W) directions. Each data point represents the average value of 100 distinct covariance analyses.

5.3.2. Constraining the Initial State of Io

In an ideal world, the orbit of Io is primarily constrained by the radio science solution, while the COF-COM-offset will be constrained by optical observations. However, given an expected significant radio science true-to-formal-error ratio, space-based astrometry has to simultaneously constrain the initial state of Io and its COF-COM-offset. To determine the estimator's ability to simultaneously constrain both sets of parameters, we have to analyse the contribution of the simulated astrometric observations to Io's orbital solution. To this end, Figure 9 highlights the average c_q value (see Eq. 19) of Io's position as a function of the radio science true-to-formal-error ratio and the number of observations. Having been obtained simultaneously with the results presented in Figure 7, each square again represents the average value of the same 100 different combinations of epochs.

Unlike the above-described visually distinct behaviours of the COF-COM-offset's formal error in the in-plane and out-of-plane directions, changes in the averaged c_q values in Figure 9 exhibit a common - though distinctly pronounced - trend in all three directions. While the bottom-left corner exhibits a value of approximately nought for c_q - indicating no contribution of the observations to the orbital solution of Io - increasing the true-to-formal-error ratios and numbers of observations leads to a growth of the average c_q value towards the top-right corner of each subplot. This demeanour is indicative of the fact that the contribution of the observations becomes predominant and significantly helps to improve the orbital solution of Io, which is not constrained by the *a priori* information anymore.

Given the significantly lower radial uncertainty of the radio science solution, a reasonable contribution of the observations to the estimation of the initial radial state of Io is only discernible for unrealistically high true-to-formal-error ratios paired with high numbers of observations. Owing to the coarser *a priori* uncertainties in along-track and normal direction, and their above-described different levels of observability, considerable contributions of the observations to the orbit are visible in the along-track and especially the normal component. If we assume a total of approximately 1280 images being taken of Io - based on Cassini's average moon-wise number of observations (Tajeddine et al. 2015), see Section 5.2 - we visualise the evolutions of the formal uncertainties of the state of Io during the Jovian orbital phase of JUICE for two realistic true-to-formal-error ratios (8 and 13) in Figure 10. In particular, while the radial position is perfectly constrained by the scaled radio science solution - indicated by the dashed line - and the along-track state exhibits slight improvements between approximately 400 and 800 metres for two true-to-formal-error ratios, respectively, space-based astrometry constrains the out-of-plane direction to an average uncertainty of about 350 metres - comparable to the accuracy of Io's radio science solution for a true-to-formal-error ratio of unity. Overall, the behaviour shown in Figures 9 and 10 is thus perfectly in line with the above-outlined conclusions (see Section 5.3.1).

It has to be stressed that these results are most likely sketching a too-optimistic scenario since none of the remaining Galilean moons have been propagated alongside Io. In general, their respective radio science solutions will exhibit much lower formal uncertainties. In particular, this holds for Europa and Ganymede, both strongly coupled with the dynamics of Io via the Laplace resonance. Thus, by constraining the dynamics of the remaining moons, the radio science solution might prove to be more influential on constraining the state of Io than presented in Figure 9. Potentially this could thus lead to an earlier and steeper degradation of the COF-COM-offset's formal errors as a function of the true-to-formal-error ratio of the radio science solution, alongside a slower conversion with increasing numbers of observations in Figure 7. In turn, the contribution of the observations to Io's orbital solution would be further pushed towards the top-right corner of Figure 9, yielding a less constrained initial state of Io. Nevertheless, note that while the effect on the state of Io due to the Laplace resonance is only indirect - moderately correlated with the initial state of Io (Fayolle et al. 2023) - higher true-to-formal-error ratios of Io's radio science position have a direct effect. Overall, even without directly taking any orbital uncertainties of the remaining moons into account, our analysis of the extent to which space-based astrometry could constrain the state of Io is still reasonably indicative.

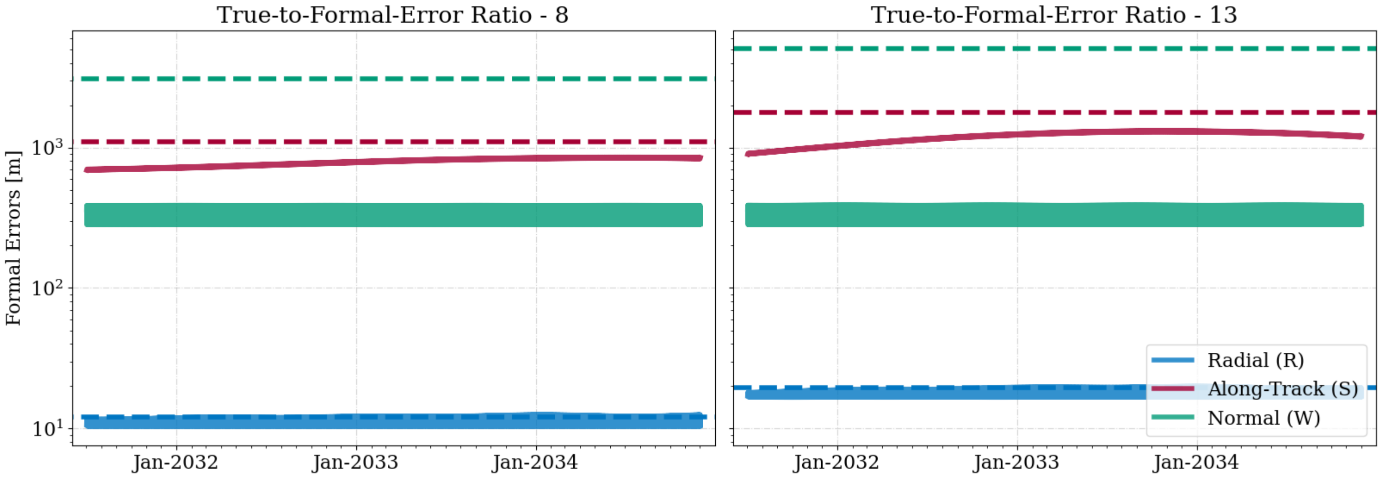

Fig. 10. Evolution of the formal uncertainties of the orbital solution of Io using a total number of 1280 simulated observations by the NavCam of JUICE. Dashed lines indicate the average radio science *a priori* constraints by Fayolle et al. (2023) scaled by the true-to-formal-error ratio.

6. Discussion

Understanding of tidal dissipation provides key insights into the thermo-orbital evolution of planetary systems, and the formation of the entire Solar System. For Jupiter, in order to detect secular signatures of tidal mechanisms, improved orbital solutions of the Galilean satellites - in particular of Io - are crucial. Thus, since optical space-based astrometry is pivotal to stabilise and potentially constrain the inversion of the state of Io, within this section, we discuss how such observations might either be used to validate the indirectly obtained radio science solution or directly contribute to the ephemeris of Io. Subsequently, we analyse any potential insights into Io's structure that one might draw based on the offset between the COF and COM. Finally, we briefly outline how space-based observations of stellar occultations of Io might possibly supplement optical astrometry.

6.1. Validation and Contribution to the Orbital Solution

Given the low expected formal uncertainties obtained by the radio science solution used as *a priori* information to constrain the estimation of the state of Io (see Section 4.3), the overall science return of optical space-based astrometry as stabilising contribution to the orbital solution is at stake. Assuming a moderate number of observations (no more than approximately 200 images) as well as a reasonable true-to-formal-error ratio no larger than five to eight - in essence, all combinations resulting in the lower left, dark purple parts in all three subplots in Figure 9 - we have shown that the orbital solution will be entirely dominated by the radio science solution.

On the one hand, even if we assume a negligible contribution to the overall orbital solution, we might instead exploit the information contained in optical space-based astrometry to validate the quality of the radio science solution. Owing to the indirect determination of Io's orbit from radiometric tracking data, a validation hereof is particularly critical. To this end, if the propagated - much tighter - error bound of the radio science solution laid within the much looser bounds of the individual optical observations, we could validate the radio science solution. Assuming the validity of the orbital solution, the absence of a significant offset between the centre-of-figure and centre-of-mass of Io directly leads to the just outlined congruence between the two different error bounds. Yet, the presence of a non-zero offset between the centre-of-figure and the centre-of-mass could skew the optical error bounds such that the propagated radio science uncertainties only partially match them. If this partial mismatch were to be explained by periodic behaviour due to an unaccounted COF-COM-offset, the radio science solution could still be validated.

On the other hand, even without perfect knowledge of the offset between the centre-of-figure and centre-of-mass of Io, optical space-based astrometry could contribute to the improvement of the orbital solution. By introducing a non-unity true-to-formal-error ratio, we artificially increase the error bound associated with the radio science solution while that of the optical observations remains untouched. Hence, assuming a reasonably coarse radio science solution - with a true-to-formal-error ratio no smaller than about five to eight - parts of the propagated error are scaled such that they lie outside of the astrometric error bounds. By definition, any non-intersecting parts of the errors are deemed unrealistic. In essence, realise that this is a highly simplified description of the underlying idea of orbit estimation - any improvements of the orbital solution thus come at the expense of the radio science solution being not as valid as originally thought. Nonetheless, we want to stress that this partial mismatch of the error bounds is different to the one outlined in the context of validation of the radio science solution - in particular, their respective effects due to decreasing true-to-formal-error ratios in the radio science solution are entirely contrary.

Visually, we can discern any non-negligible contributions of optical space-based observations to the overall orbital solution of Io by their increasingly yellowish shading in Figure 9, thus towards the top-right corner of each subplot. Assuming a total number of approximately 1280 observations - based on the average number of observations taken per moon by Cassini (Tajeddine et al. 2015), see Section 5.2 - minimum radio science true-to-formal-error ratios of approximately 3-5 and 1-2 for the along-track and normal direction, respectively, have been found in order for optical astrometry to have a reasonable contribution to the ephemeris estimation. However, as previously outlined, no significant improvements have been found for the radial position. Overall, given an anticipated true-to-formal-error ratio for Io between 3 and 10 (see Section 4.2), we hence expect significant contributions to the out-of-plane - and to a slightly lesser extent to the along-track - direction of Io's ephemeris while the radial position remains constrained by the *a priori* constraint.

On a final note, it has to be stressed that a quantitative definition of the cut-off values for which the contribution of the optical space-based astrometric observations to the orbital solution of Io is deemed negligible is subject to several parameters and thus far from clear-cut. First, the centre-of-figure, unlike the centre-of-mass, is conceptually merely vaguely defined, leading to a distinct - yet not quantifiable - noise floor. Second, as already briefly touched upon (see Section 5.3.2), by constraining the dynamics of the remaining moons via a concatenated estimation, the radio science solution might prove to be more influential on constraining the state of Io. In particular, due to the Laplace resonance being aligned with the orbital plane, any effects hereof will mainly affect the in-plane position of Io while the out-of-plane component remains largely untouched. Third, inaccuracies in the outlined analytic simulation of image-reduction (see Section 3.1) will be a further source of influence, with lower accuracies leading to higher uncertainties - and thus lower levels of contribution - in all three directions. Finally, the overall quality of the *a priori* information used to constrain the estimation of the COF-COM-offset directly propagates into the level of space-based astrometry's contribution to the estimated state of Io. Thus, as a result of tighter *a priori* constraints due to global inversion strategies - enabling estimation using radio-tracking data of JUICE and Europa Clipper alongside more than a century of ground-based astrometry (Fayolle et al. 2023) - the orbital solution of Io will benefit less form space-based astrometric observations.

6.2. Constraining the Interior Structure of Io

As evidenced by the values that have been found for its low-degree gravity field coefficients (see Table 1), Io is thought to be in hydrostatic equilibrium (Anderson et al. 2001). This conclusion is further underlined by the high level of correspondence between its observed and theoretical shape (assuming hydrostatic equilibrium), indicating a stable, balanced shape (Thomas et al. 1998). Thus, obtainable moments of inertia further suggest a differentiated interior structure with distinct layers - an iron core, a mantle, and a silicate crust (Van Hoolst et al. 2020). While it is commonly argued that the core of Io is molten (*e.g.* Khurana et al. 2011; Schubert et al. 2004), its radius (with estimates ranging from 650 to 950 km) and the mass fraction (respectively between 10 and 20 per cent of the total mass) hereof strongly depend on the exact - unknown - composition (Steinke 2021). Finally, given the observability of various mountains, the presence of a sufficiently strong lithosphere of varying thickness is assumed (Steinke et al. 2020).

So far, while no indications contradicting the presumed differentiated internal structure of Io have been observed, the state of Io's mantle remains highly questioned. In particular, the sublayer structure and their respective thermal states are subjects of debate, with conflicting views on the mantle's melt fraction. Studies about heat convection and diffusion within the mantle suggest a melt fraction of approximately 20 per cent (Steinke et al. 2020), which is backed by the expected range of 20 to 30 per cent indicated by the eruption temperature of Io's volcanoes (Keszthelyi et al. 2007). However, Khurana et al. (2011) have argued for the presence of even more significant melt fractions or even the potential existence of a global magma ocean due to the magnetic field as measured by the Galileo probe, with high melt fraction again having been repudiated by observations of Io's aurora (Roth et al. 2017).

Circling back to the briefly touched link between Io's interior and its tidal properties, hosting the bulk of tidal heat production, the mantle layer of Io strongly influences the interior and orbital dynamics (Steinke 2021), yet its exact structure and composition are not fully understood. To this end, estimations of the offset between the centre-of-figure and centre-of-mass yield an additional constraint on both the structure and composition of Io's mantle layer, crucial for further narrowing down the list of available interior models. In particular, we have to distinguish between effects due to two distinct cases - first, the estimated offset differs significantly from zero, or second, no or an almost negligible offset is assumed to be present.

Any significant COF-COM-offset arises from an asymmetric distribution of density or material (as strongly pronounced external topographic features), with internal heterogeneities being highly dominant given the mass-ratio between the crust and the mantle layer. Hence, potentially hinting at the presence of anomalies in a homogeneous, symmetric density distribution due to solidified silicate, increasing offsets could be an indication of a decreasing melt fraction in the mantle. However, by turning this argument around, any offset could also hint at the existence of an irregular pattern of regions with a higher melt fraction and temperature than surrounding areas as a result of irregular heat transfer through the mantle layer. Thus, significant offsets between the COF and COM generally suggest a more complex, asymmetric, and less homogeneous internal structure.

Given that significant variations in the conductive crust indicate changes in the crustal thickness of the order of several kilometres (Van Hoolst et al. 2020; Steinke et al. 2020), such variations would indeed lead to a certain, yet not overly significant 'baseline' offset (i.e. smaller than the above-assumed one, but still estimable). Assuming an otherwise symmetric distribution of density over the mantle layer, the estimation of no or an almost negligible offset would thus hint at either differences in the mineral composition - hence density - of the crust or isostatic compensation[5] of density anomalies within the mantle by the topography or vice versa. The absence of any significant offset between the COF and COM is a necessary condition for the presence of a high melt fraction of silicates within Io's mantle. However, we have to stress that this is by no means a sufficient condition in favour of a greater percentage of magma within Io. In general, a small offset is thus an indication of a more homogeneous, symmetric internal structure and composition of Io.

6.3. Influence of Orbital Librations and Tidal Deformation

As outlined in Section 2, the orbital motion of Io is not entirely Keplerian and subject to slight temporal variations, leading to changes in the gravitational torque of Jupiter and hence additional librations and tidal deformations (Lainey et al. 2006; Van Hoolst et al. 2020). Generally, these librations are modelled as superpositioned contribution to the rotational state of Io - contradicting our initial, simplified assumption of a synchronous rotation. Mathematically, librations directly influence Eq. 21 - the observation equation for the constant COF-COM-offset vector - by altering the body-fixed-to-inertial rotation matrix. Tidal deformations, on the other hand, induce a - so far unaccounted, see Section 3.1 - discrepancy between the model used to fit the limb to its imaged counterpart and the actual shape of Io.

As a result of the Laplace resonance, Van Hoolst et al. (2020) indicate that long-term librations of Io are strongly connected with the orbital interactions via the other moons - with variations

---

[5] Isostatic compensation refers to the mechanism by which any excess mass above a specific reference level (such as Earth's sea level) is countered by a deficiency in density within the underlying layers, ultimately achieving a state of isostatic equilibrium (Kearey et al. 2009).

in eccentricity, semi-major axis, or orbital inclination merely having a secondary influence. Yet, we have to stress that the libration amplitude is directly linked to the rigidity and viscosity of Io's interior structure and composition. In particular, since the tidal deformation of the crust of Io increases with decreasing crustal rigidity, conservation of energy dictates the libration amplitude to decrease (Jara-Orué & Vermeersen 2014; Van Hoolst et al. 2013). Thus, exact measurements of the libration amplitude could provide direct insights into the internal structure of Io. Finally, non-accounted librations could potentially negatively spill into the estimation of the discrepancy between the centre-of-figure and centre-of-mass, as well as the optical space-based orbital solution of Io.

Given an expected order of magnitude for the libration amplitude of approximately one kilometre - with exact values strongly depending on the internal structure and melt fraction of Io (Van Hoolst et al. 2020) - currently achievable uncertainties of space-based imaging are too coarse to properly constrain the libration of Io. Still, space-based stellar occultation observed using the ultraviolet spectrograph (UVS) of either JUICE or Europa Clipper could obtain accuracies up to a few metres. While this high level of accuracy of UVS observations might be problematic in the context of ephemeris estimation - since the best available dynamical and shape models of Io are not yet at metre level - significant advancements in the topography of Io (Abrahams et al. 2021) as well as our understanding of librations and tidal deformations within Io are to be expected. Besides giving direct insights into the structure of Io's interior, explicitly accounting for long-term orbital librations could allow a reprocessing of the optical space-based imaging data - potentially yielding further improvements of the orbital solution and estimation of the centre-of-figure and centre-of-mass offset of Io.

7. Conclusions

Improving the orbital solutions of the Galilean satellites to advance our understanding of the underlying mechanisms of tidal dissipation is crucial to providing key insights into their thermo-orbital evolution and the formation of the entire Solar System. However, while the radio-tracking data of JUICE and Europa Clipper will constrain the dynamics of Europa, Ganymede, and Callisto to an unprecedented level of accuracy, the lack of flybys around Io results in an imbalanced data set. Merging the radio science data with optical space-based astrometry of Io could thus stabilise and potentially improve the orbital solution. Obtaining a measure for the COF-COM-offset moreover yields a new constraint on Io's interior structure and composition. Exploiting the tidal coupling between Io and Jupiter, this could lead to further improvements in our understanding of tidal interaction.

By explicitly accounting for any potential discrepancy between the imaged centre-of-figure and propagated centre-of-mass, we have mitigated the offset's effect on the ephemeris estimation of Io when using optical space-based astrometric observations. Given the high level of expected accuracy in Io's radio science solution (Fayolle et al. 2023; Magnanini et al. 2023), we have discussed the extent to which astrometric imaging is able to either validate radio science of Io or constrain its state. The formal errors in the COF-COM-offset and the state of Io have been estimated from simulated optical space-based astrometry as a function of the expected number of observations and the radio science true-to-formal-error ratio (see Section 5.3).

It has been shown that the absolute uncertainties and the relative observation geometries of a sequence of space-based astrometric images are pivotal drivers in constraining the offset in the COF and COM of Io. Hence, an analytic expression to model the relative uncertainties associated with simulated observations has been implemented (see Section 3.1) and optimised based on data provided by Tajeddine et al. (2015). Instead of resorting to their expected average number of background stars, realistically accounting for the momentaneous number of visible stars in the NavCam's field-of-view would complement the currently used model for the camera's pointing uncertainty.

Given the three-dimensional nature of the problem, variations within the relative observation geometry are crucial to the estimation of the COF-COM-offset (Pasewaldt et al. 2012). We have found that - owing to the largely equatorial alignment of JUICE with respect to Io - the observation of the along-track position of Io is obstructed by the brightness of Jupiter (see Section 5.1.2). Hence, in order to maximise the scientific return of optical space-based astrometry, observations taken during the high-inclination phase of JUICE are indispensable. Adopting a simultaneously uncertainty- and geometry-driven hybrid algorithm for the selection of epochs at which observations are to be simulated has thus been found to be essential (see Section 5.2).

To restrain our estimation framework to the formal uncertainty of the radio science solution, we have constrained our covariance analysis to the averaged propagated formal errors of Io that would arise from the rigorous implementation of the radiometric tracking set-up of JUICE and Europa Clipper using suitable *a priori* information (see Section 4.3). For the discrepancy between the centre-of-figure and the centre-of-mass, a hypothetical best-case scenario with formal uncertainties of approximately 200 metres and about 100 metres in the in-plane and out-of-plane directions, respectively, has subsequently been found. Translating Cassini's average number of 1310 observations per moon to Io, we have obtained realistically attainable formal uncertainties of no more than 300 metres. Nonetheless, using the proposed algorithm, our estimation has been limited to the state of Io. While the *a priori* covariance matrix accounts for the (static) uncertainties in the states of the other moons, we merely mimic any influence that the propagated uncertainties in these states could have on the covariance of Io and vice versa. Thus, expanding the dynamical model to all four Galilean moons would be an insightful complement.

Finally, using a rigorous Monte Carlo analysis, the expected contribution of optical observations to the estimation of the offset between the centre-of-figure and the centre-of-mass, as well as the ephemeris of Io as a function of the expected quality of the radio science solution, has been assessed (see Sections 5.3). While the estimation of the COF-COM-offset's radial contribution has been found to be independent hereof, both the along-track and out-of-plane direction are distinctly affected by the radio science true-to-formal-error ratio. Within their ability to either validate radio science or constrain the orbital solution of Io, all three components have been found to exhibit comparable demeanour - the state of Io is progressively less constrained by the radio science *a priori* information and the contribution of the optical observations becomes predominant. While the exact value for the radio science true-to-formal-error ratio of the state of Io is not known, a total of 1280 observations of Io translate to minimum ratios for astrometry to have an observable impact of approximately 3-5 and 1-2 for the in-plane and out-of-plane directions, respectively. Overall, it is thus highly likely that space-based astrometry contributes to the orbital solution of Io. Nonetheless, the potential of optical space-based imaging to constrain the orbital solution of Io should be further investigated - for instance by concurrently inverting space-based astrometric observations of both JUICE and Europa Clipper.

References

Abrahams, J. N. H., Nimmo, F., Becker, T. M., et al. 2021, Earth and Space Science, 8

Anderson, J. D., Jacobson, R. A., Lau, E. L., Moore, W. B., & Schubert, G. 2001, Journal of Geophysical Research: Planets, 106, 32963

Antreasian, P. G., Bordi, J. J., Criddle, K. E., et al. 2005, Cassini orbit determination performance during the first eight orbits of the Saturn satellite tour

Arlot, J.-E. 2019, Journal of Astronomical History and Heritage, 22, 78

Boutonnet, A., Varga, G., Rocchi, A., Martens, W., & Mackenzie, R. 2018, JUICE - Jupiter Icy moons Explorer Consolidated Report on Mission Analysis (CReMA), Report, ESA-ESOC (European Space Operations Centre)

Cappuccio, P., Notaro, V., di Ruscio, A., et al. 2020, IEEE Transactions on Aerospace and Electronic Systems, 56, 4984

Cooper, N. J., Murray, C., Porco, C., & Spitale, J. 2006, Icarus, 181, 223

Cooper, N. J., Murray, C. D., Lainey, V., et al. 2014, A&A, 572

Davies, A. G. 2007, Volcanism on Io: A Comparison with Earth (Cambridge: Cambridge University Press)

Davies, A. G., Perry, J. E., Williams, D. A., & Nelson, D. M. 2023, Nat. Astron.

Dias-Oliveira, A., Vieira-Martins, R., Assafin, M., et al. 2013, Monthly Notices of the Royal Astronomical Society, 432, 225

Dirkx, D., Fayolle, M., Garrett, G., et al. 2022, in Europlanet Science Congress 2022, Granada, Spain, 18–23 Sep 2022, EPSC2022-253

Dirkx, D., Gurvits, L. I., Lainey, V., et al. 2017, Planet. Space Sci., 147, 14

Dirkx, D., Lainey, V., Gurvits, L. I., & Visser, P. N. A. M. 2016, Planet. Space Sci., 134, 82

Dirkx, D., Mooij, E., & Root, B. 2019, Astrophysics and Space Science, 364, 37

Fayolle, M., Dirkx, D., Lainey, V., Gurvits, L. I., & Visser, P. N. A. M. 2022, Planet. Space Sci., 219

Fayolle, M., Dirkx, D., Visser, P. N. A. M., & Lainey, V. 2021, A&A, 652

Fayolle, M., Magnanini, A., Lainey, V., et al. 2023, A&A, 677, A42

Floberhagen, R. 2001, Thesis, Technische Universiteit Delft

Folkner, W. M., Iess, L., Anderson, J. D., et al. 2017, Geophysical Research Letters, 44, 4694

French, R. G., McGhee, C. A., Frey, M., et al. 2006, Publications of the Astronomical Society of the Pacific, 118, 246

Fuller, J., Luan, J., & Quataert, E. 2016, Monthly Notices of the Royal Astronomical Society, 458, 3867

Gaia Collaboration. 2018, A&A, 616, A1

Gaia Collaboration. 2021, A&A, 649, A1

Gomes-Júnior, A. R., Morgado, B. E., Benedetti-Rossi, G., et al. 2022, Monthly Notices of the Royal Astronomical Society, 511, 1167

Grasset, O., Dougherty, M. K., Coustenis, A., et al. 2013, Planet. Space Sci., 78

Greenberg, R. 2010, Reports on Progress in Physics, 73

Heller, R., Marleau, G. D., & Pudritz, R. E. 2015, A&A, 579

Iess, L., Folkner, W. M., Durante, D., et al. 2018, Nature, 555, 220

Jacobson, R. A., Haw, R. J., McElrath, T. P., & Antreasian, P. G. 2000, J. Astronaut. Sci., 48, 495

Jara-Orué, H. M. & Vermeersen, B. L. 2014, Icarus, 229, 31

Jones, D. L., Folkner, W. M., Jacobson, R. A., et al. 2015, The Astronomical Journal, 149

Jones, D. L., Folkner, W. M., Jacobson, R. A., et al. 2020, The Astronomical Journal, 159, 72

Kaula, W. M. 1964, Reviews of Geophysics, 2

Kearey, P., Klepeis, K. A., & Vine, F. J. 2009, Global Tectonics, 3rd edn. (Oxford: Wiley-Blackwell)

Keszthelyi, L., Jaeger, W., Milazzo, M., et al. 2007, Icarus, 192, 491

Khurana, K. K., Jia, X., Kivelson, M. G., et al. 2011, Science, 332, 1186

Konopliv, A. S., Asmar, S. W., Folkner, W. M., et al. 2011, Icarus, 211, 401–428

Lainey, V., Arlot, J.-E., Karatekin, Ö., & Van Hoolst, T. 2009, Nature, 459, 957

Lainey, V., Casajus, L. G., Fuller, J., et al. 2020, Nature Astronomy, 4, 1053

Lainey, V., Dehant, V., & Pätzold, M. 2007, A&A, 465, 1075

Lainey, V., Duriez, L., & Vienne, A. 2004, A&A, 420, 1171

Lainey, V., Duriez, L., & Vienne, A. 2006, A&A, 456, 783

Lainey, V., Jacobson, R. A., Tajeddine, R., et al. 2017, Icarus, 281, 286

Lainey, V., Özgür Karatekin, Desmars, J., et al. 2012, AJ, 752, 14

Lari, G. 2018, Celestial Mechanics and Dynamical Astronomy, 130

Liebe, C. C. 1995, IEEE Aerospace and Electronic Systems Magazine, 10, 10

Lieske, J. H. 1998, A&A Supplement Series, 129, 205–217

Magnanini, A., Zannoni, M., Gomez Casajus, L., et al. 2023, A&A - Review

Melman, F. 2018, Thesis, Technical University Delft

Mignard, F. 1979, The Moon and the Planets, 20, 301

Milani, A. & Gronchi, G. 2010, Theory of Orbit Determination (Cambridge: Cambridge University Press)

Montenbruck, O. & Gill, E. 2000, Satellite Orbits: Models, Methods, and Applications (Berlin, Heidelberg: Springer Berlin Heidelberg)

Moore, W., Schubert, G., Anderson, J., & Spencer, J. 2007, in Io After Galileo: A New View Of Jupiter's Volcanic Moon, ed. R. M. C. Lopes & J. R. Spencer (Berlin: Springer Berlin), 89–108

Murray, C. D. & Dermott, S. F. 1999, Solar System dynamics (Cambridge: Cambridge University Press)

Oberst, J., Matz, K. D., Roatsch, T., et al. 2006, A&A, 447, 1145

Pasewaldt, A., Oberst, J., Willner, K., et al. 2012, A&A, 545

Peale, S. J., Cassen, P., & Reynolds, R. T. 1979, Science, 203, 892–894

Roth, L., Saur, J., Retherford, K. D., et al. 2017, Journal of Geophysical Research: Space Physics, 122, 1903

Samuel, H., Lognonné, P., Panning, M., & Lainey, V. 2019, Nature, 569, 523

Schubert, G., Anderson, J. D., Spohn, T., & McKinnon, W. B. 2004, in Jupiter. The Planet, Satellites and Magnetosphere, ed. F. Bagenal, T. E. Dowling, & W. B. McKinnon (Cambridge: Cambridge University Press), 281–306

Smith, D. E., Zuber, M. T., Neumann, G. A., & Lemoine, F. G. 1997, Journal of Geophysical Research: Planets, 102, 1591

Steinke, T. 2021, Thesis, Technische Universiteit Delft

Steinke, T., Hu, H., Höning, D., van der Wal, W., & Vermeersen, B. 2020, Icarus, 335, 113299

Tajeddine, R., Cooper, N. J., Lainey, V., Charnoz, S., & Murray, C. D. 2013, A&A, 551

Tajeddine, R., Lainey, V., Cooper, N. J., & Murray, C. D. 2015, A&A, 575

Thomas, P., Davies, M., Colvin, T., et al. 1998, Icarus, 135, 175

Van Hoolst, T., Baland, R.-M., & Trinh, A. 2013, Icarus, 226, 299

Van Hoolst, T., Baland, R.-M., Trinh, A., Yseboodt, M., & Nimmo, F. 2020, Journal of Geophysical Research: Planets, 125

Vienne, A. 2008, Planet. Space Sci., 56, 1797

Willner, K., Oberst, J., Wählisch, M., et al. 2008, A&A, 488, 361

Zuber, M. T., Smith, D. E., Lemoine, F. G., & Neumann, G. A. 1994, Science, 266, 1839

Appendix A: Optical Space-Based Astrometry - Validation of the Centre-of-Figure Uncertainty for JUICE

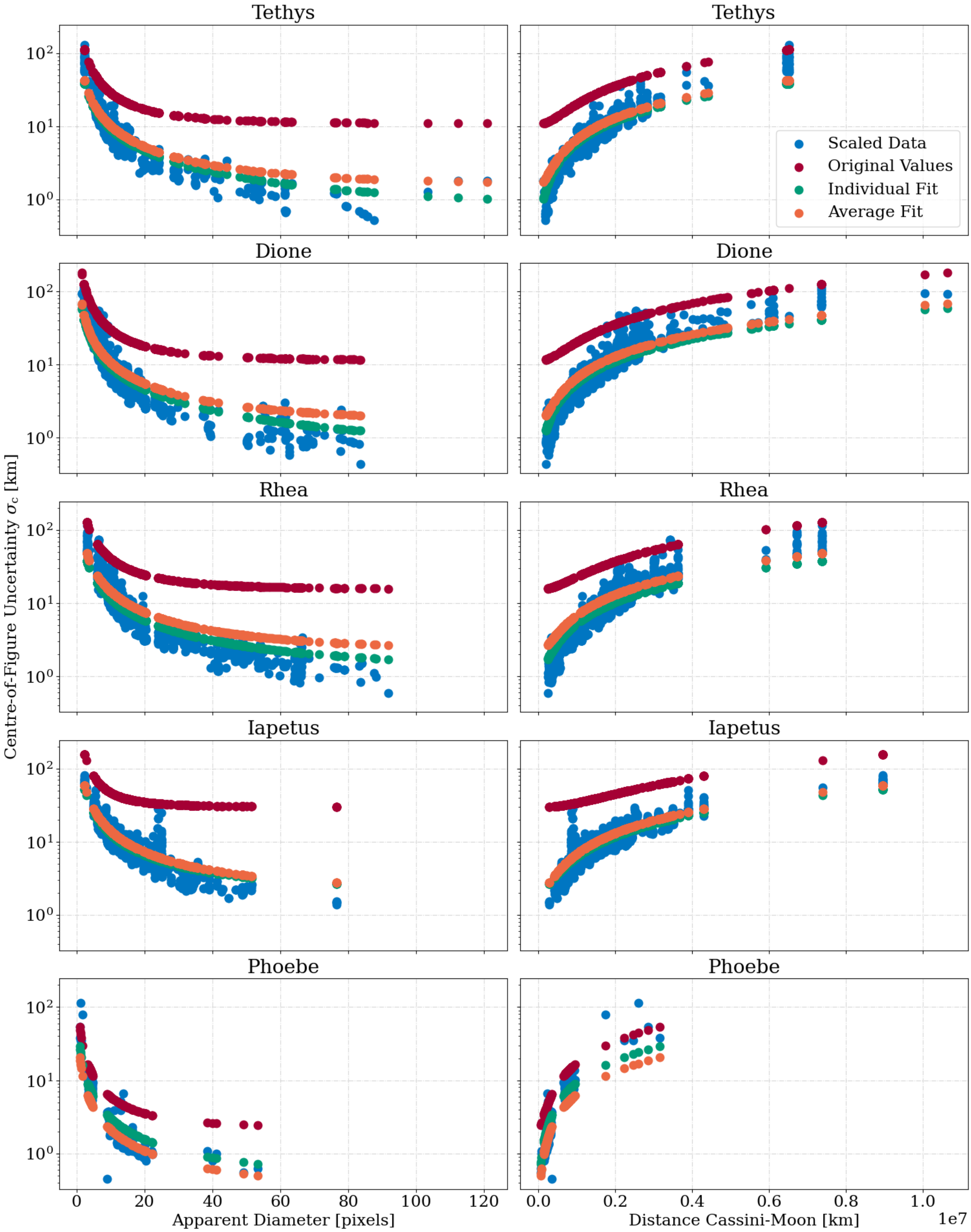

Fig. A.1. Moon-wise behaviour of both the fitted analytical model by Antreasian et al. (2005) to the data provided by Tajeddine et al. (2015) for Cassini as a function of either the apparent diameter or the distance to the respective moon. Data has been scaled to mimic the he results that would have been expected when using a NavCam-like camera instead of Cassini's NAC. Stated centre-of-figure uncertainties are thus not representative for the original accuracy achieved by Cassini, yet they demonstrate how the reduction of NavCam-like images would have performed.

While highly adapted reduction techniques have been developed to obtain estimates of the accuracies of space-based images (Tajeddine et al. 2013, 2015), they fall short of the description of simulated uncertainties. Thus, an analytical expression hereof is indispensable in the context of conceptual studies. However, with the only available analytical model by Antreasian et al. (2005) merely poorly agreeing with the data obtained by Cassini, we have fitted the two variable model parameters to imaging data provided by Tajeddine et al. (2015) for five Saturnian moons - Tethys, Dione, Rhea, Iapetus, and Phoebe. Figure A.1 visualises the moon-wise results of this non-linear least-squares fit.

In general, as can be inferred from Figure A.1, the (fitted) analytical model by Antreasian et al. (2005) is well adapted, yet the original values for the model parameters yield notable discrepancies with Cassini's data. For the four larger moons - Tethys, Dione, Rhea, and Iapetus, in particular - we obtain high levels of agreement between the fitted curves and the imaging data. Phoebe, on the other hand, has a highly irregular shape that naturally complexifies the limb-fitting process. Hence, since Cassini has furthermore taken significantly fewer images of this satellite, Phoebe's individual fit should be treated with caution. Still, to obtain a slightly conservative parameter estimate - i.e. favouring slight overestimation of the formal uncertainty over too optimistic accuracies - the slightly higher fitted parameters for Phoebe have explicitly been included in the calculation of the averaged parameters subsequently being treated as final fit. Overall, we have found values of 0.095 pixels and 0.0014 for the weighting factor $\sigma_{\min}$ and scaling factor C, respectively.

Given that the apparent diameter of the imaged moon in pixels - of which the analytical expression is a function - is a somewhat elusive quantity, we have also visualised the demeanour of the centre-of-figure uncertainty as a function of the distance between the spacecraft and the respective moon. For observations of Io by JUICE, we are especially interested in relative distances ranging from 0.04e7 to 0.25e7 kilometres, the minimum and maximum proximity for which optical space-based astrometry has been found to be possible. From Figure A.1, we can conclude that the obtained fit within this regime is of particular quality, highlighting the high degree of the underlying potential of our fitted analytical expression.

On a final note, the artificially introduced scaling factor of $FOV_{NavCam}/FOV_{NAC} = 4/0.35$ to mimic the results that would have been expected when using a NavCam-like camera instead of Cassini's NAC needs to be addressed. Realise that both the obtainable centre-of-figure uncertainty as well as the respective satellite's apparent diameter have to be scaled accordingly. Intuitively, while the linear scaling of the (by definition one-dimensional) apparent diameter is rather straightforward, one would expect the centre-of-figure uncertainty of the two-dimensional limb to be scaled by a scaling factor taking both dimensions of the field-of-view into account. However, owing to the limb-fitting process being performed iteratively for all horizontally interconnected lines of pixels across the satellite (for more details, see Tajeddine et al. (2013)), the respective pixel-wise information content similarly has to be scaled linearly using the above-stated scaling factor.

3

Conclusions and Recommendations

Building upon the results and discussion thereof presented in the journal paper (see Chapter 2), within this chapter we provide detailed conclusions by evaluating how the individual research questions have been answered and contributed to the overall research objective of the thesis. Furthermore, we thoroughly delineate and discuss recommendations for potential future work.

3.1. Conclusions

Within this section, we will address the underlying research objective of this work outlined in Section 1.1. Providing an answer to all research questions will place this work in the context of the overall research objective that laid the foundation of this work.

RSQ1: How can we simulate optical space-based astrometric observations whilst simultaneously deriving realistic associated uncertainties?
From a simulation point-of-view, optical astrometry can be simulated as angular observations of the right ascension and declination of a natural satellite with respect to the spacecraft. In essence, this is comparable to the much more frequently used simulation of angular measurements of ground-based Very Long Baseline Interferometry (VLBI) observations. However, a dedicated schedule and observational constraints - e.g. ensuring no images to be taken with a direct view of the Sun or too close to the limb of Jupiter - have to be implemented upfront as a general feasibility check of all individual epochs over the total simulation period. To model the error induced by an optical reduction pipeline and derive realistic uncertainties, an analytic expression to compute the relative uncertainties associated with simulated observations has been implemented and optimised. To this end, we have fitted the variable parameters within our analytical expression to the optical (already reduced) data obtained by Cassini using a least-squares algorithm. However, given that the geometrical specifications of the corresponding field-of-views significantly differ between the imaging subsystems of Cassini and JUICE, we had to introduce a scaling factor to mimic the results that would have been expected when using a NavCam-like camera instead of Cassini's imaging subsystem.

RSQ2: How can we account for the COF-COM-offset of Io within our dynamical model?
In a body-fixed frame, the offset between the centre-of-figure and centre-of-mass of a celestial body can be expressed as a constant vector. Hence, mathematically perfectly decoupled from any assumed

shape model, a straightforward dynamical representation should exist. Usually, the offset between the COF and COM enters the equations of motion via the gravity field. However, we have shown that a consistent implementation in the dynamical model can be somewhat cumbersome. In particular, using the relation between a celestial body's COM with respect to its COF and its unnormalised gravity field coefficients of degree and order one has proven to be highly erroneous. While this approach yields a consistent description of the gravitational dynamics, the COF is now treated as the overall origin of the body-fixed frame. Yet, we have found that by shifting the frame origin from the COM to the COF, non-zero degree and order one gravity field coefficients introduce an artificial discrepancy to the implemented analytical tidal model developed with respect to a body's COM. For Io, changing the origin of the underlying frame indirectly leads to variations in the energy dissipated into its orbit via the tidal interaction with Jupiter resulting in large mismatches in the orbital position over time.

Thus, instead of altering the properties of the dynamical model, we have introduced a difference between the models used within the simulation of observations and state propagation. While entering the observation equation, the COF does not influence the dynamical equations of motion. In other words, optical astrometry data has explicitly been fed into the covariance analyses as unintended observations of the centre-of-figure. In essence, this process explicitly accounts for the offset between the observed COF and propagated COM, unlike the implicit estimation framework typically applied to space-based astrometric observations. Since the offset between the COF and COM has so far not been explicitly estimated, per definition, optical observations are always taken with respect to the COF. Yet, any optical observables are implicitly treated as being taken with respect to the imaged body's COM, thus introducing a discrepancy between the observation and estimation models. However, by explicitly estimating the offset between the COF and COM alongside the initial state of Io, we eliminate the model discrepancy, thus potentially improving the overall orbital solution.

RSQ3: To what extent will different relative observation geometries and uncertainties of optical observations influence the formal errors of the estimated COF-COM-offset?
We have found that absolute (metric) uncertainties and relative observation geometries space-based astrometric images are crucial to constrain the estimation of the discrepancy between the centre-of-figure and centre-of-mass of Io. Unsurprisingly, decreasing uncertainties have been identified as the primary driver of the offset's associated formal errors - with potential improvements due to ten suitably selected observations ranging from 43 per cent in the out-of-plane component up to 50 per cent in the in-plane directions, respectively. Yet, we have further highlighted that variations in the relative observation geometry are a pivotal secondary criterion. Owing to the largely equatorial alignment of JUICE with respect to Jupiter and Io, the observation of the in-plane component of the offset is generally obstructed by the brightness of the former prominently looming in the NavCam's field-of-view, while the normal direction is well covered. The high-inclination phase of JUICE is the only exception that breaks this pattern owing to a significant out-of-plane orientation.

Since the image-acquisition planning for the NavCam instrument is yet not firmly chosen, potential recommendations for an effective observation scheme are of particular importance. Hence, in order to maximise the scientific return of optical space-based astrometry, we have highlighted that - besides an overall low absolute uncertainty - imaging during the high-inclination phase of JUICE is indispensable to decorrelate the different contributions to the in-plane offset. Using the proposed uncertainty and geometry-driven hybrid algorithm for the selection of epochs at which observations are to be simulated, already low numbers of astrometric images (80 observations) yield low formal errors in the determination of the COF-COM-offset of about 1 kilometre. In particular, this is about one-quarter of the number of observations required to obtain comparable uncertainties when randomly selecting epochs. Furthermore, by translating Cassini's average number of 1310 observations per moon to Io, we have obtained realistically attainable formal uncertainties of no more than 300 metres. Finally, we have shown that an optimised observation geometry yields a more circularised uncertainty ellipse, with errors in radial and along-track direction mutually approaching, even though the three-dimensional ellipse, however, will never be spherical but remains oblate in the out-of-plane component.

RSQ4: What is the influence of the radio science quality on the space-based astrometry's ability to constrain the estimation of the COF-COM-offset and contribute to the orbital solution?
Owing to the tracking data of JUICE and Europa Clipper predominately obtained during the orbital phase around Ganymede and the many flybys of Europa, respectively, the indirect estimation of the state of Io is going to lead to a substantial true-to-formal-error ratio of its radio science solution. In general, an increasing radio science true-to-formal-error ratio has led to interference with the formal errors of the offset between the centre-of-figure and centre-of-mass. We have highlighted that the estimation of the COF-COM-offset spills into that of the initial state, with the estimator no longer being able to discern between the two effects. Since the *a priori* radio science solution has been found to no longer be able to exclusively constrain the estimation of the initial state of Io, space-based astrometric observations begin to improve the overall orbit determination at the expense of accuracy within the formal errors of the estimated COF-COM-offset. Owing to the low uncertainty level of the radio science solution in the radial direction (1.5 metres), the associated component of the COF-COM-offset has never been affected. However, for moderate numbers of observations, the scaled radio science normal (387 metres) and along-track errors (137 metres) begin to interfere with the estimated uncertainties of the COF-COM-offset (between approximately 3,000 to 150 metres for 10 and 5120 observations, respectively). We have shown that this trend already occurs for true-to-formal-error ratios between 3 and 5 for the out-of-plane direction, and 8 and 13 in the along-track component.

The extent to which optical space-based observations could potentially contribute to the estimation of the state of Io has been found to significantly depend on the true-to-formal-error ratio of the radio science solution. Assuming a reasonable true-to-formal-error ratio as well as a moderate number of observations, we have shown that the orbital solution will be entirely dominated by radio science. While we have underlined that optical observations could still be valuable to validate the radio science solution, we have further highlighted that optical space-based astrometry might indeed contribute to improvements in the orbital solution, given a sufficiently high true-to-formal-error within the radio science solution. Assuming a total number of approximately 1280 observations - based on the average moon-wise number of observations taken by Cassini - minimum radio science true-to-formal-error ratios of approximately 3-5 and 1-2 for the along-track and normal direction, respectively, have been found in order for optical astrometry to have a reasonable contribution to the ephemeris estimation. However, owing to the associated firm radio science constraint, no significant improvements have been found for the radial position.

RSQ5: Which insights can a measure of the discrepancy between the centre-of-figure and centre-of-mass of Io give us on the interior structure of Io?
Any significant COF-COM-offset arises from an asymmetric distribution of density or material (as especially pronounced external topographic features), with internal heterogeneities highly dominant given the mass ratio between the crust and the mantle layer. Hence, potentially hinting at the presence of anomalies in a homogeneous, symmetric density distribution due to solidified silicate, increasing offsets could be an indication of a decreasing melt fraction in the mantle. However, by turning this argument around, any offset could also hint at the existence of an irregular pattern of regions with a higher melt fraction and temperature than surrounding areas as a result of irregular heat transfer through the mantle layer. Thus, significant offsets between the COF and COM generally suggest a more complex, asymmetric, and less homogeneous internal structure.

Given that significant variations in the conductive crust indicate changes in the crustal thickness of the order of several kilometres, such variations would indeed lead to a certain, yet not overly significant 'baseline' offset (i.e. smaller than the above-assumed one, but still estimable). Assuming an otherwise symmetric distribution of density over the mantle layer, the estimation of no or an almost negligible offset would thus hint at either differences in the mineral composition - hence density - of the crust or isostatic compensation (a special form of Archimedes' principle) of density anomalies within the mantle by the topography or vice versa. The absence of any significant offset between the COF and COM is a necessary condition for the presence of a high melt fraction of silicates within Io's mantle. However, we have to stress that this is by no means a sufficient condition in favour of a greater percentage of magma within Io. In general, a small offset is thus an indication of a more homogeneous, symmetric internal structure and composition of Io.

The goal of this thesis is to estimate and analyse the discrepancy between the centre-of-figure and centre-of-mass of Io, and subsequently determine the ability of optical space-based astrometric observations to contribute to the overall orbital solution.

Improving the orbital solutions of the Galilean satellites is crucial to providing key insights into their thermo-orbital evolution and the formation of the entire Solar System. To this end, to stabilise the imbalanced estimation of Io's radio science ephemeris solution, direct optical space-based astrometry by the imaging subsystem of JUICE has been suggested to constrain the dynamics of Io. Yet, with the inversion of orbital dynamics performed with respect to the centre-of-mass of natural satellites, optical space-based observations of the position of a body's centre-of-figure introduce a discrepancy between the observation and estimation model. Thus, explicitly accounting for the offset between the observed centre-of-figure and the propagated centre-of-mass during ephemeris estimation, however, mitigates the influence of the discrepancy on the orbital solution of Io when using optical space-based astrometric observations.

Within this work, we have shown that the absolute uncertainties and the relative observation geometries of a sequence of space-based astrometric images are pivotal drivers in constraining the offset in the COF and COM of Io. However, owing to the largely equatorial alignment of JUICE with respect to Io - the observation of the along-track position of Io has been found to be obstructed by the brightness of Jupiter. In order to maximise the scientific return of optical space-based astrometry, the benefit of observations taken during the high-inclination phase of JUICE has been highlighted. Hence, we have formulated recommendations for an appropriate adaptation of the observation schedule of the NavCam. If we assume a total of approximately 1280 images being taken of Io - based on Cassini's average moon-wise number of observations - realistically attainable formal uncertainties in the estimated COF-COM-offset of no more than 300 metres have been obtained. For astrometry to have a significant impact on the ephemeris estimation of Io, this has translated to a true-to-formal-error ratio of the *a priori* radio science solution of approximately 3-5 and 1-2 for the in-plane and out-of-plane directions, respectively. Overall, given an anticipated radio science quality for Io with ratios between three and ten, we have thus concluded a high likelihood of space-based astrometry contributing to the orbital solution.

3.2. Recommendations for Future Work

The results and conclusions presented in this thesis have already hinted at several interesting points that could be investigated in the future to further analyse the discrepancy between a celestial body's COF and COM. Within this section, these areas of further research shall be briefly addressed.

- This work has exclusively focused on the estimation of the centre-of-figure and centre-of-mass offset of Io. However, crucial information about the formation and evolution of the Jovian system as well as on the respective interior structure can be expected from the estimation of the COF-COM-offset in the remaining Galilean satellites. While observations by the laser and radar altimeter aboard JUICE and Europa Clipper will most likely well-constrain the discrepancies for Ganymede and Europa, respectively, any offset within Callisto remains unconsidered. Hence, as a preliminary study of the science return, the methodology developed within this thesis could be transferred to Callisto. Unlike Io, Callisto is not trapped in orbital resonance with any of the other moons - whilst potential minor improvements of Io's orbital solution might thus be cancelled by the Laplace resonance out over short time spans, Callisto's ephemeris is much more stable. On the other hand, since the data used to generate the control point network of Callisto would be a lot more diverse, this introduces a new source of complexity. Nonetheless, whilst this would further validate the results and conclusions drawn in this work, it would also underline the general applicability of the methodology to other satellites or planetary systems.

- So far, we have only taken optical space-based astrometric observation by JUICE into account. However, these could potentially be combined with observations of Io taken by the imaging subsystem of Europa Clipper. The presence of two missions in the same planetary system is unprecedented. Such a study could thus reveal potential observational synergies when combining the two data sets of space-based astrometry. In particular, the simultaneous observation of Io from two different points of view could be an interesting feature to investigate further.
- The contribution of the number of visible background stars to the pointing error and hence space-based astrometric uncertainty could simultaneously benefit from a deeper analysis. In particular, ways to implement the stars of the Galactic background and their respective brightness based on a Gaia star catalogue, as well as realistically modelling the light pollution around the edges of Io's limb should be further investigated. Even though we have shown that the contribution of the pointing error to the overall uncertainty is about one order of magnitude lower than the error within the limb-fitting process, this could nevertheless pave the way for a much more fine-grained and realistic representation of the uncertainty within optical observations and the selection of epochs.
- Furthermore, a concatenated analysis of the contribution of optical space-based observations to the orbital solution of Io combined with the estimation of the initial states of the remaining Galilean satellites - Europa, Ganymede, and Callisto - could be conducted. In essence, this would enable deeper insights into how propagated uncertainties of the other moons might influence the estimation of the offset between Io's centre-of-figure and centre-of-mass or how improvements in the ephemeris estimation might be absorbed within the initial states of the other moons. Investigation of this effect would be of particular interest for Europa and Ganymede, both strongly coupled with the dynamics of Io via the Laplace resonance.
- The critically delineated method to constrain the estimation of the orbital solution of Io to the expected level of Io's propagated formal errors using suitable *a priori* covariance matrices - and in particular all underlying, simplifying assumptions - should be thoroughly validated. So far, we have not taken any temporal variations - due to, for instance, a densely stacked succession of flybys - in the obtainable formal uncertainty of the radio science solution into account. Instead, *a priori* covariance matrices that mimic the averaged propagated formal errors have been computed. To this end, the radiometric tracking set-up of both JUICE and Europa Clipper should be rigorously implemented. Subsequently, comparing the results obtained using our *a priori* approach and those arising from such a concatenated state estimation could validate the extent to which the use of *a priori* constraints approximates the impact of the radio science solution. Further, realise that this validation should also be combined with the above-outlined recommendations, if applicable.

- Finally, no non-state parameters besides the offset between the centre-of-figure and centre-of-mass have been estimated. Still, we know that the orbital motion of Io is not entirely Keplerian and subject to slight temporal variations, leading to librations of Io's rotation. In general, these librations could be modelled as superpositioned contributions to the rotational model of Io. However, given the conceptual nature of this thesis, so far, this has been omitted. Yet, simulating and estimating librations of Io could prove to be a valuable addition to the analysis of the expected scientific return of optical space-based imaging. In particular, since non-accounted librations might potentially negatively affect the estimation of the offset between the centre-of-figure and centre-of-mass, as well as the optical space-based orbital solution of Io. Since the currently achievable uncertainties of space-based imaging are too coarse to properly constrain the librations of Io, space-based stellar occultations of the ultraviolet spectrograph (UVS) of either JUICE or Europa Clipper could be simulated. While the high level of accuracy of UVS observations might be problematic in the context of ephemeris-estimation - since the best available dynamical and shape models of Io are yet not at metre level - librations with an expected order of magnitude for the associated amplitude of approximately one kilometre could be neatly estimated. Potentially, this could allow us to simulate the scientific return of optical space-based imaging in case librations of Io are taken into account - yielding further improvements in the orbital solution and estimation of the centre-of-figure and centre-of-mass offset of Io.

A

Integrator and Propagator Selection

To propagate the orbits of the Galilean satellites, their respective equations of motion (as stipulated in Section 2.4 of the journal paper) have to be integrated over time. Owing to its finite time-step, numerical integration is an approximate representation of reality and thus a trade-off between numerical precision and computational effort has to be made. In general, two types of numerical errors constitute the achievable accuracy - we distinguish between the so-called rounding and truncation errors. While the latter builds up over integration time due to the above-outlined approximation of the solution, the former is a result of the computational limitation in the finite floating-point number representation. Given the complex nature of the dynamics of the Galilean satellites, small initial offsets due to erroneously integrated orbits might become reinforced by the Laplace resonance. Hence, the selection of a sufficiently accurate numerical integrator is crucial. On the other hand, the maximum achievable physical accuracy of the propagated orbit is limited by the level of uncertainty within the implemented dynamical model. With the integration of the orbit and the variational equations being the computational bottleneck of our estimation framework, using covariance analyses in the context of a rigorous Monte Carlo analysis poses a significant time-wise challenge, underlining the need for efficient numerical integration. Thus, a trade-off between the computational effort (i.e. the number of function evaluations) and the achievable numerical accuracy is crucial, with the individual steps hereof being presented in Section A.2, extending on a brief discussion on the selection of a benchmark solution in Section A.1. Finally, Section A.3 provides a concise explanation of our choice of propagator, differing in the way they express and solve the equations of motion.

A.1. Benchmark Solution

To analyse the integration error associated with different numerical integrators and settings, we have to benchmark the integrated equations against a reference solution. To this end, the selection of a suitable benchmark integrator is required. Owing to their predictable behaviour as a function of increasing time-steps, usually, high-order fixed-step integrators are chosen to establish a benchmark solution. Thus, we will use a Runge-Kutta 8th-order integrator and subsequently optimise its time-step to minimise the numerical integration error of the reference solution. To get a reasonable estimate of the achievable integration error ϵ as a function of the time-step, we will compare two integrations with different numerical accuracies (i.e. two time-steps, Δt_1 and $\Delta t_2 > \Delta t_1$) with one another. Further denoting the 'true' orbital and integrated solution by $y(t)$ and $\bar{y}(t)$, respectively, we find the following estimate for the benchmark integration error:

$$\begin{aligned} y(t) &= \bar{y}^{(1)}(t) + \epsilon\left(\Delta t_1\right), \\ y(t) &= \bar{y}^{(2)}(t) + \epsilon\left(\Delta t_2\right), \\ \bar{y}^{(1)}(t) - \bar{y}^{(2)}(t) &= \epsilon\left(\Delta t_2\right) - \epsilon\left(\Delta t_1\right) \approx \epsilon\left(\Delta t_2\right). \end{aligned} \tag{A.1}$$

Yet, we have to ensure that the benchmark integrator's time-step has to be sufficiently small to blur the line between numerical truncation and rounding errors. Nevertheless, we have to prevent the accumulation of random numerical noise due to an excessive number of integration steps (i.e. a minuscule time-step). To this end, Figure A.1 visualises the demeanour of the numerical error of a Runge-Kutta 8th-order integrator as a function of the time-step. Thus, for the reference solution to lie within the transition regime from truncation to rounding errors, we choose a benchmark time-step of 15.0 minutes.

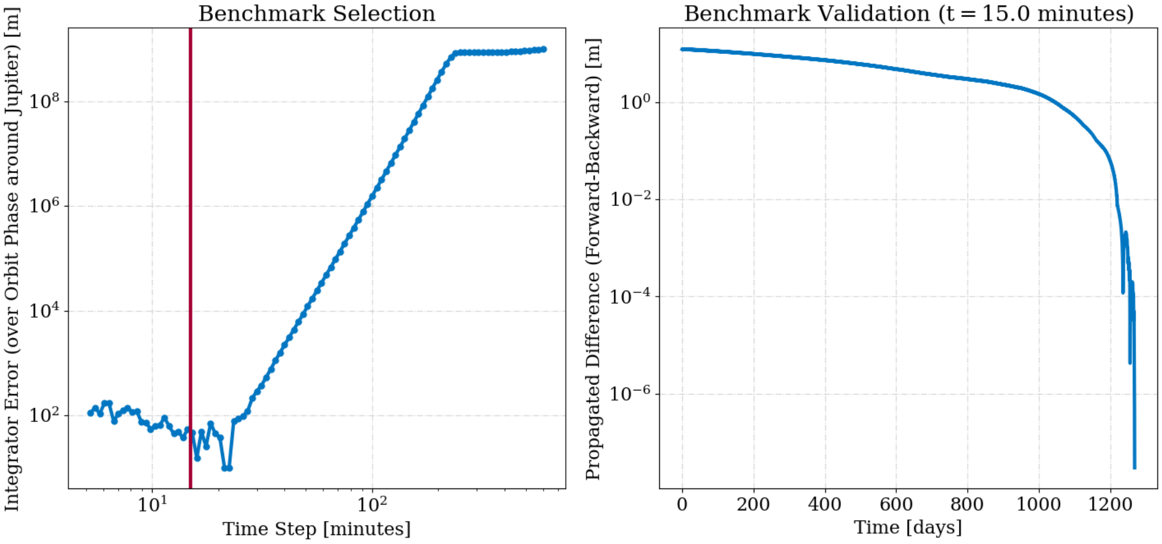

Figure A.1: Benchmark selection (left) and validation (right). Numerical integration errors for the selection have been computed with respect to the 5.0 minutes solution using an 8th-order Runge-Kutta integrator over the duration of the orbital phase of JUICE around Jupiter. The chosen integrator's time-step is indicated by the vertical red line and validated via a forward-backward propagation of the state of Io, using the state of the forward propagation as the new initial state of the backward propagation.

To validate our choice of benchmark integrator, we perform a forward-backwards propagation of the state of Io, using the state of the forward propagation as the new initial state of the subsequent backward propagation. By design, with the exception of numerical integration errors, the initial and final state of the forward and backward propagation, respectively, should be identical. To this end, Figure A.1 illustrates the differences between the forward and backward propagation. With a final mismatch of a mere 10 metres, the accuracy and suitability of the chosen benchmark integrator have been validated.

A.2. Comparison of Integrators

A wide variety of different integrators is implemented in the TU Delft Astrodynamics Toolbox (tudat), in particular Euler, Runge-Kutta, Runge-Kutta-Fehlberg, Dormand-Prince, Adams-Bashforth-Moulton, and Bulirsch-Stoer integration routines. Without going into too much detail, both the Euler and Bulirsch-Stoer integrators have been eliminated upfront - while the former is prone to lead to very high integration errors due to the underlying first-order linearisation, the sparse integration outputs of the latter - typically used in combination with extensively long integration times - are not suitable in the context of simulating optical space-based astrometric observations and orbit determination. By design, the chosen bounds for the absolute and relative tolerances for variable time-step integrators are rather independent of the orbital problem at hand. In contrast, the selected time-steps have to be critically evaluated to match the problem at hand, since for instance, much lower step-sizes are required to capture the fast-changing dynamics during re-entry flights than the propagation of the much more uniform orbital dynamics of celestial bodies. Since Lainey et al. (2009) propagated the dynamics of the Jovian system over more than a century, their time-step of approximately two hours has been chosen as the upper limit, given our much shorter propagation period. The following integrators and settings have been implemented:

- Runge-Kutta (RK)
  - RK4: time-step = [30.0; 40.0; 50.0; 60.0; 90.0; 120.0] min
  - RK5: time-step = [30.0; 40.0; 50.0; 60.0; 90.0; 120.0] min
  - RK6: time-step = [30.0; 40.0; 50.0; 60.0; 90.0; 120.0] min
  - RK7: time-step = [30.0; 40.0; 50.0; 60.0; 90.0; 120.0] min
  - RK8: time-step = [30.0; 40.0; 50.0; 60.0; 90.0; 120.0] min
- Runge-Kutta-Fehlberg (RKF)
  - RKF4(5): absolute and relative tolerances = [10^{-14}; 10^{-12}; 10^{-10}; 10^{-8}; 10^{-6}; 10^{-4}]
  - RKF5(6): absolute and relative tolerances = [10^{-14}; 10^{-12}; 10^{-10}; 10^{-8}; 10^{-6}; 10^{-4}]
  - RKF7(8): absolute and relative tolerances = [10^{-14}; 10^{-12}; 10^{-10}; 10^{-8}; 10^{-6}; 10^{-4}]
- Dormand-Prince (DP) - DP8(7): abs. and rel. tolerances = [10^{-14}; 10^{-12}; 10^{-10}; 10^{-8}; 10^{-6}; 10^{-4}]
- Adams-Bashforth-Moulton (ABM)
  - variable order and time-step: abs. and rel. tolerances = [10^{-13}; 10^{-11}; 10^{-9}; 10^{-7}; 10^{-5}; 10^{-3}]
  - 6th order, variable time-step: abs. and rel. tolerances = [10^{-13}; 10^{-11}; 10^{-9}; 10^{-7}; 10^{-5}; 10^{-3}]
  - 8th order, variable time-step: abs. and rel. tolerances = [10^{-13}; 10^{-11}; 10^{-9}; 10^{-7}; 10^{-5}; 10^{-3}]
  - 10th order, variable time-step: abs. and rel. tolerances = [10^{-13}; 10^{-11}; 10^{-9}; 10^{-7}; 10^{-5}; 10^{-3}]
  - variable order, fixed time-step = [30.0; 40.0; 50.0; 60.0; 90.0; 120.0] min

By grouping the integrators into their respective classes - fixed-step (RK), multi-step (RKF and DP), as well as variable- and fixed-step multi-stage (ABM), Figure A.2 effectively highlights the different deviations from our chosen benchmark solution (i.e. the integrator error) corresponding to the above-outlined integrators and settings. In general, a smaller time-step or stricter tolerance will lead to an increase in accuracy at the expense of more function evaluations. It becomes evident that within the three distinct integrator classes, the RK8, DP8(7), and variable order and fixed-step ABM integrator yield the best results in terms of the achievable integration error and required function evaluations. While the DP8(7) varies its respective time-step as a function of the absolute and relative tolerances (e.g. larger time-steps outside of the lunar conjunctions within the Laplace resonance), both the RK8 and ABM integrator provide an equally-spaced integration output over time. Yet, while the demeanour in terms of number of function evaluations and integration errors of the RK8 and DP8(7) are highly uniform and exhibit approximately linear behaviour (when visualised in a log-log plot), the behaviour of the ABM integrator is much more erratic and less predictable (see Figure A.2). In particular, this is underlined by the significant decrease in integration error for reductions in the time-step from 50 to 40 minutes and can be explained by the multi-stage nature of the integrator. Moreover, even though the fixed-step ABM integrator exhibits the lowest number of function evaluations to integrate Io's equations of

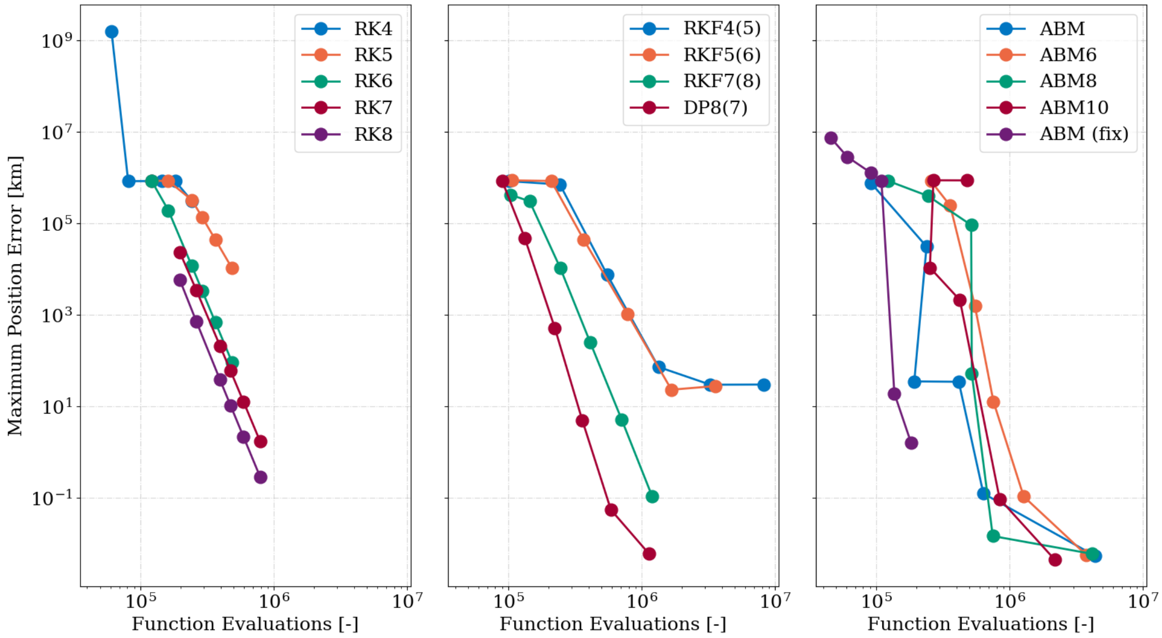

Figure A.2: Integrator error for different integrators and settings as a function of the number of function evaluations. The above-stated time-steps and tolerances as well as a Cowell propagator have been used.

motion, it is simultaneously limited to a minimum achievable accuracy of approximately one kilometre. In comparison with the much lower integration errors of the RK8 and DP8(7) methods, this renders the fixed-step ABM integrator unsuitable for our problem at hand. Finally, we want to shift our focus to the change in slope in the demeanour of the DP8(7) integrator for reductions of the absolute and relative tolerance from 10^{-12} to 10^{-14}. This kink is indicative of a transition from pure truncation to numerical rounding error - thus progressively unpredictable integration behaviour for slight various in the integration time or initial state (as will be performed to ensure the consistency of the dynamical model, see Appendix B). Hence, even though slightly more function evaluations will be required to reach a similar numerical accuracy compared to the DP8(7) integrator, a fixed-step-size RK8 integrator with a time-step of 30 minutes has thus been finally selected as the best trade-off between the maximum position error (approximately 100 metres) and the required number of function evaluations (slightly less than 10^6), while at the same time providing a perfectly uniform integration output.

A.3. Selection of Propagators

Finally, a choice of propagator has to be made. So far, all integrations have been performed using the default Cowell propagator. To this end, tudat allows a choice of the following implemented propagators:

- Cowell,
- Encke,
- Gauss - Keplerian Elements,
- Gauss - Modified Equinoctial Elements (MEE),
- Unified State Model (USM) - Quaternions,
- Unified State Model (USM) - Modified Rodrigues Parameters (MRP),
- Unified State Model (USM) - Exponential Map.

However, due to Euler's rotation theorem, some of these propagators exhibit one or more numerical singularities for certain values of the eccentricity and inclination of the orbit. For instance, propagating Keplerian elements is numerically singular in the case of perfectly circular ($e = 0$) or planar ($i = 0°$) orbits, while MEE also exhibits a singularity for zero inclination, effectively ruling out those propagators for the propagation of the Galilean satellites, since their orbits are too close to (some) of the known singularities. Moreover, due to the presence of the Laplace resonance, the three inner moons exhibit significant deviations from their initial Kepler orbits over long integration intervals, greatly reducing the effectiveness of the Encke formulation. Moreover, a preliminary analysis has shown that neither of the three USM propagators has led to significant improvements in terms of accuracy or computational efficiency when combined with the chosen RK8 integrator. Hence, since neither of the other propagators has been proven to be a significantly more accurate or robust option given the problem at hand, and Cowell's straightforward implementation, it has been kept as default propagator within this work.

B

Verification and Validation

Within this section of the appendix, we describe the individual steps that have been taken to verify and validate the dynamical and numerical models that have been implemented over the course of this work. In particular, we have used various modules of the TU Delft Astrodynamics Toolbox (tudat). Extensive use has been made of the orbit propagation and estimation features. Besides any readily implemented and validated functions, we have made use of multiprocessing in Python to enable the efficient computation of covariance matrices and have further expanded the tudat-toolbox by several numerical methods developed within the scope of this thesis, including the analytic determination of the uncertainty optical space-based astrometry and the associated observation schedule and constraints as presented in Sections 4.1 and 4.3 of the journal paper. First, however, the consistency of the dynamical model - as outlined in Section 2 of the journal paper - has been validated, with the individual steps hereof being presented in Section B.1, followed by the validation of optical observation constraints in Appendix B.2. Finally, in Appendix B.3, the extensively used estimation framework (i.e. underlying covariance analysis) is verified using a deterministic approach.

B.1. Consistency of the Dynamical Model

Owing to the complex dynamical interactions between the four Galilean satellites - in particular, the presence of the Laplace resonance between Io, Europa, and Ganymede - a correct and consistent implementation of the overall dynamical model is crucial for an accurate discussion of the results. To this end, we have fitted Io's initial position and velocity to the NOE-5-2021 ephemerides of the Galilean moons and compared its propagated state history to the ephemeris' reference state. Subsequently, the presence of the Laplace resonance between the propagated state of Io and the states of Europa and Ganymede (as taken from their respective SPICE kernels) has been validated based on the correct representation of the Laplace angle and the oscillation around its mean value. Finally, the agreement between the propagated state of Io and the trajectory of JUICE (similarly taken from its SPICE kernels) needs to be shown - this has been done by evaluating the differences in the distance between JUICE and both Io's propagated and reference trajectories, as well as the relative angles with the body-fixed axes of Io over the duration of the orbital phase around Jupiter.

B.1.1. Fit to the NOE-5-2021 ephemerides

To mitigate the influences of slight modelling mismatches between our delineated dynamical model (see Section 2 of the journal paper) and the one underlying the computation of the NOE-5-2021 ephemerides of the Galilean satellites provided by the Institut de Mécanique Céleste et de Calcul des Ephémérides (IMCCE), we fit the state of Io to (artificial) Cartesian state observations of its ephemeris. The positions and velocities of the three remaining moons are fixed to their ephemerides' states. By fitting the propagated state history of Io to its NOE ephemeris, we obtain a good (i.e. consistent with the ephemeris when propagated) estimate of the initial position and velocity. By design, any minor disagreements between the two dynamical models will spill into the optimised initial state of Io, minimising the overall state difference. These computations have been performed over a time span of 1,270 days - the duration of the orbital phase of JUICE around Jupiter - with a rate of one simulated observation every three hours. As initial epoch, we have hence chosen July 1st 2031, the day of the Jupiter Orbit Insertion (JOI) of JUICE. In particular, the difference in the orbital position of Io has been fit. Note that no weights have been assigned to the Cartesian position observables. A similar approach has been used by Lainey et al. (2007) to fit the initial states of the Martian moons to their respective ephemerides.

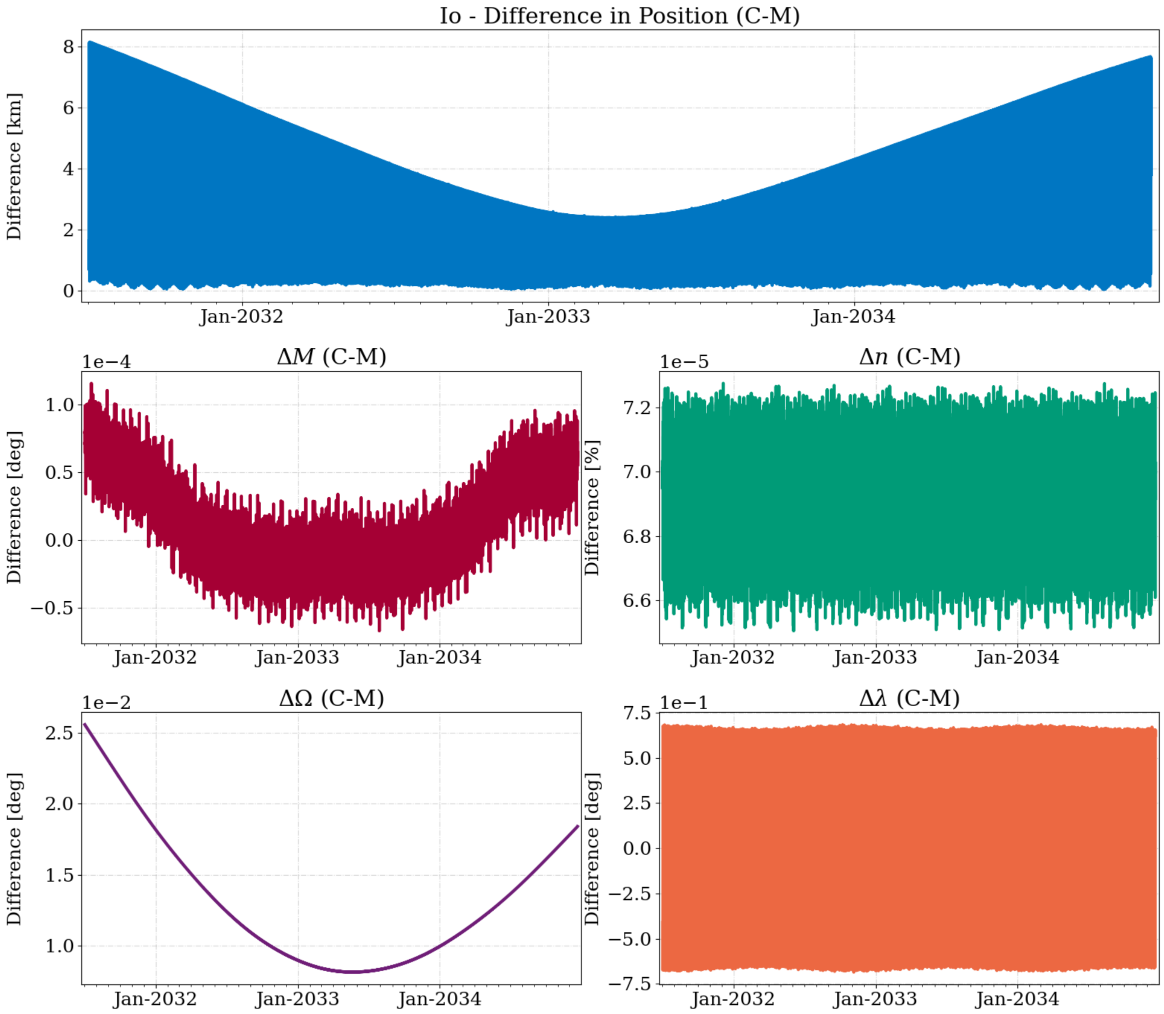

Figure B.1: Residuals between the propagated state of Io (C) and its NOE-5-2021 ephemeris (M) in the absolute difference in position (top) and selected orbital parameters - the mean anomaly ΔM, the orbital mean motion Δn, the right ascension of the ascending node $\Delta\Omega$, and the mean longitude $\Delta\lambda$. The relative difference in the orbital mean motion is given with respect to its reference state (obtained from the NOE-5-2021 ephemeris).

In Figure B.1, we show the residuals in the absolute position for Io after having applied the above-outlined estimation procedure. If not indicated otherwise, residuals have been evaluated by subtracting the modelled or reference values using the NOE ephemerides (M) from the computed values (C). Besides the difference in position, Figure B.1 furthermore illustrates deviations in the mean anomaly ΔM, the orbital mean motion Δn, the right ascension of the ascending node $\Delta\Omega$, and the mean longitude $\Delta\lambda$. All presented orbital parameters have been selected due to their relevance in the following calculation of the Laplace resonance (see Section B.1.2) between Io, Europa, and Ganymede.

We observe that the absolute difference in the orbital position does not exceed a few kilometres and exhibits symmetric demeanour - maximal deviations towards the temporal bounds of the estimation and a minimum centred at the mid-point. Overall, the difference in the position of Io as depicted in Figure B.1 indicates good agreement between the two underlying dynamical models. This preliminary conclusion is further underlined by the residuals within the remaining orbital parameters - in particular, the almost constant (relative) offset in the respective orbital mean motions are indicative of a consistent implementation of any secular dynamics with a period equal to or lower than the duration of the orbital phase of JUICE around Jupiter. Realise that the (minor) differences in the satellite's right ascension of the ascending node are a direct result of the slight variations in the Laplace resonance due to the difference in the satellites' position. Furthermore, the behaviour of the difference in the longitude of Io with respect to Jupiter exhibits approximately periodic behaviour, oscillating around a mean value of nought hinting at internal compensation of minor modelling mismatches, which is confirmed by the demeanour of the difference in the mean anomaly of Io. In essence, while any short-term periodic behaviour is oscillating around a superposed long-term curve - exhibiting a high level of shape-wise resemblance with that of the right ascension - the average difference is nonetheless equal to zero.

On a final note, it has to be stressed that the assumed modelling uncertainty of the NOE-5-2021 ephemeris itself is of the order of a few kilometres. Hence - assuming the Laplace resonance to be present in the dynamical model, which we will analyse in the following - the overall, good agreement is more than adequate for the simulation of observations and estimation of the offset between the centre-of-figure and centre-of-mass of Io.

B.1.2. Presence of the Laplace Resonance in the Dynamical Model

As already highlighted in our journal paper, the Jovian system and the Galilean satellites are distinctively shaped by the orbital resonance between Io, Europa, and Ganymede. In fact, the Laplace resonance is the superposition of two distinct resonances, a 1:2 commensurability between Europa and Io and a second 1:2 resonance between Ganymede and Europa. Given that no flybys are planned around Io, its radio science solution will mainly be determined indirectly via the dynamics of Europa (via the various flybys of Europa Clipper) and Ganymede (via the orbital phase of JUICE) - we have to validate the presence of the Laplace resonance in our dynamical model. In particular, the Laplace resonance is characterised by the so-called Laplace angle ϕ_L as a function of the momentaneous mean longitudes of the three inner Galilean satellites (Murray and Dermott, 1999):

$$\phi_L = \lambda_I - \lambda_E + \lambda_G = 180^\circ, \tag{B.1}$$

effectively assuming a static resonance. The Laplace angle, however, *de facto* slightly librates around a mean value of 180° with a period of 2059.622 days, essentially being the main effect of the Laplace resonance (Lainey et al., 2006), superpositioned by several short-term oscillations.

Furthermore, the two distinct commensurabilities can be described individually by their longitudes of conjunction θ_{ij}, with the first and second subscript denoting the particular resonance pair and argument of pericenter, respectively. Hence, the resonance between the two inner moons, Io and Europa, can be characterised by (*e.g.* Greenberg, 2010; Murray and Dermott, 1999):

$$\theta_{11} = \lambda_1 - 2\lambda_2 + \bar{\omega}_1 \approx 0^\circ, \tag{B.2a}$$

$$\theta_{12} = \lambda_1 - 2\lambda_2 + \bar{\omega}_2 \approx 180^\circ, \tag{B.2b}$$

again taking slight librations around a mean value - 0° or 180° - into account. For the commensurability between Europa and Ganymede, we find (*e.g.* Greenberg, 2010; Murray and Dermott, 1999):

$$\theta_{22} = \lambda_2 - 2\lambda_3 + \bar{\omega}_2 \approx 0^\circ, \tag{B.3a}$$

$$\theta_{23} = \lambda_2 - 2\lambda_3 + \bar{\omega}_3 = [0^\circ;\ 360^\circ], \tag{B.3b}$$

with θ_{23} periodically circulating through 360°. On a final note, we want to stress that the expression for the Laplace angle given in Eq. B.1 directly follows from the longitudes of conjunction involving Europa's argument of pericentre $\bar{\omega}_2$, implicitly linking the inner and outer resonance pair.

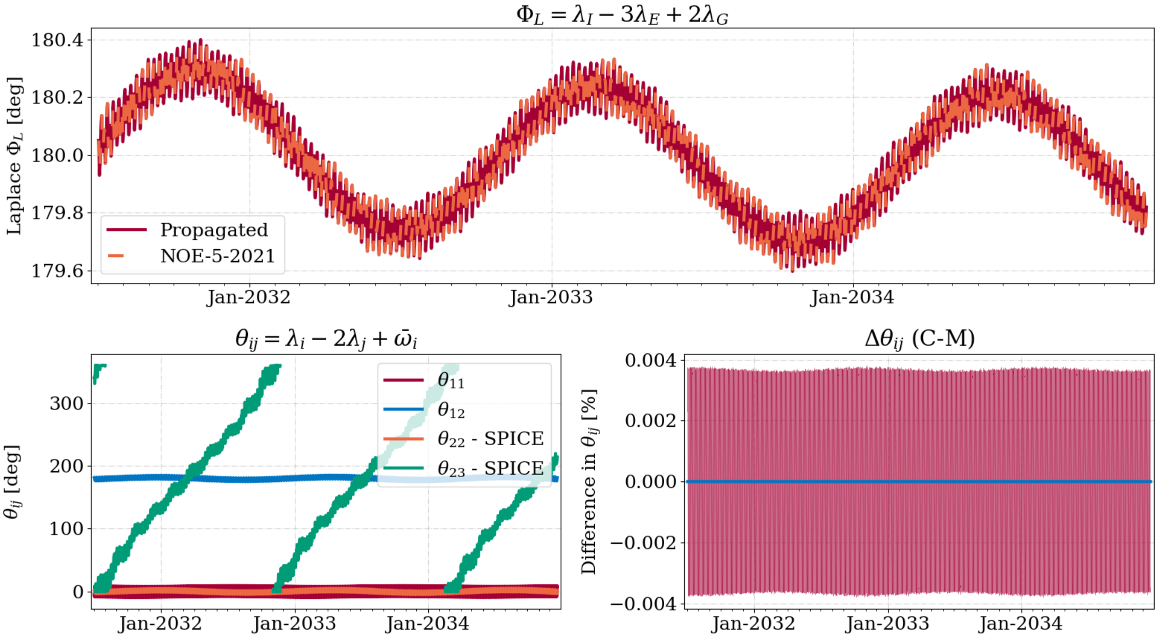

Figure B.2: Validation of the presence of the Laplace resonance in the computed model (C). The states of Io have been propagated using a fitted initial state and the delineated dynamical model. The overall Laplace angle and the two longitudes of conjunction of the inner resonance pair (Io and Europa) are compared with their reference values (M) taken from the NOE-5-2021 ephemerides. Complementary, the behaviour of the two longitudes of conjunction of the outer resonance pair (Europa and Ganymede) as obtained from the respective ephemerides states (SPICE) is shown.

To validate the presence of the Laplace resonance between the propagated state of Io and the states of Europa and Ganymede (as taken from their respective SPICE kernels) in our dynamical model, we compare the propagated stability of the Laplace angle over the period of the orbital phase of JUICE around Jupiter with the one exhibited by the NOE ephemerides in Figure B.2. Besides, we furthermore illustrate the behaviour and relative deviations of the two inner longitudes of conjunction between Io and Europa. Relative differences have been calculated with respect to the NOE-5-2021 ephemerides. Realise that in order to illustrate the distinct demeanour of the two outer longitudes of conjunction between Europa and Ganymede, we have opted to visualise their reference values (obtained using the respective NOE-5-2021 ephemerides) alongside their propagated, inner counterparts.

Overall, the presence of the Laplace resonance in our model is confirmed by the almost perfect congruence between the propagated and reference resonant argument. Yet, at first glance, while the Laplace angle indeed librates around a mean value of 180°, both our dynamical representation, as well as the one of the reference system, exhibit a period of about 16 months ($\approx$ 487 days), distinctively different from the outlined 2059.622 days. However, careful analysis leads to the conclusion that this long-term libration is indeed present - though only poorly visible given the limited time-scale of Figure B.2 - and superpositioned by a second, prominent oscillation with a period of the above-stated 16 months. Realise the agreement with the period with which θ_{23} is circulating through 360° - thus, presumably, the driving dynamical effect behind the librations in the Laplace angle. Furthermore, this short-term libration perfectly agrees with the one exhibited by the NOE reference ephemerides. The demeanour of the two propagated, inner longitudes of conjunction over time is as expected based on the above-provided explanations - Figure B.2 clearly illustrates librations around 0° for θ_{11} and around 180° for θ_{12}. In relative terms, the difference between the propagated and reference longitudes of conjunction are perfectly periodic and (almost) negligible. Hence, we can conclude that Io, Europa, and Ganymede remain in stable resonance over the duration of the orbital phase of JUICE around Jupiter.

B.1.3. Agreement with the Trajectories of JUICE

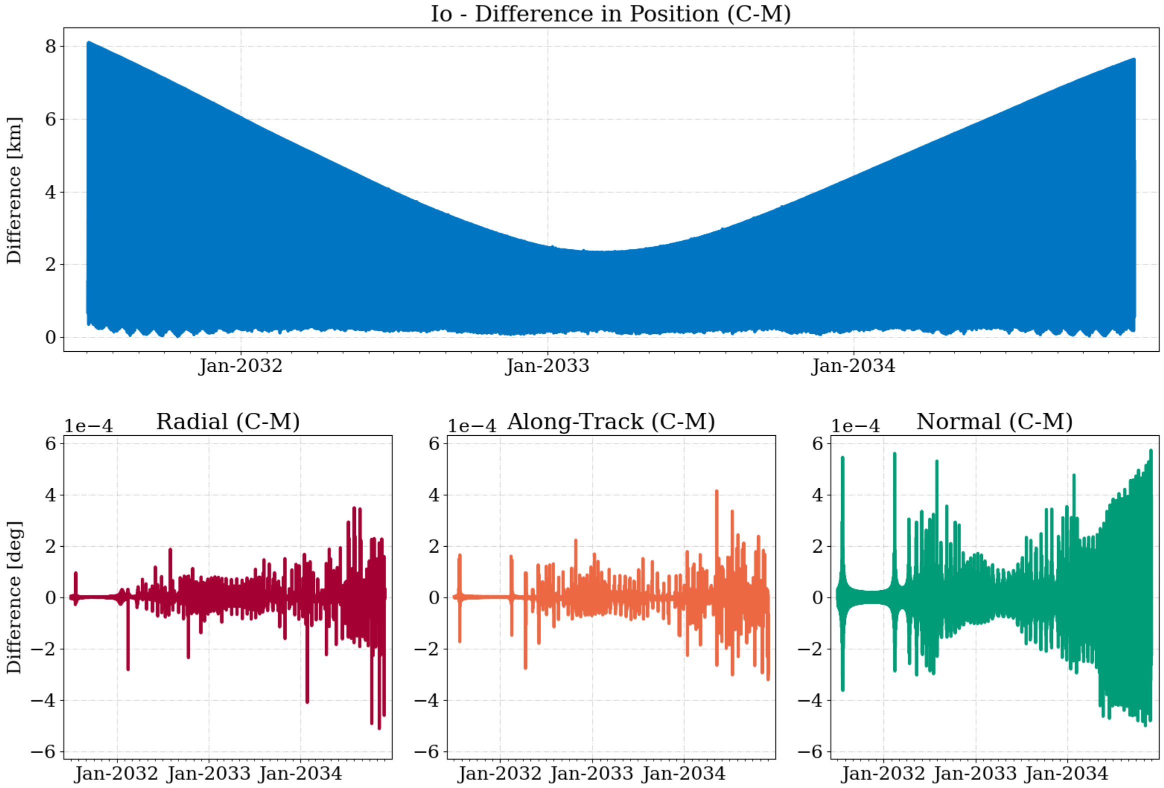

Figure B.3: Residuals in the distance between JUICE and both the propagated state of Io (C) and its NOE-5-2021 ephemeris (M) and the relative angles with the body-fixed axes of Io over the duration of the orbital phase around Jupiter.

Finally, for the simulation of optical space-based astrometry, we have to validate that the trajectory of JUICE taken from its respective SPICE kernels is in agreement with the propagated state of Io. Since the optical uncertainty, as well as the observation schedule and constraints, are a function of the momentaneous observation geometry, a good agreement between the trajectory of JUICE and the propagated orbit of Io is crucial. To this end, we evaluate and visualise the differences in the distance between JUICE and both Io's propagated and reference trajectories, as well as the relative angles with the body-fixed axes of Io over the duration of the orbital phase around Jupiter in Figure B.3.

First, as expected, the absolute difference between the trajectory of JUICE and the propagated state of Io (C) and its NOE-5-2021 ephemeris (M) are perfectly identical to the previously delineated behaviour for the state of Io in Figure B.1. Even though this is trivial from a purely mathematical point-of-view since we have taken the state of JUICE from the same reference trajectory, for the sake of completeness, we nevertheless want to stress that - given a minimum distance between JUICE and Io of approximately 381,492 kilometres - the highlighted difference is reasonably negligible. Second, the differences in the relative angles between the JUICE-Io observation vector and Io's three body-fixed axes - radial, along-track, and normal - exhibit a common trend, with slightly more pronounced offsets towards the end of the propagation. Yet, entirely independent of the overall trend, the maximum difference never exceeds 0.0006 degrees and can thus be reasonably neglected. Hence, the above-outlined findings validate the almost perfect agreement of the trajectory of JUICE with the propagated state of Io.

B.2. Validation of Optical Observation Constraints

Given the intricate reduction process of space-based astrometric images, several constraints have to be met to ensure unbiased observations with low associated uncertainties. The implemented restrictions for optical observations using the NavCam of JUICE have been outlined in Section 4.3 of the journal paper. For the sake of completeness, we have re-stated the entire set of general parameters in Table B.1. Note that parameters have been chosen such that the images' number of visible background stars does not get corrupted by any external influences (e.g. the minimum Sun-Spacecraft-Moon angle) or to reduce any sources of error within the limb-fitting process (e.g. maximum Sun-Moon-Spacecraft (phase-)angle). Similarly to any picture taken on Earth, imaging against direct sunlight will cause the contrast to drop and contours to blur - thus, a too high Sun-Moon-Spacecraft angle would result in erroneous fits of the moon's limb (*e.g.* Cooper et al., 2014).

Table B.1: Assumptions of general parameters for the NavCam, according to Boutonnet et al. (2018).

Parameter	Value
Minimum number of pixels to be filled by the moon	5
Maximum fraction of the FOV allowed to be filled by the moon	$1/\sqrt{5}$
Minimum Sun-Spacecraft-Moon angle	30°
Minimum Jupiter-Limb-Spacecraft-Moon angle	5° for apparent size of Jupiter > 4°
Maximum Sun-Moon-Spacecraft angle	130°
Time around closest approach without NavCam	±12 hrs

In addition to the value for the minimum Jupiter-Limb-Spacecraft-Moon angle stated in Table B.1, we have implemented a secondary constraint stipulating that for an apparent size of Jupiter smaller than four degrees, a minimum angle of ten degrees has to be met. On a final note, we want to underline that neither the constraint for the minimum number of pixels to be filled by the moon nor for the maximum fraction of the FOV allowed to be filled by the moon will never be met for Io - with at least 5.73 and no more than 15,397 pixels (of the total 1,048,576 - corresponding to a fraction of 1.4 per cent) ever being filled by the moon - justifying the omission of any further validation of the implementation hereof.

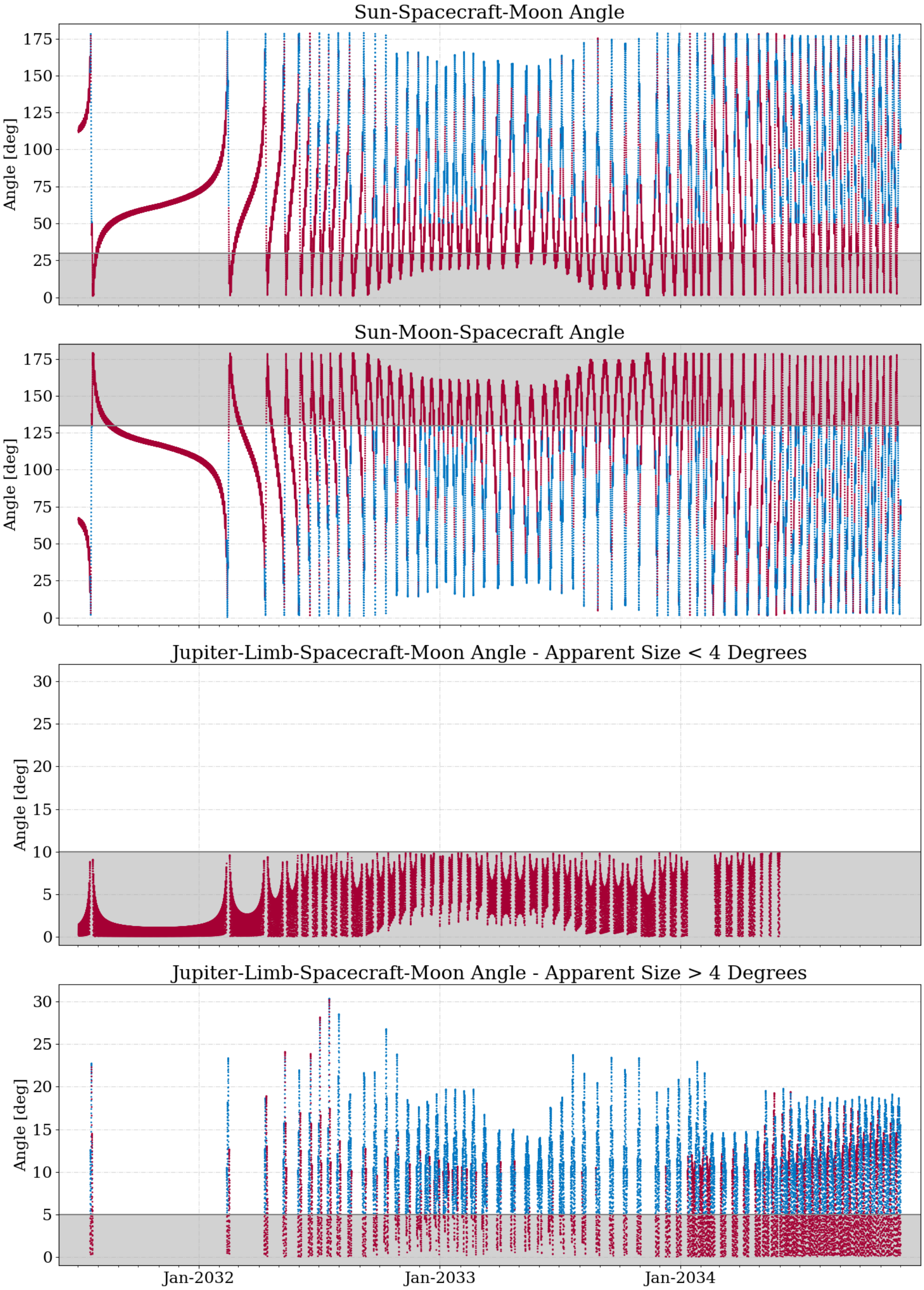

Figure B.4: Relative observation geometries of Io with respect to JUICE. Overall variations in the Sun-Spacecraft-Moon angle, the Jupiter-Limb-Spacecraft-Moon angle, and the Sun-Moon-Spacecraft angle are given over time. While shaded regions indicate the constraints for the individual angles, (in-)feasible epochs are depicted in red or blue, respectively.

Having first verified the implementation of the three overall orbital angles - the Sun-Spacecraft-Moon angle, the Jupiter-Limb-Spacecraft-Moon angle, and the Sun-Moon-Spacecraft angle - using a set of unit tests, we can subsequently validate the computation of their respective constraints. To this end, Figure B.4 visualises the behaviour of the three angles with respect to Io over time. The angle between Jupiter's limb, JUICE, and Io has been split in two distinct cases, depending on the apparent size of Jupiter in or outside of the FOV. Shaded parts indicate the overall regions for which individual constraints are met. Hence, trivially, every epoch's angular geometry herein must be deemed unfeasible - which has both visually (see Figure B.4) and analytically been reviewed using a second set of unit tests, validating the correct implementation of the optical observation constraints.

B.3. Deterministic Verification of the Covariance Analysis

So far, the formal uncertainties arising from covariance analysis have been interpreted as error-free. Yet, we have to verify whether the formal covariance errors estimated and discussed in Sections 5 and 6 of the journal paper are consistent with the values that would be estimated from real observations (i.e. including noise) using iterative least-squares orbit determination. While the conceptual study performed in the journal paper has been restricted to a pure covariance analysis, for the purpose of verification we have also performed a 'full' least-squares estimation (see Section 3.1 of the journal paper) referred to as deterministic simulation in the following. Note that Fayolle et al. (2022) have outlined an identical deterministic simulation as verification of a covariance analysis, which is where the structure and methodology of this section have greatly drawn inspiration from. To verify our implemented estimation framework, the outlined deterministic approach has to obey the same assumption as the covariance analysis - the perfect agreement between the observational and dynamical models. Hence, we have to stress that while a deterministic simulation, in essence, allows an assessment of the consistency between the estimated formal and true errors, this analysis must not be seen as validation of how representative the formal errors are of the true errors (i.e. the determination of a true-to-formal-error ratio) obtained from real data. Nonetheless, the proposed deterministic verification ensures the correct implementation of the estimation framework and underlines the robustness of the obtained formal errors in the context of covariance analysis.

B.3.1. Methodology and Settings

In general, as stated by Fayolle et al. (2022), variations within the values of a set of parameters using an iterative weighted least-squares estimation routine are given by (*e.g.* Montenbruck and Gill, 2000)

$$\Delta\vec{q}_i = \left(\boldsymbol{P}_0^{-1} + \boldsymbol{H}_i^T \boldsymbol{W}_i \boldsymbol{H}_i\right)^{-1} \left(\boldsymbol{H}_i^T \boldsymbol{W}_i \Delta\vec{z}_i + \boldsymbol{P}_0^{-1} \Delta\vec{q}_{0,i}\right), \tag{B.4}$$

where $\Delta\vec{q}_i$ and $\Delta\vec{z}_i$ denote the variation in parameters values and the vector containing the observations residuals at each iteration i, respectively, and $\Delta\vec{q}_{0,i}$ is the difference between the current parameters estimates and their a priori values. While $\boldsymbol{H}_i$ and $\boldsymbol{W}_i$ denote the current design and weight matrix, the overall *a priori* matrix is given by $\boldsymbol{P}_0$.

As outlined by Fayolle et al. (2022), true errors are directly computed from the difference between their estimated values and their true parameters' values assumed in our dynamical model. Optical space-based observations are modelled with the noise level computed using the derived analytical expression for space-based astrometric uncertainties (see Section 4.1 of the journal paper). A total of 1280 epochs at which observations have been simulated have been chosen randomly using the delineated hybrid algorithm (see Section 4.4 of the journal paper). Furthermore, random three-dimensional offsets between the centre-of-figure and centre-of-mass (randomly selected from a Gaussian distribution with a standard deviation of one kilometre in all three directions) have been taken into account. Estimations have been performed for a total of 100 different COF-COM-offset combinations. To mimic imperfect knowledge of the true ephemeris of Io, we have artificially perturbed the initial state using a randomly selected state inside its multivariate probability distribution multiplied by a scaling factor of five.

B.3.2. Results

No more than ten iterations have been required for the least-squares estimator to reach convergence. While, at first glance, this seems slightly extensive, note that we have altered the initial state of Io by five times a randomly selected perturbation within its multivariate probability distribution. With $\sigma_{i,0}$ being the formal uncertainty given by the constraining radio science solution, we have *de facto* perturbed the state of Io with a new standard deviation of $5\sigma_{i,0}$. Since we have not altered the radio science constraint, this artificially introduced mismatch between the implemented *a priori* information and the perturbed state of Io underlines the need for higher numbers of iterations to reach convergence.

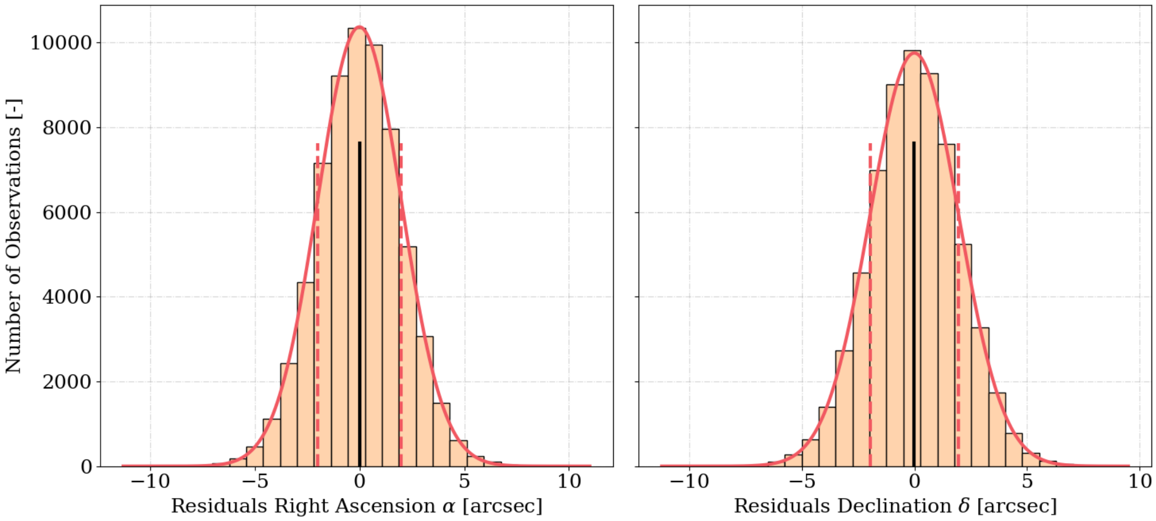

Figure B.5: Final observation residuals residuals in right ascension and declination after the weighted least-squares estimation reached convergence. Black lines indicate the mean of the residuals for each observable, while dashed red lines represent the standard deviation. The initial state of Io has been constrained by a radio science *a priori* covariance matrix with a true-to-formal-error ratio of unity. A total number of 1280 astrometric observations have been simulated.

For a radio science true-to-formal-error ratio of unity, the final observations residuals in right ascension and declination are provided in Figure B.5. Unsurprisingly, both residuals follow an approximated Gaussian distribution with almost zero mean. Furthermore, their respective standard deviations lie in the close vicinity of the averaged noise level of the selected observation epochs (see Section 5.1 of the journal paper). Increasing the radio science true-to-formal-error ratio to eight (see Figure B.6) does not notably influence the final observations residuals. We can still observe two approximated Gaussian distributions centred around a mean value of nought while the associated standard deviations remain equal to the average noise level of the simulated astrometric observations.

For a radio science *a priori* true-to-formal-error ratio of unity, Figure B.7 provides the histograms of the estimated true-to-formal-error ratio in the position, velocity, and COF-COM-offset of Io. It has to be stressed that we need to distinguish between two distinct true-to-formal-error ratios - the one used to scale the *a priori* constraint and the one arising from our parameter estimation. For the latter, all values lie between zero and eight, with significant differences between the estimated state variables

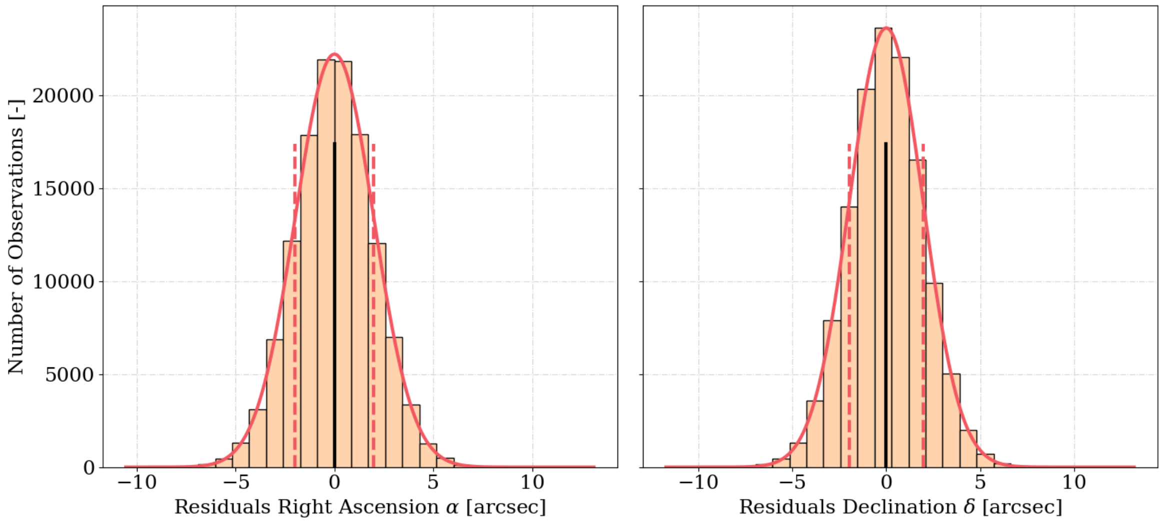

Figure B.6: Final observation residuals residuals in right ascension and declination after the weighted least-squares estimation reached convergence. Black lines indicate the mean of the residuals for each observable, while dashed red lines represent the standard deviation. The initial state of Io has been constrained by a radio science *a priori* covariance matrix with a true-to-formal-error ratio of eight. A total number of 1280 astrometric observations have been simulated.

(zero to eight) and the offset between the COF and COM (zero to four). As highlighted by Fayolle et al. (2022), the underlying estimation models are nonetheless deemed faultless, with converged true errors theoretically being representative of the estimated formal uncertainties (i.e. the true error is an individual of the entire population described by a Gaussian distribution with a standard deviation equal to the estimated formal error). Furthermore, the deterministic simulation highlights two distinct trends - one within the true-to-formal-error ratio of the state of Io and one for the COF-COM-offset. While the obtainable standard deviation for the former is skewed towards two (instead of the ideal value of one), the standard deviation of the latter lies slightly below unity.

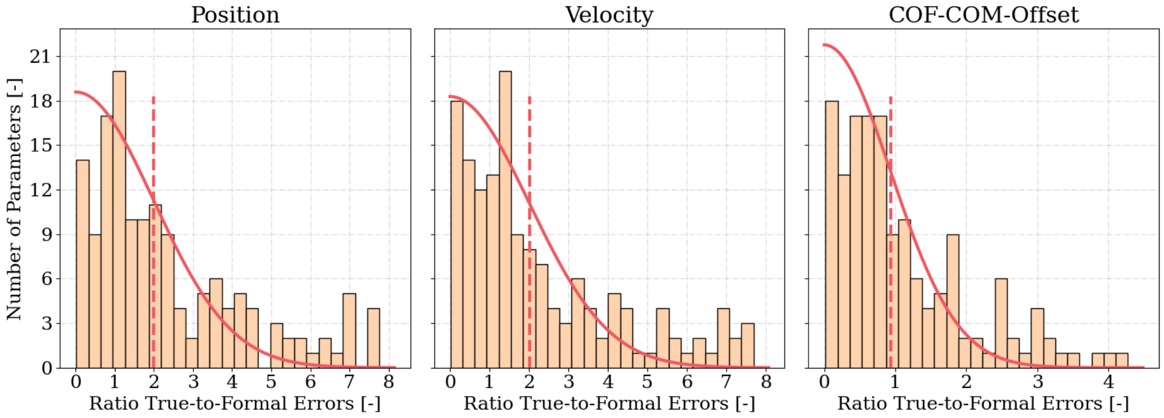

Figure B.7: Distribution of the true-to-formal-error ratio for all estimated parameters. Nine parameters - initial state (3D position, 3D velocity) of Io alongside the COF-COM-offset (constant 3D vector) - were estimated. The initial state of Io has been constrained by a radio science *a priori* covariance matrix with a true-to-formal-error ratio of unity. A total number of 1280 astrometric observations have been simulated.

We have shown that for low radio science true-to-formal-error ratios - in particular for ratios of unity - optical space-based observations will only negligibly contribute to the orbital solution of Io (see Section 5.3.2 of the journal paper). Perturbing the initial state, however, requires the improvement of the initial state solely by the simulated astrometry, and thus only two distinct, relative observables - right ascension and declination. The formal error - by design unaware of the perturbation - is still dominated by the tight *a priori* constraint. Yet, with the formal errors being wronged by the perturbed initial state, space-based astrometry has to fully constrain the orbital solution. Given the much coarser associated uncertainties as well as the theoretical negligible contribution to the estimation of the initial state, the obtained true-to-formal-error ratios in position and velocity (see Figure B.7) are still laudable. Nonetheless, we have to note that for low radio science true-to-formal-error ratios, the *a priori* constraint might be too tight when dealing with perturbed states and formal errors have to be treated with caution. On the other hand, as expected, the discrepancy between the centre-of-figure and centre-of-mass has been estimated to a high level of accuracy, with true-to-formal-error ratios no higher than three. This is entirely in line with our conclusions on the observations' ability to constrain the COF-COM-offset (see Section 5.3.1 of the journal paper) and verifies the robustness of the offset's estimation.

To confirm these preliminary conclusions and limitations of our estimation framework, we have increased the radio science *a priori* true-to-formal-error ratio from unity to eight, with Figure B.8 providing the associated histograms of the estimated true-to-formal-error ratio in the position, velocity, and COF-COM-offset of Io. As expected - based on the above-outlined explanation - the estimated true-to-formal-error ratios in the initial state have been reduced by about 30 per cent (from 2.0 to 1.4), with maximum ratios never exceeding a value of seven. However, this comes at the expense of an increase in the true-to-formal-error ratio of the estimated COF-COM-offset. While a significant amount of ratios still lies between zero and one (with total numbers roughly equal to those earlier provided in Figure B.7), the values located in the tail of the distribution are skewed to notably higher ratios, with the limit value increased by about a factor two. Yet, this behaviour is perfectly in line with the conclusion delineated in Section 5.3.2 as well as the above-presented explanations.

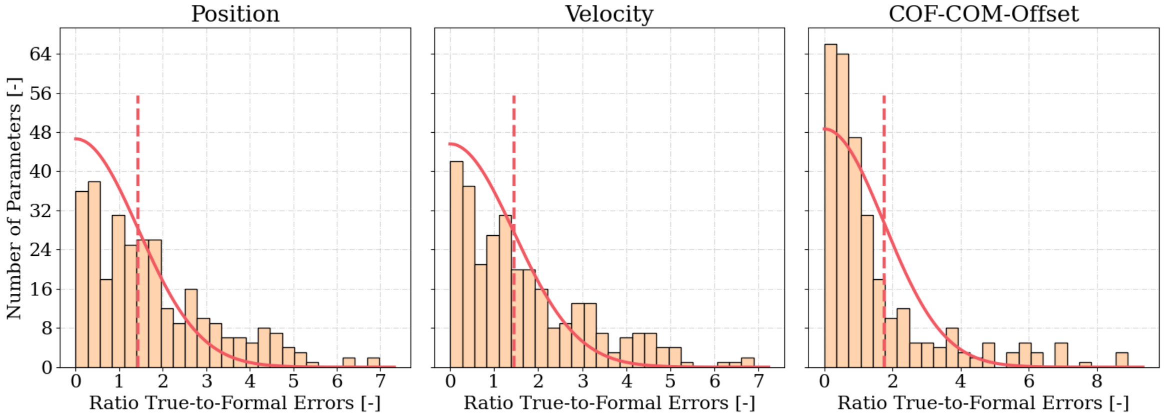

Figure B.8: Distribution of the true-to-formal-error ratio for all estimated parameters. Nine parameters - initial state (3D position, 3D velocity) of Io alongside the COF-COM-offset (constant 3D vector) - were estimated. The initial state of Io has been constrained by a radio science *a priori* covariance matrix with a true-to-formal-error ratio of eight. A total number of 1280 astrometric observations have been simulated.

Using a deterministic approach, we have successfully verified that the formal uncertainties provided by our covariance analysis are a good representation of the achievable true errors, underlining the robustness of our analysis. Nonetheless, we have to slightly differentiate this statement - with decreasing quality of the radio science solution, the slight underestimation of the formal errors is shifted from the two state-parameter sub-sets (position and velocity) to the estimation of the offset between the centre-of-figure and centre-of-mass skewing the overall distribution towards higher values. Yet, we have found that this hints at minor issues arising from the tight *a priori* constraints of our estimation framework.

C

Additional Material

To give the reader an impression of the trajectory JUICE is going to follow whilst orbiting Jupiter, as well as highlight the distance maintained with Io - with no orbit closer than the semi-major axis of Europa - Figure C.1 visualises this particular trajectory, covering a total time span of 1,270 days.

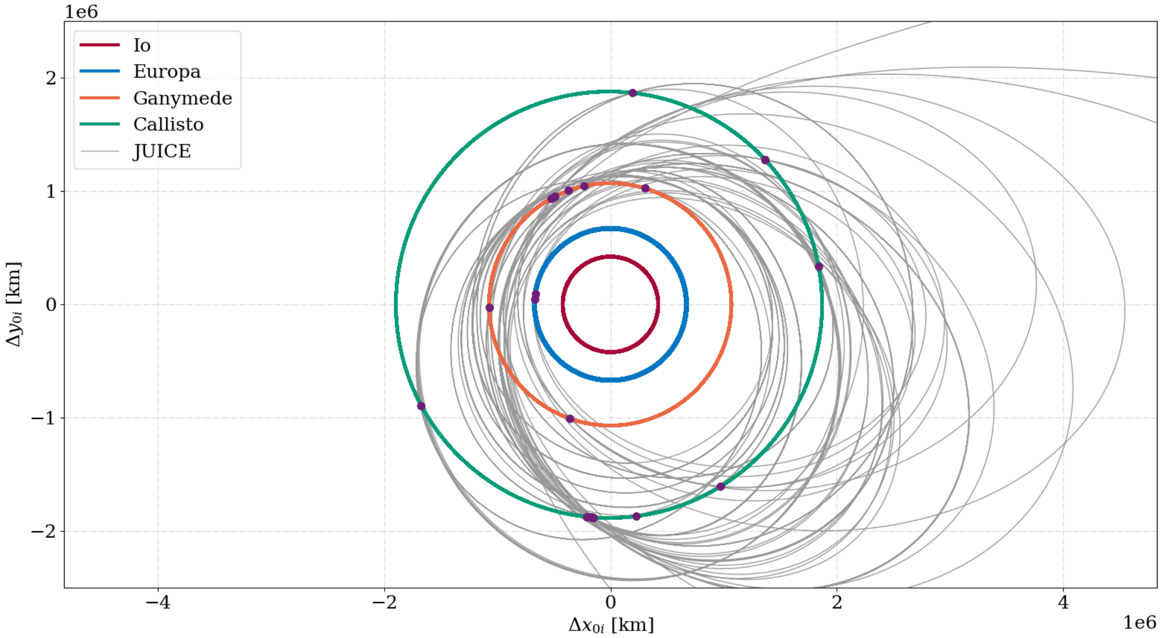

Figure C.1: Trajectory of JUICE taken from SPICE. A total time span of 1,270 days from July 1st 2031 onward is shown. Moments of closest approach during the flybys of JUICE have been highlighted in purple.

References

Boutonnet, A., Varga, G., Rocchi, A., Martens, W., and Mackenzie, R. (2018). *JUICE - Jupiter Icy moons Explorer Consolidated Report on Mission Analysis (CReMA)* (Report). ESA-ESOC (European Space Operations Centre).

Cooper, N. J., Murray, C. D., Lainey, V., Tajeddine, R., Evans, M. W., and Williams, G. A. (2014). Cassini ISS mutual event astrometry of the mid-sized Saturnian satellites 2005–2012. *Astronomy & Astrophysics*, *572*.

Davies, A. G. (2007, August). *Volcanism on io: A comparison with earth*. Cambridge University Press.

Dias-Oliveira, A., Vieira-Martins, R., Assafin, M., Camargo, J. I. B., Braga-Ribas, F., da Silva Neto, D. N., Gaspar, H. S., Pires dos Santos, P. M., Domingos, R. C., Boldrin, L. A. G., Izidoro, A., Carvalho, J. P. S., Sfair, R., Sampaio, J. C., and Winter, O. C. (2013). Analysis of 25 mutual eclipses and occultations between the Galilean satellites observed from Brazil in 2009. *Monthly Notices of the Royal Astronomical Society*, *432*(1), 225–242.

Dirkx, D., Gurvits, L. I., Lainey, V., Lari, G., Milani, A., Cimò, G., Bocanegra-Bahamon, T. M., and Visser, P. N. A. M. (2017). On the contribution of PRIDE-JUICE to Jovian system ephemerides. *Planetary and Space Science*, *147*, 14–27.

Fayolle, M., Dirkx, D., Lainey, V., Gurvits, L. I., and Visser, P. N. A. M. (2022). Decoupled and coupled moons' ephemerides estimation strategies application to the JUICE mission. *Planetary and Space Science*, *219*.

Fayolle, M., Dirkx, D., Visser, P. N. A. M., and Lainey, V. (2021). Analytical framework for mutual approximations. *Astronomy & Astrophysics*, *652*.

Fayolle, M., Magnanini, A., Lainey, V., Dirkx, D., Zannoni, M., and Tortora, P. (2023). Combining astrometry and JUICE – Europa Clipper radio science to improve the ephemerides of the Galilean moons. *Astronomy and Astrophysics*, *677*, A42.

Fuller, J., Luan, J., and Quataert, E. (2016). Resonance locking as the source of rapid tidal migration in the jupiter and saturn moon systems. *Monthly Notices of the Royal Astronomical Society*, *458*(4), 3867–3879.

Greenberg, R. (2010). The icy Jovian satellites after the Galileo mission. *Reports on Progress in Physics*, *73*(3).

Heller, R., Marleau, G. D., and Pudritz, R. E. (2015). The formation of the Galilean moons and Titan in the Grand Tack scenario. *Astronomy & Astrophysics*, *579*.

Hussmann, H., Choblet, G., Lainey, V., Matson, D. L., Sotin, C., Tobie, G., and Van Hoolst, T. (2010). Implications of rotation, orbital states, energy sources, and heat transport for internal processes in icy satellites. *Space Science Reviews*, *153*(1-4), 317–348.

Jacobson, R. A., Haw, R. J., McElrath, T. P., and Antreasian, P. G. (2000). A comprehensive orbit reconstruction for the galileo prime mission in the j2000 system. *The Journal of the Astronautical Sciences*, *48*(4), 495–516.

Kaula, W. M. (1964). Tidal dissipation by solid friction and the resulting orbital evolution. *Reviews of Geophysics*, *2*(4).

Lainey, V., Arlot, J.-E., Karatekin, Ö., and Van Hoolst, T. (2009). Strong tidal dissipation in Io and Jupiter from astrometric observations. *Nature*, *459*(7249), 957–959.

Lainey, V., Casajus, L. G., Fuller, J., Zannoni, M., Tortora, P., Cooper, N., Murray, C., Modenini, D., Park, R. S., Robert, V., and Zhang, Q. (2020). Resonance locking in giant planets indicated by the rapid orbital expansion of titan. *Nature Astronomy*, *4*(11), 1053–1058.

Lainey, V., Dehant, V., and Pätzold, M. (2007). First numerical ephemerides of the Martian moons. *Astronomy & Astrophysics*, *465*(3), 1075–1084.

Lainey, V., Duriez, L., and Vienne, A. (2004). New accurate ephemerides for the Galilean satellites of jupiter. *Astronomy and Astrophysics*, *420*(3), 1171–1183.

Lainey, V., Duriez, L., and Vienne, A. (2006). Synthetic representation of the galilean satellites' orbital motions from l1 ephemerides. *Astronomy & Astrophysics*, *456*(2), 783–788.

Lainey, V., Jacobson, R. A., Tajeddine, R., Cooper, N. J., Murray, C., Robert, V., Tobie, G., Guillot, T., Mathis, S., Remus, F., Desmars, J., Arlot, J.-E., De Cuyper, J.-P., Dehant, V., Pascu, D., Thuillot, W., Poncin-Lafitte, C. L., and Zahn, J.-P. (2017). New constraints on Saturn's interior from Cassini astrometric data. *Icarus*, *281*, 286–296.

Lainey, V., Karatekin, Ö., Desmars, J., Charnoz, S., Arlot, J.-E., Emelyanov, N., Poncin-Lafitte, C. L., Mathis, S., Remus, F., Tobie, G., and Zahn, J.-P. (2012). Strong tidal dissipation in Saturn and constraints on Enceladus' thermal state from astrometry. *The Astrophysical Journal*, *752*(1), 14.

Lari, G. (2018). A semi-analytical model of the Galilean satellites' dynamics. *Celestial Mechanics and Dynamical Astronomy*, *130*(8).

Magnanini, A., Zannoni, M., Gomez Casajus, L., Tortora, P., Lainey, V., Mazarico, E., and Park, R. S. (2023). Joint analysis of JUICE and Europa Clipper tracking data to study the Jovian system ephemerides and dissipative parameters. *A&A - Under Review*.

Montenbruck, O., and Gill, E. (2000). *Satellite orbits: Models, methods, and applications*. Springer Berlin Heidelberg.

Murray, C. D., and Dermott, S. F. (1999). *Solar System dynamics*. Cambridge University Press.

Pasewaldt, A., Oberst, J., Willner, K., Wählisch, M., Hoffmann, H., Matz, K. D., Roatsch, T., Hussmann, H., and Lupovka, V. (2012). New astrometric observations of Deimos with the SRC on Mars Express. *Astronomy & Astrophysics*, *545*.

Peale, S. J., Cassen, P., and Reynolds, R. T. (1979). Melting of io by tidal dissipation. *Science*, *203*(4383), 892–894.

Samuel, H., Lognonné, P., Panning, M., and Lainey, V. (2019). The rheology and thermal history of Mars revealed by the orbital evolution of Phobos. *Nature*, *569*(7757), 523–527.

Smith, D. E., Zuber, M. T., Neumann, G. A., and Lemoine, F. G. (1997). Topography of the Moon from the Clementine lidar. *Journal of Geophysical Research: Planets*, *102*(E1), 1591–1611.

Steinke, T. (2021). *The curious case of Io - connections between interior structure, tidal heating and volcanism* [Thesis]. Technische Universiteit Delft.

Vienne, A. (2008). Dynamical objectives of observation of mutual events. *Planetary and Space Science*, *56*(14), 1797–1803.

Yoder, C. F. (1979). How tidal heating in Io drives the Galilean orbital resonance locks. *Nature*, *279*(5716), 767–770.

Yoder, C. F., and Peale, S. J. (1981). The tides of Io. *Icarus*, *47*(1), 1–35.

Zuber, M. T., Smith, D. E., Lemoine, F. G., and Neumann, G. A. (1994). The shape and internal structure of the Moon from the Clementine mission. *Science*, *266*(5192), 1839–1843.